3-21-2013

Biaxial (Tension-Torsion) Testing of an Oxide/Oxide Ceramic Matrix Composite

Joseph M. DeRienzo

Follow this and additional works at: https://scholar.afit.edu/etd

Part of the Aerospace Engineering Commons

BIAXIAL (TENSION-TORSION) TESTING OF AN OXIDE/OXIDE CERAMIC
MATRIX COMPOSITE

THESIS

Joseph M. DeRienzo, Captain, USAF

AFIT-ENY-13-M-10

DEPARTMENT OF THE AIR FORCE
AIR UNIVERSITY

AIR FORCE INSTITUTE OF TECHNOLOGY

Wright-Patterson Air Force Base, Ohio

AFIT-ENY-13-M-10

BIAXIAL (TENSION-TORSION) TESTING OF AN OXIDE/OXIDE CERAMIC

MATRIX COMPOSITE

THESIS

Presented to the Faculty

Department of Aeronautics and Astronautics

Graduate School of Engineering and Management

Air Force Institute of Technology

Air University

Air Education and Training Command

in Partial Fulfillment of the Requirements for the

Degree of Master of Science in Materials Science

Joseph M. DeRienzo, B.S.

Captain, USAF

March 2013

AFIT-ENY-13-M-10

BIAXIAL (TENSION-TORSION) TESTING OF AN OXIDE/OXIDE CERAMIC

MATRIX COMPOSITE

Joseph M. DeRienzo, B.S.
Captain, USAF

Approved:

_____   _____
Marina B. Ruggles-Wrenn, PhD (Chairman)   Date

_____   _____
Thomas G. Eason, PhD (Member)   Date

_____   _____
Gregory A. Schoeppner, PhD (Member)   Date

Abstract

High temperatures and structural loads in advanced aerospace structures often result in complex loading conditions. This study is focused on biaxial (tension-torsion) testing of an oxide-oxide porous matrix ceramic matrix composite (CMC) (Nextel^{TM} 720/AS) thin wall tube with a novel involute layup. Tests included pure torsion and biaxial (tension-torsion) loading. Strain gages were used in addition to digital image correlation (DIC) to measure strains and to detect crack initiation and propagation. Room temperature and 1100°C uniaxial tests were performed in a build up approach prior to biaxial (tension-torsion) testing. Double-notch shear (DNS) specimens were tested at 1100°C in air to obtain interlaminar shear strength (ILSS).

Acknowledgments

This project would not have been possible without the opportunity from my advisor, Dr. Marina Ruggles-Wrenn, and my sponsors at AFRL in Mr. Larry Zawada, Dr. Eric Jones, and Dr. Craig Przybyla. My advisor and sponsors' time in their own educational opportunities and the work they have done in their post-educational endeavors is remarkable and personally admirable. I sincerely appreciate them giving me an opportunity to learn under their guidance.

I'd also like to publicly acknowledge the men of the AFIT Model Shop who dedicated themselves to accomplishing non-standard, unusual, and oftentimes very difficult, risky, and extremely time-intensive work required for test article machining, preparation, and setup. Mr. Dan Ryan, Mr. Brian Crabtree, and Mr. Chris Hawkless all spent more time than I ever could have asked them to have ever spent on my test articles. They are absolute professionals and I regard their work, work ethic, and enthusiasm in very high regard. I simply would not have taken off, let alone landed, without their power. I appreciate their supervisor Jan LeValley for enabling Dan, Brian, and Chris to use their talents appropriately on my project.

Additional thanks goes to Mr. Jay Anderson and Mr. Barry Page of AFIT and Mr. Greg Walsh of MTS. Jay and Barry were instrumental in teaching me the use of the test equipment, testing within the AFIT lab, and having a lab with functional test platforms and test instrumentation. The true measure of their help is in getting my test equipment back in order after malfunctions and test setup setbacks. Jay and Barry never took these lightly and were always instrumental in making sure my test equipment was never the limiting factor in my testing. I am grateful for Jay and Barry's work in having and maintaining such top notch facilities for these endeavors. Greg was a miracle worker getting the biaxial

Table of Contents

List of Figures

xiii

List of Tables

List of Symbols

Symbol	Definition
$\mu\epsilon$	$\frac{\Delta L}{L_0} x 10^{-6}$ (microstrain)
Ω	resistance (Ohms)
kip	1,000 pounds-force

List of Acronyms

Acronym	Definition
ABS	absolute value
AFIT	Air Force Institute of Technology
AFRL	Air Force Research Laboratory
alumina	Al_2O_3
aluminosilicate	Al_2SiO_5
ASTM	American Society for Testing and Materials
CMC	ceramic matrix composite
CNC	Computer Numerically Controlled
COI	Composite Optics, Inc.
DIC	Digital Image Correlation
DNS	double-notch shear
EBC	environmental barrier coatings
FEA	finite element analysis
FOV	field of view
GOM	Gesellschaft für Optische Messtechnik
ILSS	interlaminar shear strength
PMC	polymer matrix composite
SCA	Signal Conditioning Amplifier
SiC	silicon carbide
SiC-SiC	Silicon Carbide-Silicon Carbide
UDRI	University of Dayton Research Institute
USS	ultimate shear strength
UTS	ultimate tensile strength

BIAXIAL (TENSION-TORSION) TESTING OF AN OXIDE/OXIDE CERAMIC

MATRIX COMPOSITE

I. Introduction

C omposite materials combine multiple material phases into a material system designed to execute a desirable performance characteristic or set of characteristics. If designed properly, the sum properties of the phases exceed those of the constitutive parts[8]. The phase of material that is continuous throughout the material is referred to as the matrix. The matrix serves as a binder to hold the composite together in addition to providing a mechanism for load transfer to the reinforcement. The reinforcement is discontinuous through the composite and provides the main load-bearing capability. The interaction of the two (or more) phases takes place in the interface. The interface can be controlled through an interphase, often applied to the reinforcement, to achieve a desired interface between the matrix and reinforcement. An interphase, however, is not required present in a composite. The reinforcement and matrix and the interface can be engineered to achieve different macroscopic material properties. Processing, layup, and construction of phases into a composite often have more influence on macroscopic system material properties than the constitutive materials themselves[15].

Many modern aerospace, energy, automotive and biomedical engineering systems require components capable of withstanding harsh environments like those found in parts of gas turbine engines, nuclear power plants, the human body, and internal combustion engines[44][47][18]. Advanced gas turbine engines have already attained steady-state combustor temperatures of 1316°C. Under these conditions, one or more advanced cooling techniques such as louver, convection/film, film, impingement/film cooling, and thermal

1

barrier coatings are required to protect individual components currently made out of metal superalloys. Cooling effectiveness, ϕ, is defined in Equation (1.1) where T_g, T_m, and T_c are defined as mainstream gas, average metal, and cooling air temperatures. One superalloy found in combustor liners is Hastelloy X whose solid-phase upper limit is 982°C. If cooling air temperature is 649°C, per Equation (1.1), a combustor liner of Hastelloy X would have a cooling effectiveness of 0.5. Increasing mainstream gas temperature would increase overall turbine engine efficiency. To maintain the same cooling effectiveness with higher mainstream gas temperature, either average metal temperature must go up or cooling temperature must go down. Materials with higher upper temperature limits as well as abilities to withstand highly corrosive environments seen in turbine engines could increase operational temperatures of advanced turbine engines. Additionally, materials with higher upper temperature limits could reduce demands for turbine engine component cooling air[27]. Increasing overall turbine engine temperatures could increase overall engine efficiencies, thus, reducing fuel consumption and allow for greater design flexibility of engine airflow [13].

$$\phi = \frac{T_g - T_l}{T_g - T_c} \tag{1.1}$$

Ceramic materials offer higher temperatures and strength-to-weight ratios over metal super alloys while maintaining corrosive resistance. Disadvantages of ceramics, however, include brittleness and porosity including microscopic cracks inherent to monolithic ceramics. One promising candidate material class for use in high-temperature aerospace environments is CMCs. CMCs offer the advantages of high temperature ratings and high strength-to-weight ratio inherent to engineering ceramics with an increased fracture toughness reducing brittleness and unanticipated catastrophic failures[16].

Oxidating environments can present service limiting conditions for certain CMCs. Sources have observed performance degradations in certain CMCs like Silicon Carbide-

Silicon Carbide (SiC-SiC). To obtain extended service lifetimes with these oxidation-prone CMCs environmental barrier coatings (EBC) must be implemented[44]. The EBC prevents mechanical performance degradation due to oxidation[12]. Coatings increase the cost of CMC manufacture. All oxide materials provide high temperature, high strength-to-weight ratio, and oxidation resistant properties without the use of coatings [43].

One candidate oxide-oxide CMC commonly investigated for application in high temperature oxidizing aerospace applications is Nextel[TM] 720 fiber (3M, St. Paul MN) deposited in an oxide Al_2SiO_5 (aluminosilicate) matrix with no fiber-matrix interface coating. Nextel[TM] 720/AS is the focus of the present study. The oxide Nextel[TM] 720 reinforcement has a chemical composition of 85% Al_2O_3 and 15% SiO_2 (by weight) and is rated to 1200°C [30]. The Nextel[TM] 720/AS oxide-oxide CMC has an upper temperature limit of 1100°C limited by the aluminosilicate matrix [3]. The upper temperature limit of Nextel[TM] 720/AS is achieved with a density 2.60 g/cm^3 which is over three times less than the density of Hastelloy X at 8.22 g/cm^3.

A novel involute oxide-oxide CMC layup using fiber tapes has been developed by Composite Optics, Inc. (COI) Ceramics. According to COI Ceramics, this material layup exhibits efficiencies in processing resources, little to no ply wrinkling, a fine microstructure, and excellent machinability. This advancement in the processability of CMCs could enable more widespread use by reducing machining tolerances and manufacture of potential parts.

The goal of the present study is to investigate the porous matrix oxide-oxide CMC thin-wall involute tube under pure torsion and proportionally loaded tension-torsion. These studies will demonstrate procedures and produce preliminary results used for future testing and engineering component designs for advanced high-temperature aerospace structures. Procedures were developed through uniaxial tensile tests both in a 0° and 90° fiber-dominated orientation out of an involute panel in laboratory air at room and elevated temperatures (1100°C). Additional experimentation tested interlaminar shear properties of

a baseline balanced 0°/90° layup from an eight harness satin weave also in laboratory air and steam both at elevated temperatures (1100°C). Involute CMC layups were tested to further the understanding of a complex loading condition for future design considerations. Strain gages, in both linear and rectangular rosette gages, were used. GOM Aramis DIC software, a full-field displacement and strain measurement technique was also used to detect crack initiation and crack propagation. DIC utilizes a stochastic or random speckle pattern applied through various techniques such as commercially available spray paint, air brushing, or laser toner ink powder on the test article. DIC data can be used to verify and validate predictive computational models, such as finite element analysis (FEA), with its full field measurement capability.

II.   Background

2.1   Ceramic Matrix Composites

Monolithic ceramics often have strengths much greater than high-strength alloys, but their use in structural applications is limited by their brittle and damage intolerant nature. CMCs are tougher and more damage tolerant. A "nail test" illustrates the damage tolerant nature of CMCs. An attempt to drive a nail through a monolithic ceramic would result in catastrophic failure. The same nail driven through a CMC is more likely to be supported in a similar fashion to a nail driven through wood as seen in Figure 2.1. The fibers and matrix are able to keep damage localized near the nail penetration site similar to that of wood. Damage tolerant behaviors have led to the more widespread use of CMCs in advanced high-temperature engineering applications[43].
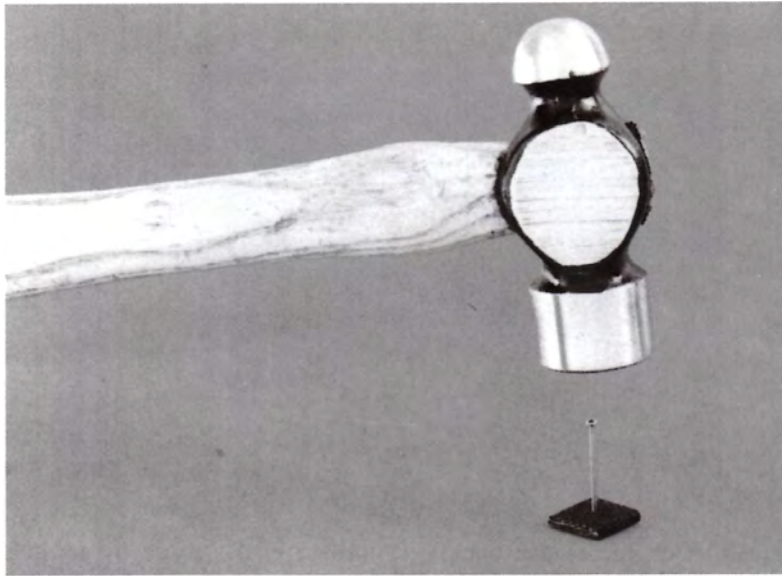
Figure 2.1: CMC nail test damage tolerance demonstration[13]

2.2   Fibers

Composite stiffness and strength is determined in large part by the configuration of the fiber reinforcement and fiber volume. Fiber reinforcement can be in the form of chopped fibers, whiskers, or continuous fibers either in unidirectional continuous, crossply or fabric, or multidirectional fiber composite [15]. Fibers possess higher flexibility and higher strength over the same bulk material phase in non-fiber form due to their small cross-section and high aspect ratio. Flaw size in fibers must inherently be smaller smaller than the fiber itself. The high aspect ratio allows for weaving fibers into fabric. Fabrics can be woven to obtain a desired flexibility which in turn affects the overall stiffness of the resultant fabric. Fabric weave influences composite matrix porosity. A plain or basket weave results in a stiffer fabric which usually increases matrix porosity within the composite while a satin weave in the common form of eight or five harness (8H or 5H) fabric is more flexible and usually reduces matrix porosity within the composite. The flexibility of the weave is influential in parts forming. Parts that require complex shapes can benefit from weaves that can be easily formed or draped into molds. Fibers can be made from polymers, metals or ceramics. Several ceramic fibers commercially available and used today include silicon carbide (SiC) and Al_2O_3 (alumina) available in under the Sylramic ^{TM}, Nicalon ^{TM}, and Nextel^{TM} brand names[13].

2.3   Matrix

Matrix serves to protect and support the fiber reinforcement as well as transfer loads between fibers[15]. The fiber-to-fiber load transfer mechanism provided by the matrix plays a major role in the load-bearing properties of the composite. A cross section of a composite is shown in Figure 2.2.

Many composites currently in use contain a polymer matrix such as polyethylene or epoxy with a carbon or glass reinforcement. polymer matrix composites (PMCs)
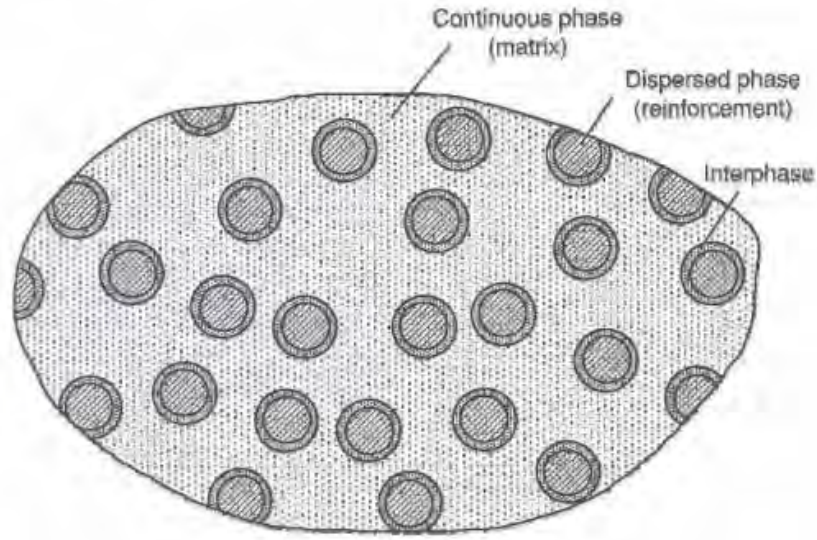
Figure 2.2: Typical composite cross section [15]

have gained wide acceptance across a wide range of uses such as aircraft wings and engines as well as civil structures[46][6][34]. Polymers have low density and fracture toughness similar to that of monolithic ceramics. Figure 2.3 illustrates the significantly lower operating temperature capability polymers have compared to ceramics. For CMCs to capitalize on their high temperature and low density properties and find a place in engineering designs and applications, an increase in damage tolerance must be made[13].
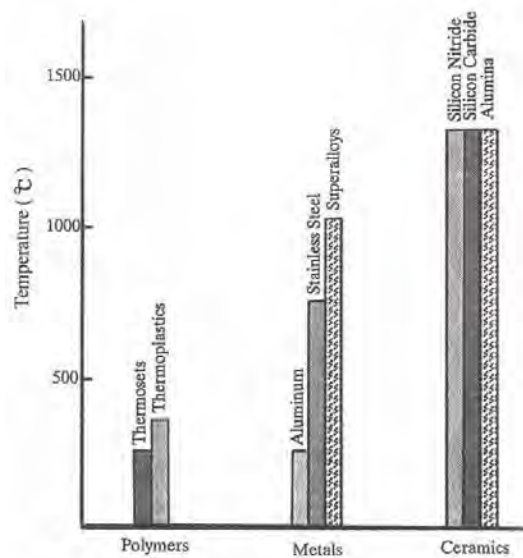
Figure 2.3: Typical service temperatures for polymers, metals, and ceramics [13]

2.4 Methods to Increase Fracture Toughness

Ceramic strength is a function of fracture toughness and flaw size as seen in Equation (2.1)[20]. One manner to increase ceramic material strength is to increase fracture toughness. Several design philosophies for increasing CMC fracture toughness currently exist. One is a weak fiber-matrix interface that provides for crack deflection in a dense matrix. This mechanism allows cracks to grow through the matrix but due to weak fiber-matrix interface, cracks are deflected around the fiber. If, however, a strong fiber-matrix interface was present, the crack would be allowed to propagate through the fibers unimpeded and, thus, have a lower fracture toughness. This unimpeded crack propagation would lead to undesired catastrophic failure like a monolithic ceramic rather than graceful failure sought out with the use of CMCs[13]. Trials of fiber coatings to create a weak fiber-matrix interface have been used in SiC-SiC CMCs[13]. These coatings, such as Monazite (lanthanum phosphide) have been used in oxide-oxide CMCs, but resulted in fiber degradation[11].

8

$$\sigma_f = \frac{K_{IC}}{Y\sqrt{c}} \qquad (2.1)$$

Another design to increase fracture toughness is a porous matrix oxide-oxide CMC. In a porous matrix oxide-oxide CMC, the bonds between the oxide fibers and the oxide matrix are very strong, but cracks are deflected away from the fibers due to the porosity of the matrix. In this case, the porosity of the matrix, as opposed to a the weak fiber-matrix interface, is used as the crack deflection mechanism. Without an interphase layer, an oxide-oxide CMC with a dense matrix would exhibit a strong fiber-matrix interface and lack the porosity needed as a crack deflection mechanism required for increased fracture toughness [13]. Selecting a matrix material that resists densification and retains porosity is another key to increasing high temperature fracture toughness in porous matrix oxide-oxide CMCs[21]. These concepts can be seen illustrated in Figure 2.4.
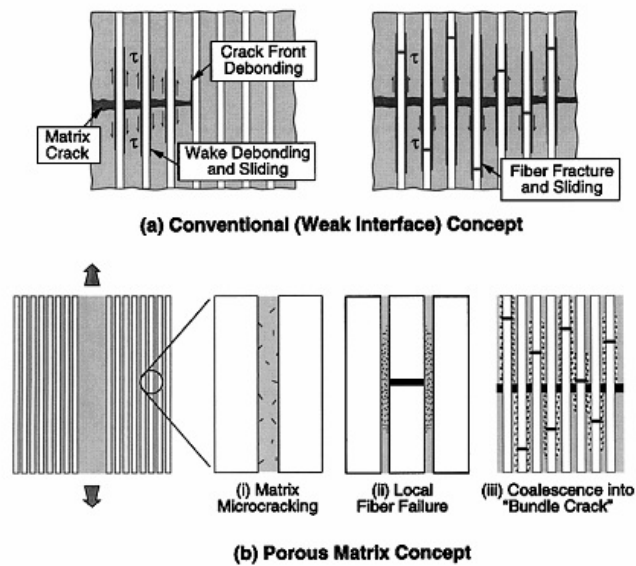
Figure 2.4: Mechanisms for increasing damage tolerance: a) conventional weak fiber interface in dense matrix b) porous matrix concept with strong fiber interface[48]

9

2.5   Oxide/Oxide CMCs

Silicon carbide fibers are some of the most popular CMC reinforcements[25]. This popularity is due to the ability of SiC-SiC composites to operate in temperatures as high as 1400°C. These materials are well-suited for liquid propellant rocket motors and turbine engine parts for several reasons. SiC-SiC CMCs demonstrate a high specific strength, thereby decreasing component weight. Additionally, because of their high maximum use temperature, SiC-SiC components do not require cooling which eliminates the requirements for heavy cooling systems[13]. Despite excellent high temperature properties, SiC composites are known to exhibit oxidation embrittlement. Performance degredations are caused by oxidation embrittlement at temperatures as low as 500°C in steam[12]. Matrix cracks allow the environment to interact with fibers and fiber coatings. Steam or other oxidizing environments accelerate oxidation embrittlement. Cyclic loading in an oxidating environment is thought to increase fiber and fiber coating oxidation rate. Accelerated degredation is thought to be a result of reaction gases being expelled from matrix cracks during unloading and the oxidizing environment being drawn into the composite during reloading[39]. This performance degredation illustrates limits to non-oxide CMCs.

Recent efforts have turned to porous matrix oxide-oxide composites which, without fiber coatings, can be utilized successfully in high-temperature oxidizing environments such as exhaust washed turbine engine components[30]. One example of an exhaust-washed structure is a commercial jetliner turbine engine exhaust nozzle and centerbody pictured in Figure 2.5. Nextel$^{\text{TM}}$ 720 fibers consist of 85% alumina and 15% SiO_2 by weight. Other fibers with higher strength have been used in oxide-oxide CMCs. Nextel$^{\text{TM}}$ 610 fibers are one such example. However, Nextel$^{\text{TM}}$ 720 fibers investigated in this study have a higher creep resistance and temperature stability compared to Nextel$^{\text{TM}}$ 610

10

fibers[2]. Nextel^{TM} 720 fiber and Nextel^{TM} 720/AS CMC properties are listed in Table 2.1 and Table 2.2, respectively.

Figure 2.5: CMC turbine engine exhaust nozzle and centerbody (Courtesy Boeing)

Property	Nextel^{TM} 720
Filament Diameter (μm)	10-12
Tensile Strength (GPa)	2.1
Modulus (GPa)	260
Density (g/cm^2)	3.4
Coefficient of Thermal Expansion (ppm/$^{\circ}$C)	6.0

Table 2.1: Mechanical properties of Nextel^{TM} 720 fibers[2]

Material	Fiber Volume	Matrix Volume	Porosity	Density
	(%)	(%)	(%)	(g/cc)
Nextel™ 720/AS	45.6	29.5	24.9	2.60

Table 2.2: Properties of the Nextel™ 720/AS composite used in this research[2]

2.6 Previous Biaxial (Tension-Torsion) Research on Oxide-Oxide Thin-Wall Tubes

Thin-wall tube specimens are more difficult to test than uniaxial specimens. To achieve successful test results, more than one load channel must be controlled simultaneously. Additionally, more data must be reduced and presented in a logical fashion which is not as straightforward as uniaxial testing. Biaxial testing, however, better simulates actual loading condition seen by aerospace materials. This is especially of concern with composites where off-axis loading conditions can lead to sub-standard performance.

Five requirements for the biaxial (tension-torsion) testing of thin-walled tubes have been presented by Daniel and Ishai in their text *Engineering Mechanics of Composite Materials*. These requirements are as follows:

1. The tube must be loaded without constraints that would produce local extraneous or nonhomogeneous stresses.

2. Surface pressures on the laminate in the test section, used for producing circumferential or axial stresses, should be minimized to avoid adding a high radial stress component resulting in a triaxial state of stress.

3. Functional or material failures of the load introduction tabs must be avoided.

4. Undesirable buckling prior to material failure must be avoided.

5. The cost of specimen fabrication, equipment, and testing process must not be prohibitive.

Uniaxial tests are more common than biaxial tests because of the requirements outlined by Daniel and Ishai. Despite the additional testing burdens, biaxial tests have, however, been accomplished in both tension-torsion with tubes and in-plane with cruciform specimens. These experiments all required procedural development and most experimental setups experienced failures in one or more of Daniel and Ishai's thin-walled tube biaxial (tension-torsion) testing requirements before achieving successful results[19][26][29][31][42]. While extensive uniaxial test results of Nextel^{TM} 720/AS layups exist, a relatively few number of multiaxial test results have been reported on. Searches of biaxial (tension-torsion) test results on oxide-oxide CMCs reveal no results. The present study aims to add to the contributions of multiaxial CMC testing.

This study set out to develop the test methodology for biaxial (tension-torsion) testing of thin-walled CMC tubes.

2.7   Thesis Objective

In a typical CMC component used in a high temperature aerospace application, mechanical loading and thermal gradients combine to create biaxial states of stress. Biaxial stress in metals and other ductile materials has been well documented and understood and has led to the development of biaxial failure criterion such as von Mises and Tresca to predict ultimate loads in these materials. A suitable failure criterion for CMCs has not been established due to their low ductility and the relatively low quantities of data when compared to metals. The objective of this study was to develop a test methodology useful for collecting and analyzing the effects of biaxial stress on oxide-oxide CMCs. The methodology that was developed in the present study utilizes standard strain gage instrumentation as well as DIC to capture full field strain and deformation behaviors for incorporation into computational models. Additional predictive data was collected through uniaxial tests of flat specimens at room and elevated temperature (1100°C) in both air and steam.

III. Test Material and Specimen Geometry

Nextel[TM] 720/AS is an oxide-oxide CMC composed of Nextel[TM] 720 continuous fiber reinforcement and porous aluminosilicate matrix. Nextel[TM] 720-based CMCs have been extensively studied[24][41][38][40][37][35][36]. The present study investigates Nextel[TM] 720/AS, a particular CMC formulation developed by COI Ceramics. Nextel[TM] 720/AS comprises Nextel[TM] 720 fibers in a porous oxide aluminosilicate matrix. Nextel[TM] 720/AS has a matrix-limited short-term upper temperature limit of 1100°C[2].   The matrix-limited short-term upper limit is a result of the aluminosilicate's temperature-based phase transformation. At 1100°C, $2Al_2O_3$-$3SiO_2$ (Silicon spinel) transforms into $2(Al_2O_3$-$SiO_2)$+SiO_2 (Pseudomullite). The excess SiO_2 produced at high temperature gives allows for grain boundary slip which lowers the overall material strength[17].

Specimen geometries tested in this study included dogbone, straightsided, DNS, and thin-wall tube specimens. Due to the material expense and limited number of specimens, before testing the Nextel[TM] 720/AS specimens of each geometry, test procedures and protocols were refined in a build up approach using a more readily-available material. This approach increased the likelihood of experimental success. Aluminum alloy was used for uniaxial procedure development while PMC and alumina thin-wall tube specimens were used for biaxial (tension-torsion) gripping and test procedure development. Dogbone specimen test materials included aluminum alloy and Nextel[TM] 720/AS , straightsided specimens were exclusively Nextel[TM] 720/AS, and thin-wall tubular specimens included PMC, monolithic alumina, and involute oxide-oxide Nextel[TM] 720/AS CMC tubes.

3.1   Uniaxial Specimens

Dogbone and straightsided Nextel[TM] 720/AS specimens were machined from a single panel layup as shown in Figure 3.1. The large Nextel[TM] 720/AS involute panel was

fabricated using 8-harness (8H) satin weave Nextel^{TM} 720 cloth cut into two inch strips. Strips were stacked and offset by two millimeter. This offset creates the novel involute layup. Specimens machined from this panel were used to test uniaxial properties which were then used for comparison to the thin-wall tube involute specimens. The fabrication process can be seen graphically in the COI Ceramics-provided fabrication process in Figure 3.2. The process followed the fabric, prepreg, and layup process versus the fiber tow and filament winding process which are both shown in the diagram.
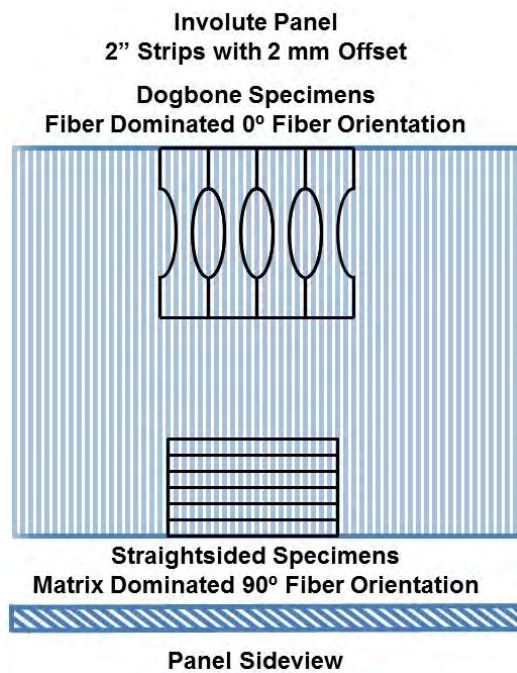
Figure 3.1: Nextel^{TM} 720/AS Dogbone and Straightsided Specimen Layups

The dogbone specimens, seen on the left in Figure 3.3, were cut in a 0°, fiber dominated orientation from the involute panel. The Nextel^{TM} 720/AS dogbone specifications can be seen in Figure 3.4. Straightsided specimens, seen on the right in Figure 3.3, were cut in a 90° orientation. The 90° orientation measured both a normal and

Oxide CMC Fabrication Process
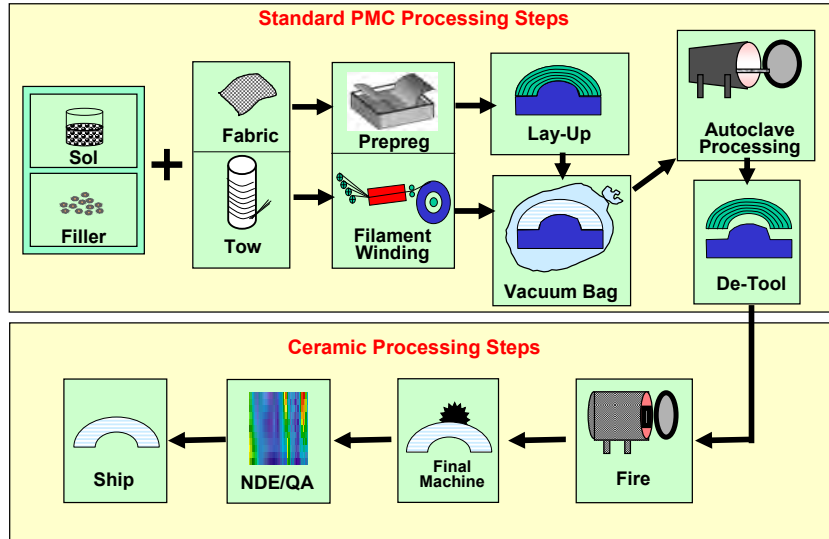
Figure 3.2: Prepreg processing steps of Nextel[TM] 720/AS composite

shear stress. The Nextel[TM] 720/AS straightsided specifications can be seen in Figure 3.7. The two specimen cut orientations to the fibers are illustrated in Figure 3.1.

Fiber orientation in the dogbone specimens, cut in the 0° direction with the involute panel ply stacking layup, can be seen in Figure 3.5. In contrast, fiber orientation of the straightsided specimens, cut 90° perpendicular to the involute panel ply stacking layup, can be seen in Figure 3.6. Thus, the 0° orientation displayed in the dogbone specimens of Figure 3.5 contain fibers that span the length of the specimens. Straightsided specimens do no have continuous fibers through the specimen length. Straightsided specimens are dependent more on the matrix-to-fiber load transfer mechanism. Because of the involute layup, this mechanism is subject to both a shear and axial stress when loaded along the

Figure 3.3: Nextel[TM] 720/AS dogbone (left) and straightsided (right) specimens
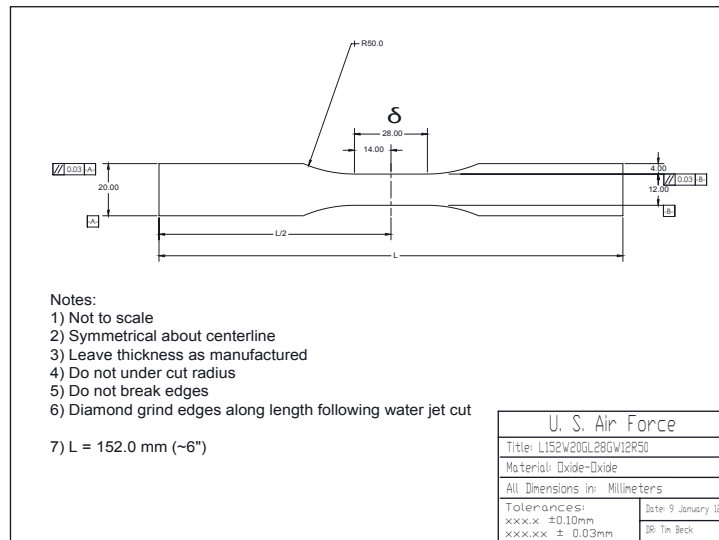
Figure 3.4: Nextel[TM] 720/AS dogbone specimen geometry specifications

length of the specimen. The 0° fiber orientation of Figure 3.5 is representative of the axial direction of the oxide-oxide CMC involute tube specimens whereas the 90° of Figure 3.6 exhibits the circumferential or torsion loaded direction of the oxide-oxide CMC involute tube specimens.
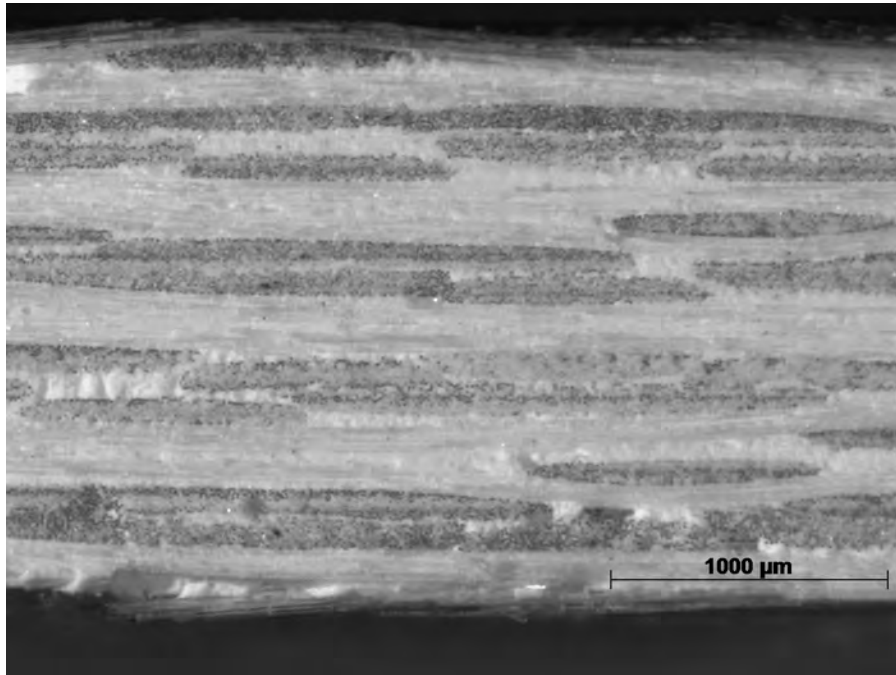
Figure 3.5: Nextel[TM] 720/AS dogbone ply (0° fiber dominated) layup (side view)

Before testing, fiberglass tabs were attached to the grip section of each uniaxial specimen using Vishay MicroMeasurments M-Bond 200 adhesive and catalyst (Vishay Micro-Measurements, Wendell, NC) as seen in Figure 3.8. Specimen tabbing was accomplished using a fiberglass tabbing material cut to cover approximately one inch of the grip section to fit in the MTS system grips. The fiberglass tabbing material served to protect the specimen from defect initiation due to specimen gripping. This defect introduction was of bigger concern on CMC specimens. The tabbing effort on aluminum alloy specimens was attempted for procedural development. Care was taken to ensure that the fiberglass tabs
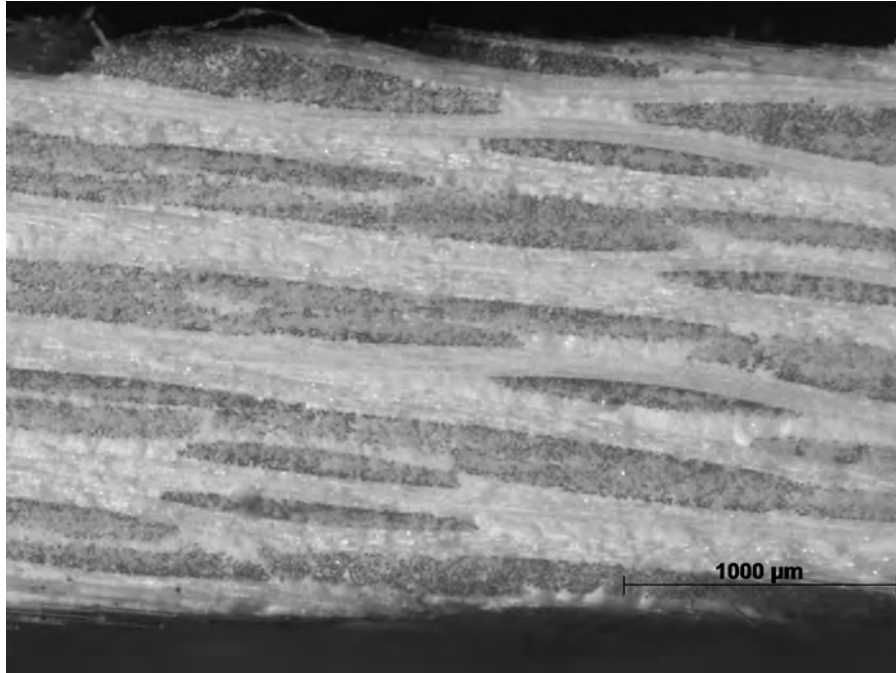
Figure 3.6: Nextel^{TM} 720/AS straightsided ply (90° matrix dominated) layup (side view)

did not extend past the exterior dimensions of the grip sections, yet covered the maximum gripping area.
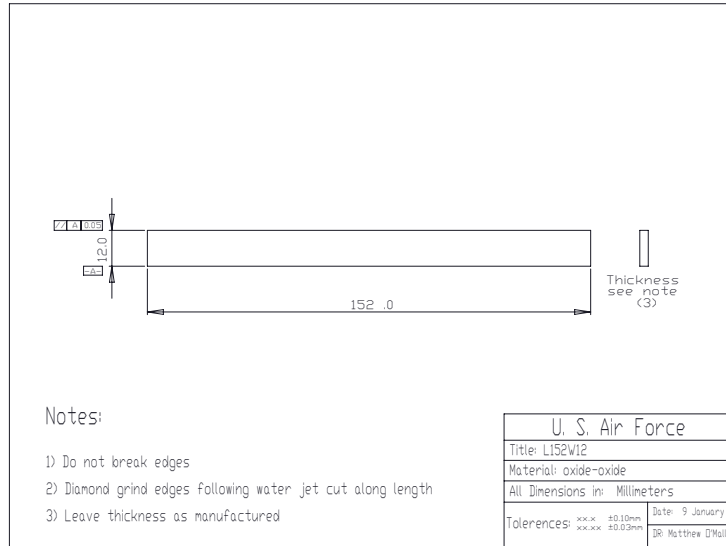
Figure 3.7: Nextel™ 720/AS straightsided specimen geometry specifications

Figure 3.8: M-Bond 200 Adhesive and Catalyst

3.2 Double-Notch Shear (DNS) Specimens

DNS specimens were used to measure ILSS, a matrix-dominated property. DNS specimens were machined per ASTM Standard C1425-05 from two remnant 6.25 inch x 6 inch sheets of Nextel^{TM} 720/AS (labeled as Panels C and B of the baseline panel in Figure 3.9). Figure 3.11 and Table 3.1 show the geometry and dimensions, respectively, for the specimens cut from the remnant panels (Panel C and B) of the balanced panel layup. Remnant sheet C and B possessed 0° fiber-dominated layup as seen in Figure 3.10. ASTM machining standard C1425-05 was chosen to create a specimen geometry that would test matrix-dominated ILSS properties. ILSS properties were compared to the shear values of straightsided specimens to estimate the properties of the biaxial (tension-torsion) oxide-oxide thin wall involute tubes.
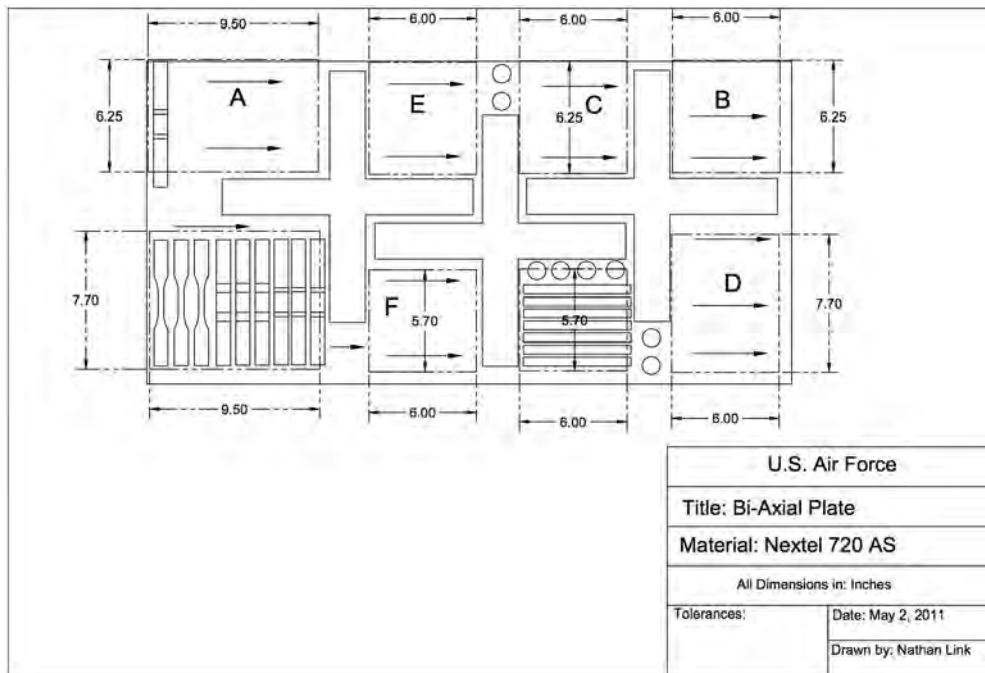
Figure 3.9: Baseline Nextel^{TM} 720/AS Balanced 0°/90° plate

DNS specimens were machined in-house at the Air Force Institute of Technology (AFIT) Model Shop using a diamond saw. Notch depth was determined through plate thickness. Per ASTM standard C1425-05, plate thickness is defined as t and thus t/2 is the midplane of the specimen. To test matrix dominated ILSS, both notches must be cut to the midplane (t/2) with a -0.00mm specification. Variations in plate thickness resulted in several of the 15 total specimens not meeting the -0.00mm t/2 specification. The influence of this tolerance is discussed later. The majority of specimens exhibited acceptable machining standards. After machining, DNS specimens were cleaned using the following procedure:

1. Five (5) minute ultrasonic deionized water bath

2. Seven (7) minute ultrasonic deionized water bath

3. Ten (10) minute ultrasonic acetone bath

4. Ten (10) minute ultrasonic acetone bath

5. Twenty-Five (25) minute ultrasonic acetone bath

6. Final acetone rinse

7. 100°C bakeout overnight (approximately 16 hours)

Ultrasonic cleaning with deionized water was conducted in order to remove residues and contaminates from the machining process. Five minutes was determined to be insufficient. A second iteration of seven minutes was also insufficient. Specimen cleaning with deionized water was thus determined to be insufficient. Ultrasonic cleaning in acetone was then conducted with better results. Cleaning results were determined by close visual inspection. Dogbone, straightsided, and tube specimens were subjected to chemical contamination removal at COI Ceramics through a bake-out procedure after processing.
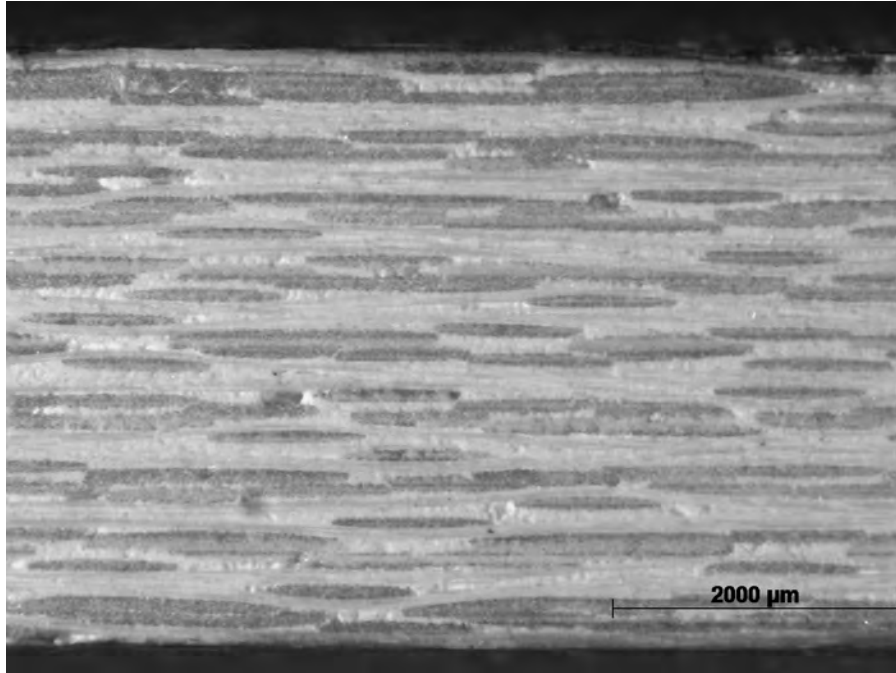
Figure 3.10: Nextel^{TM} 720/AS DNS ply layup (side view)

It should be noted that chemical contamination in remnant materials (Panels C and B in Figure 3.9) was not burned out by COI Ceramics after processing. Bake-out of remnant materials was performed at Air Force Research Laboratory (AFRL). During bake-out at AFRL, the specimens were placed on an alumina block to avoid thermal gradients from contact with the discontinuous metallic support rack and to minimize risk of damage that would result from accidental falls between the rack supports. Images of the DNS cleaning and bakeout process can be seen in Appendix A in Figure 6.9 through Figure 6.16.
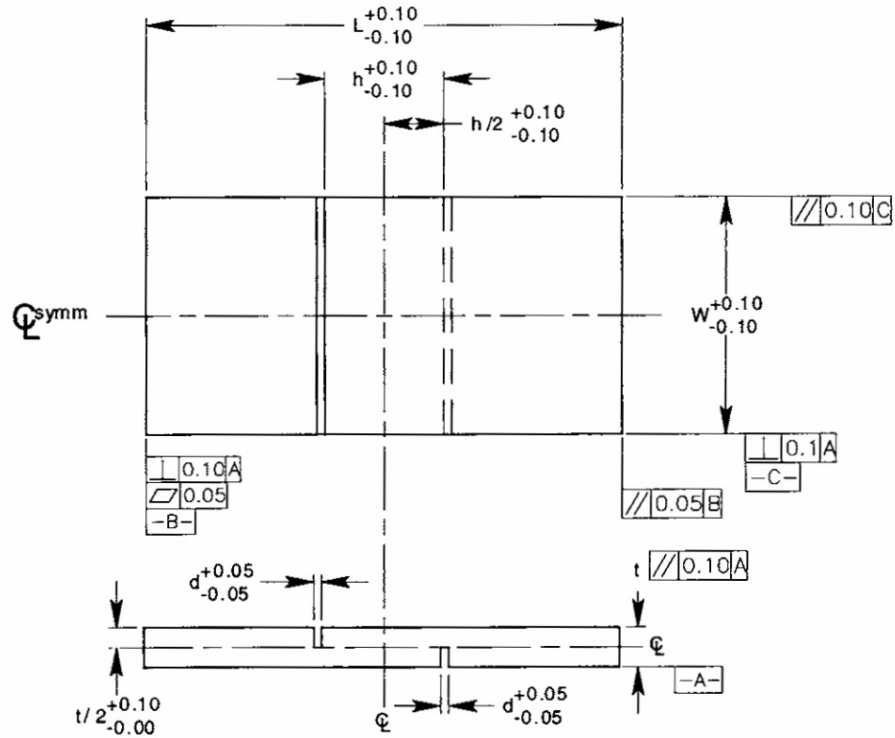
Figure 3.11: ASTM C1425-11 DNS specimen geometry. Reproduced from [9]

Dimension	Value (mm)
L	150
h	12
W	15
d	0.5
t/2	2

Table 3.1: Values for Figure 3.11

3.3 Thin-Wall Tube Specimens

The thin-walled involute oxide-oxide CMC tube geometry is a novel specimen layup, constructed by offset stacking strips of Nextel^{TM} 720/AS prepreg material. The involute tube walls were nominally 16 Nextel^{TM} 720/AS plies thick. Plies, were two inches (approximately 1/3 the circumference of the tube) in length and were assembled such that a ply end started on the tube outer diameter and terminated on the inner diameter. Figure 3.12 is a simplified visualization of the 54 total plies (arranged in a manner similar to that of a rolled newspaper). The layup exhibits excellent machinability and defect resistance to issues such as ply wrinkling. Fiber architecture was designed to support axial loads with fiber-dominated properties along the tube length. The involute architecture design produced a matrix-dominated interlaminar path from the inner diameter to the outer diameter. ILSS determination was a priority of this involute tube architecture study.
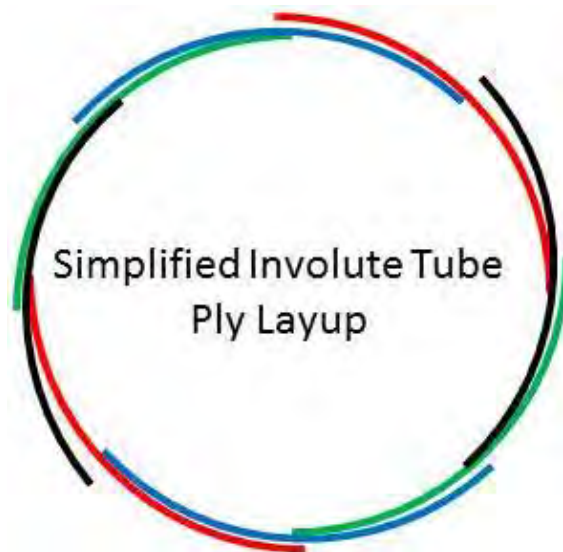
Figure 3.12: Biaxial (tension-torsion) thin-wall involute tube specimen layup

Specimens were machined to a total length of nine inches resulting in a 2.3 inch long grip section on each end, a central 3.38 inch gage section, and a 0.51 inch transition

zone separating each grip section from the gage section. Gage section outer diameter was machined nominally to 1.61 inches. Grip section outer diameter was machined to 1.75 inches. Tube dimensions and tolerances were in accordance with ASTM Standard E 2207-08 and are illustrated in Figure 4.14[10].

Gripping CMC tubes for biaxial testing is substantially more complex than for typical uniaxial coupon specimens. Gripping pressures were initially calculated based on MTS provided algorithms using material UTS and estimated coefficients of friction (μ). The algorithms estimated the pressure necessary to prevent specimen slip during a given applied load. Specimen damage resulting from gripping was of significant concern. The PMC tubes used in initial development to validate experimental setup exhibited sufficient ductility and toughness and were thick enough that specimen damage resulting from gripping was of little concern. The next stage in the test buildup process was gripping of the brittle alumina tubes. Gripping alumina tubes, the next step in test validation, was more challenging due to the brittle nature and thin walls.

A total of three alumina tubes were obtained from CoorsTek (Golden, CO) with dimensions and tolerances listed in Table 3.2. While alumina tubes met specifications, the tubes were nevertheless out-of-round, non-concentric, and non-uniform and presented challenges to subsequent machining to specifications in Figure 4.14. Tubes were ground on a Computer Numerically Controlled (CNC) lathe using diamond tooling on a tool post grinder. To minimize chance of machining-induced damage, the alumina was spun at 100 RPM and the tool post grinder was moved at 0.0005 inch/rev with 0.002 inch depth cuts per pass. Alumina specimens were cooled with biodegradable lubricating oil.

Aluminum alloy insert plugs were machined for both the alumina tubes and the oxide-oxide CMC involute tubes. The aluminum alloy plugs are shown in Figure 4.25. Dimensional drawings are shown in Figure 3.13. Outer diameter dimensions listed in Figure 3.13 are nominal and were modified to match each individual tube inner diameter.

Dimension	Specification (in)	Tolerance (in)
Length	9.000	±0.063
Outer Diameter	1.750	±0.088
Inner Diameter	1.500	±0.075

Table 3.2: Specifications and tolerances for CoorsTek AD-998 alumina tubes

The center-drilled hole was included to ensure that no pressure differential resulted from installation of the plugs due to an air-tight seal. A radius on the insertion end of the plug was created to minimize damage from insertion into the tube specimens. Overall length of the plug was 0.17 inch under the length of the specimen grip section. The outer diameter of the aluminum alloy plug was determined after the machinists at the AFIT Model Shop measured the inner diameter of each tube end. The aluminum plug was initially machined slightly oversized for the inner diameter. Plug diameter was stepwise reduced by machining 0.001" per step, until the plug was a slip fit. Due to the alumina tubes being out of round, the aluminum alloy plugs were fit with a gap of 0.005 inch to 0.007 inch. At this tolerance the out-of-round alumina tubes resulted in a tight fit between the aluminum plug and alumina tube. The center-drilled holes in the aluminum alloy plugs were threaded and a bolt inserted to maneuver the plugs in and out of the specimen ends.

Before testing, the aluminum alloy plugs were fixed in each grip end using epoxy (Hardman® Double/Bubble® Red Extra Fast Setting Epoxy Adhesive, All-Spec Industries, Wilmington, NC). In addition to affixing the aluminum alloy plug, the epoxy was used to fill the machining gap between the aluminum alloy plug and tube resulting in a more uniform load introduction. The aluminum alloy plug was affixed in place by mixing the epoxy, applying half of the mixed epoxy to the inner diameter of the tube just inside the specimen end, and half of the mixed epoxy to the outer diameter of the aluminum alloy

plug just past the radius cut. The plug was inserted with a twisting motion to ensure even spread of the epoxy within the tube. The plugs were inserted until flush with the ends of the tube by setting the tube down on a flat disposable piece of cardboard. Immediately after insertion and pressing the aluminum alloy plug flush with the specimen, an alcohol-soaked disposable paper towel was used to wipe the grip section to ensure excess epoxy was not spread onto the outer grip radius. The bottom face of the aluminum alloy plug was also wiped to remove any remaining excess epoxy. Once the epoxy was sufficiently cleaned from external surfaces, the tube with plug was stood on end on a clean section of flat cardboard for the remainder of the five minute cure time. After the cure time had elapsed, the opposing end aluminum alloy plug was set in accordance with the same procedure.
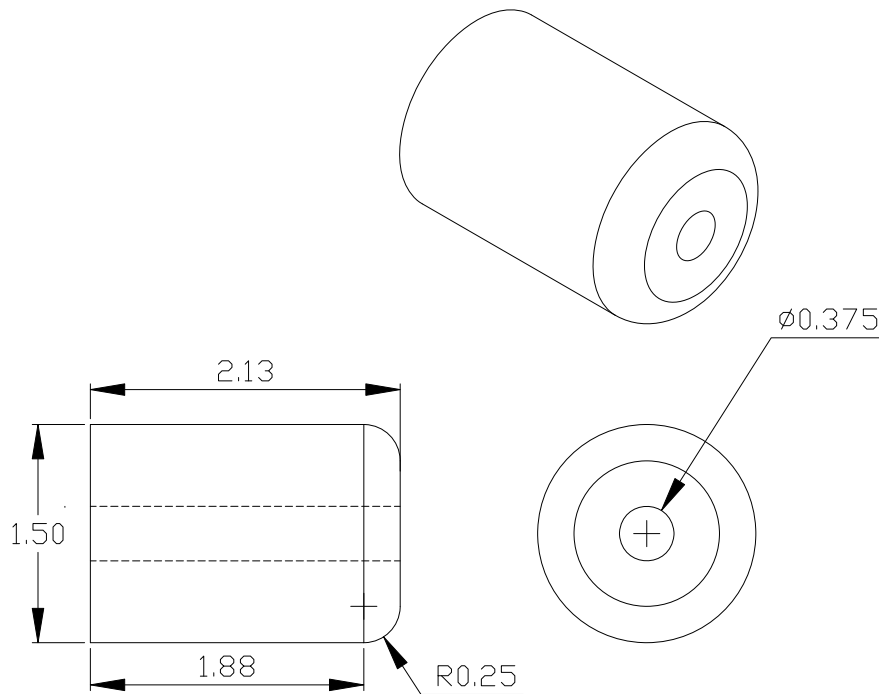
Figure 3.13: Aluminum alloy grip support plug inserts with nominal dimensions in inches

The alumina tubes presented a worst case scenario for gripping procedures. The lack of specimen and inner diameter uniformity presented the possibility of premature specimen failure due to thickness variation within the gage section. Alumina tubes were not used for data collection in this study. The non-circular cross section could lead to specimen failure from stress concentrations and invalid results if used for data collection. Due to the tighter tolerances and higher specimen uniformity of the oxide-oxide CMC involute tubes, it was believed that if alumina tubes were successfully gripped and tested, gripping pressures of the same values would be applicable to oxide-oxide CMC involute tube specimens.

Machining gaps ranged from 0.001" to 0.025" between the involute tube inner diameter and aluminum alloy plug outer diameter on the oxide-oxide CMC involute tube specimens. Vent holes were not required to be threaded for a bolt in the CMC specimen aluminum alloy plugs. The aluminum alloy plugs were fixed to the CMC test specimens in the same manner as alumina tube specimens.

IV.   Experimental Setup and Procedures

This study included uniaxial and biaxial (tension-torsion) tests on Nextel^{TM} 720/AS CMC specimens. Uniaxial flat-plate coupon tests were used to determine UTS and USS values prior to biaxial (tension-torsion) testing. UTS and USS values were used in biaxial (tension-torsion) thin-wall tube specimen failure strength envelope estimations. All tests were conducted in the mechanical testing lab at the Air Force Institute of Technology.

4.1   Room Temperature Uniaxial Tests

Uniaxial aluminum alloy dogbone specimens were studied first for procedure development and vetting in addition to risk reduction. Nextel^{TM} 720/AS dogbone and straightsided specimen studies followed. These studies were conducted using a servo-hydraulic controlled MTS 810 Material Test System 3 kip mechanical loadframe. The MTS loadframe was outfitted with an MTS Force Transducer (Model 661.19E-04) with hydraulic wedge grips and was controlled by a Flextest 40 digital controller connected to a computer with MTS Station Manager software installed. A high-temperature MTS extensometer (model number 632.53 E-14) with a gage length of 0.5 inch was used to measure strains throughout the tests. The complete test apparatus can be seen in Figure 4.1.

The loadframe's hydraulic system was warmed up prior to testing with a displacement-controlled sine waveform of 0.5 inch for at least 30 minutes. After warm up of the hydraulic system was completed, the specimens with load tabs were then inserted into the hydraulic wedge grips. Grip pressure was set to 8 MPa based on previous work on Nextel^{TM} 720/A[24]. Gripping pressure of 8 MPa ensured sufficient pressure to prevent slippage, yet was low enough to prevent specimen crushing[24].
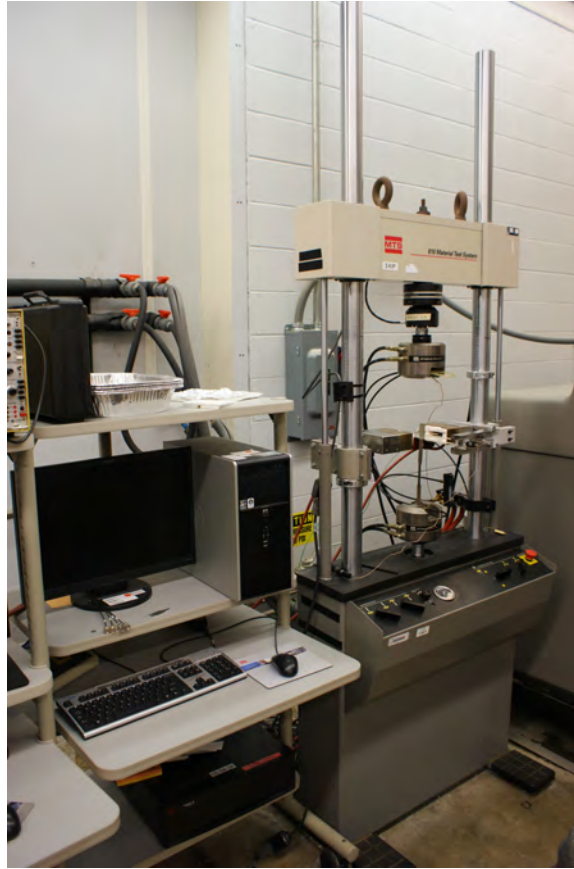
Figure 4.1: MTS 3 kip loadframe

4.1.1   Aluminum Alloy Dogbone Specimen Testing

Stock aluminum alloy dogbone specimens, previously prepared and available in the AFIT lab, were used to develop and test experimental procedures to be used on the Nextel^{TM} 720/AS specimens. Aluminum alloy specimens were prepared by measuring the width and thickness of the gage section. Following measurements, indentions were created on the sides of the specimens using a manual punch and hammer. Indentions were used for mounting the low-contact force, high-temperature MTS Model 632.53 E-14 high temperature extensometer. Indentions were aligned using a previously made and available punch alignment template. During the indention process, the specimen was held in a wooden jig, also previously fabricated.

The crosshead and hydraulic actuators were positioned in displacement control to grip approximately one inch of the specimen grip section while centering the gage section relative to the extensometer arm. The aluminum alloy specimen was loaded into the MTS loadframe with care taken to align the punched indentions with the extensometer mounting bracket. The specimen was loaded into the grips by placing the top and bottom grip sections firmly against the alignment posts to ensure vertical orientation in line with the applied loading force. The top grip was closed after placing the aluminum alloy specimen firmly against the alignment posts. The load cell was zeroed out, the MTS actuator arm was switched to load control, an input of zero force was input, and the lower grip was closed.

Studies were completed in load control with loading rates of 2 MPa/second to initiate fast fracture. Data was acquired at 30 Hz and time, actuator displacement, strain, and force were recorded. The loads were applied in 50 MPa cycles to failure with unloading occurring after each loading increment (e.g. 0 MPa to 50 MPa, unload to 0 MPa, load to 100 MPa, unload to 0 MPa, load to 150 MPa, etc.). When test procedures were finalized and successfully executed on the aluminum alloy specimens, tests on oxide-oxide specimens proceeded.

To determine applied loads and loading rates, a spreadsheet was developed based off of dogbone and straightsided specimen geometry. This spreadsheet is shown in Figure 4.2. Loads were calculated using Equation (4.1). It should be noted that while SI units were used for all analysis, loadframe limits were listed in kip. For test safety, loads were calculated in kip to ensure that loadframe limits were not exceeded.

$$\sigma = \frac{P}{A} \qquad \qquad (4.1)$$

where

$$\sigma = \textit{Axial Stress} \text{ (Pa)}$$

$$P = \textit{Axial Force} \text{ (N)}$$

$$A = \textit{Cross-sectional Area} \text{ (m}^2)$$

Specimen ID	Desired Stress, σ (MPa)	Width, w (mm)	Thickness, t (mm)	Area, A (m²)	Force, P (kip)
Nextel 720/AS (Spec Geo) - 12-XXX	2	11.96	1.97	2.36E-05	0.011
	3.5	11.96	1.97	2.36E-05	0.019
	5	11.96	1.97	2.36E-05	0.026
	10	11.96	1.97	2.36E-05	0.053
	20	11.96	1.97	2.36E-05	0.106
	25	11.96	1.97	2.36E-05	0.132
	80	11.96	1.97	2.36E-05	0.424
	50	11.96	1.97	2.36E-05	0.26484
	100	11.96	1.97	2.36E-05	0.52968
	150	11.96	1.97	2.36E-05	0.79452
	200	11.96	1.97	2.36E-05	1.05935
	250	11.96	1.97	2.36E-05	1.32419
	300	11.96	1.97	2.36E-05	1.58903
	350	11.96	1.97	2.36E-05	1.85387
	400	11.96	1.97	2.36E-05	2.11871

Figure 4.2: Dogbone and straightsided specimen load spreadsheet

4.1.2 *Nextel^{TM} 720/AS Dogbone Specimen Testing*

Nextel^{TM} 720/AS dogbone specimens were prepared and loaded in a similar manner as the aluminum alloy specimens, but without the creation of indentations. Brittle CMCs do not withstand indentations as ductile aluminum alloys. Indenting CMCs would cause extensive damage to the specimen leading to premature failure. The surface finish of the edge of the CMC, however, provided enough friction force to hold the extensometer against the specimen under test with the rods' conical ends. The top grip was closed and the low-contact force extensometer was installed with the alumina tips onto the side of the Nextel^{TM} 720/AS specimen. After extensometer mounting, the load cell was zeroed out,

the MTS actuator arm was switched to load control, an input of zero force was input, and immediately the lower grip was closed.

Nextel^{TM} 720/AS dogbone specimens were tested to failure at room temperature with monotonically increasing load at 4 MPa/second. Data was acquired at 30 Hz and time, actuator displacement, strain, and force were recorded.

4.1.3 *Nextel^{TM} 720/AS Straightsided Specimen Testing*

Straightsided specimen geometry were prepared from Nextel^{TM} 720/AS panels. Specimens were loaded in displacement control at 0.05 mm/second to initiate fast fracture. Testing of straightsided specimens was completed in the same manner as for Nextel^{TM} 720/AS dogbone specimens. Straightsided specimens lack a defined gage section in contrast with dogbone-shaped specimens. As a result, the extensometer was centered on the overall length of the straightsided specimen, rather than the gage section.

The MTS Station Manager procedure can be seen in Appendix A, Figure 6.1. This procedure incorporated an Aramis DIC 5V TTL 1/sec trigger signal. The 5V TTL 1/sec trigger signal was programmed into the MTS Station Manager procedure as an output and fed into a triggerbox trigger input in the Aramis DIC system. The Aramis DIC system was then set to detect the signal and begin a 1/sec image acquisition procedure. For non-DIC tests, this step in the procedure was removed or disabled.

4.2 Room Temperature Uniaxial Tests with Digital Image Correlation (DIC)

Material testing with the addition of DIC was accomplished in the second phase of testing. The addition of a stochastic, or random, speckle pattern, as seen in Figure 4.3, was the only additional specimen preparation. Speckle patterns were painted to enable the use of GOM Optical Measuring Techniques' Aramis DIC software suite as an additional full field measurement technique. The DIC random speckle pattern was created by applying a solid coating of flat white spray paint and then applying an incomplete, speckled layer of flat black spray paint for speckling. Both spray paints were commercially available.

34

The DIC system consisted of a pair of tripod-mounted Schneider Kreuznach Componon-S 2.8/50 50 mm aperture cameras mounted at an angle of 21.6° and run with Aramis DIC software version v6.0 2-6 (Build 2007-09-06). Calibration of the Aramis system was completed with a GOM 65x52mm calibration panel and can be seen in Figure 4.4. Facet size of 11 pixels and step size of 7 pixels was used. Specifications for the ceramic calibration panel can be seen in Table 4.1. Calibrations ultimately yielded a correlation coefficient that was compared with Aramis standards. Per the Aramis user manual, a correlation coefficient between 0.01 and 0.04 pixels indicates a correct calibration. Correlation coefficients for tests in the present study were between 0.023 pixels and 0.031 pixels, within Aramis guidelines.

Figure 4.3: Example stochastic, or random, speckle pattern for use with DIC

DIC tracks the deformations of a specimen during mechanical loading by correlating movement of the speckles on the surface through a series of images. If deformations are in a single plane, movements can be tracked via a single camera. If out-of-plane deformations

Figure 4.4: GOM 65x52mm DIC calibration panel

Panel ID	P04895
Distance	39.003mm/1.5355in
Certification Temperature	20.0°C
Expansion Coefficient	0.10×10^{-6} K^{-1}
Measurement Temperature	20.0°C

Table 4.1: GOM 65x52mm DIC calibration panel specifications

are of interest or are of significant value, the use of a two camera system is necessary. Biaxial (tension-torsion) testing, which involves out of plane loading, was the ultimate goal of this experimentation and thus a two camera system was used. Additionally, a two camera DIC system allowed for the out-of-plane deformations and strains to be mapped during the build-up uniaxial tests.

Speckle size of the stochastic pattern is important to the correlation of the specimen deformations. Rajan et al. (2012) formulated the relationship that the subset size should be three times the speckle size. DIC system evenly breaks the field of regard into the subsets dictated by the user. Each subset, in essence, acts as a single strain gage. The smaller the speckle size is, the smaller the subset size will be. The relation of speckle to subset size relates to the fidelity or spatial resolution of the system. The smaller the speckle size the higher the spatial resolution and vice versa. In an effort to achieve a stochastic pattern with the smallest speckle size, several iterations of speckle painting was done on aluminum alloy dogbone specimens. Once a suitable technique was found, the Nextel^{TM} 720/AS dogbone and straightsided specimens were both prepared in the same manner as for the standard uniaxial tests, but with the addition of the random speckle pattern.

Nextel^{TM} 720/AS dogbone uniaxial test procedures incorporating DIC required time synchronization to compare experimental loads and strains between the MTS loadframe and Aramis DIC system. The Aramis system possessed two analog-to-digital recording channels and a trigger input via a trigger box. The MTS loadframe possessed digital-to-analog outputs. Coaxial cables connected the MTS loadframe axial load and strain channels to the Aramis system triggerbox for recording. Synchronization was achieved with a 5V TTL signal connected via coaxial cable from MTS loadframe to the Aramis trigger box. The 5V TTL trigger signal then was initiated at test start via the MTS Station Manager software and triggered every second for the test duration. The Aramis system was set to receive the 5V TTL signal and record an image set. The test was completed in load control with loading rates of 2 MPa/second to initiate fast fracture. Data was acquired at 30 Hz and time, actuator displacement, strain, and force were recorded. The sequentially loaded tension loads were applied in 50 MPa cycles to failure with unloading occurring after each loading increment (e.g. 0 MPa to 50 MPa, unload to 0 MPa, load to 100 MPa, unload to

0 MPa, load to 150 MPa, etc.).The MTS procedure can be seen in Appendix A, Figure 6.4 and the sequentially loaded tension test profile can be seen in Figure 4.5.
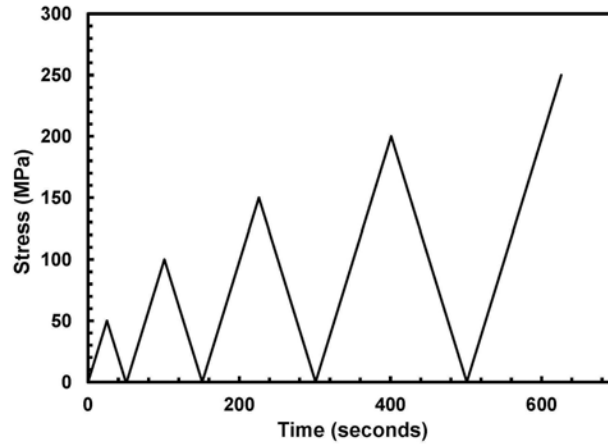
Figure 4.5: Sequentially-loaded dogbone tension test profile

4.3 Elevated Temperature (1100°C) Uniaxial Nextel^{TM} 720/AS Dogbone and Straight-sided Specimen Testing

Temperature calibration was accomplished prior to elevated temperature testing. A dogbone specimen was instrumented with two type-R thermocouples protected by ceramic beading and attached in similar fashion to previous works by Laffey and Pope[24][32]. Thermocouples were attached with high temperature piano wire wound around two grooved CMC pieces securing the thermocouple beads to the specimen. This setup can be seen on a DNS specimen in Figure 4.6. The specimen was then loaded into the MTS test frame, set in a zero load hold condition, and furnace temperature raised until 1100°C was measured and maintained on both left and right side of the specimen. Temperature was measured with an Omega CL3515A digital hand thermometer as seen in Figure 4.10. The setpoints of the furnace were then recorded and used for subsequent 1100°C air test temperature runs.

38
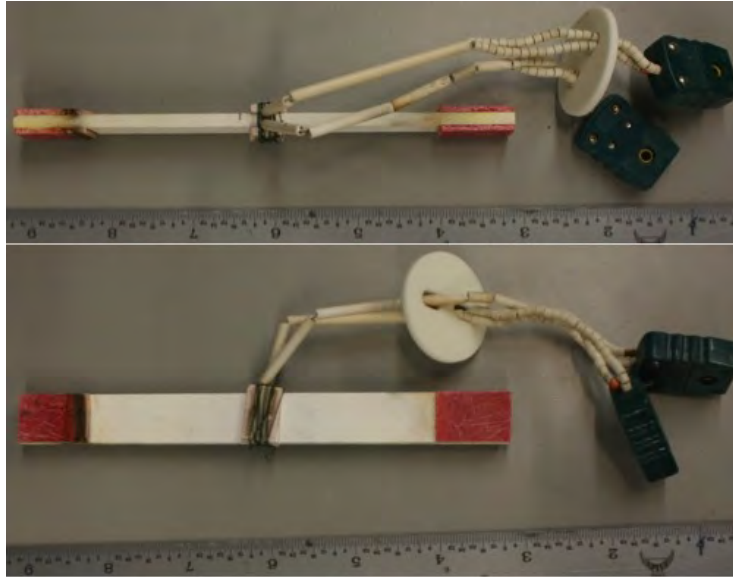
Figure 4.6: Temperature calibration specimen setup with piano wire wound around two CMC pieces securing thermocouple beads on DNS specimen used to determine setpoints for 1100°C testing in air and steam

Following temperature calibration, dogbone specimens were loaded in both monotonic and sequentially loaded tension to failure tests. The specimens were heat soaked at 1100°C in a zero load condition before loads to failure were applied. Straightsided specimens were also heat soaked prior to testing in 0.05 mm/sec displacement-to-failure loading. MTS Station Manager procedures for both dogbone and straightsided specimens can be seen in Appendix A, Figure 6.5 and Figure 6.6, respectively.

Procedure additions from room temperature testing included temperature ramp, dwell, and shutoff segments as well as zero-load-hold conditions during temperature ramp and dwell times. Temperature ramp increased test specimen temperature from room temperature to 1100°C. Dwells held the 1100°C temperature for the 30 minute dwell period. Shutoff segments brought specimen temperatures back to room temperature at the conclusion of testing.

4.4 Elevated Temperature (1100°C) Uniaxial Nextel^{TM} 720/AS Double Notch Shear (DNS) Specimen Testing

Monotonic compression to failure and interlaminar shear creep tests were conducted to DNS specimens at 1100°C. Loads and elevated temperatures were applied with a 5 kip servohydraulic-controlled MTS 810 Material Test System to impart desired stress levels based on DNS specimen geometry. Loads were determined with a spreadsheet shown in Figure 4.7 similar to dogbone and straightsided specimens and calculated using Equation (4.2). The MTS loadframe was controlled by a Flextest 40 digital controller connected to a computer with MTS Station Manager software installed as seen in Figure 4.8. The 5 kip loadframe was equipped with water cooled wedge grips and an AMTECO Hot Rail two-zone resistance-heater furnace connected to a temperature controller for each zone (left and right). An R-type thermocouple was inserted into each zone to measure temperature and provide temperature controller feedback. The MTS Model 409.83B Temperature Controller was used to control the furnace operating temperature and controlled both the left and right furnaces independently and simultaneously. Each zone utilized a display with two readouts in a stacked arrangement. The type-R thermocouple-measured temperature was displayed on top and the MTS programmable temperature setpoint was displayed below as seen in Figure 4.9.

$$\sigma = \frac{P}{WL} \tag{4.2}$$

where

$$\sigma = Axial\ Stress\ \text{(Pa)}$$

$$P = Axial\ Compressive\ Force\ \text{(N)}$$

$$W = Specimen\ Width\ \text{(m)}$$

$$L = Fracture\ surface\ length\ \text{(m)}$$

Specimen ID	Desired Stress, σ (MPa)	Width, w (mm)	Thickness, t (mm)	Area, A (m²)	Force, P (kip)	Nominal Fracture Surface Length (in)	Nominal Fracture Surface Length (m)	Nominal Fracture Surface Area (m²)
Nextel™ 720/AS DNS Specimen X	1	14.90	3.99	5.95E-05	0.013365	0.46875	0.01190625	0.000177403
	2	14.90	3.99	5.95E-05	0.026730			
	3.5	14.90	3.99	5.95E-05	0.046778			
	5	14.90	3.99	5.95E-05	0.066826			
	10	14.90	3.99	5.95E-05	0.133651			
	20	14.90	3.99	5.95E-05	0.267302			
	30	14.90	3.99	5.95E-05	0.400954			
	40	14.90	3.99	5.95E-05	0.534605			
	50	14.90	3.99	5.95E-05	0.668256			
	60	14.90	3.99	5.95E-05	0.801907			
	75	14.90	3.99	5.95E-05	1.002384			

Figure 4.7: DNS load spreadsheet
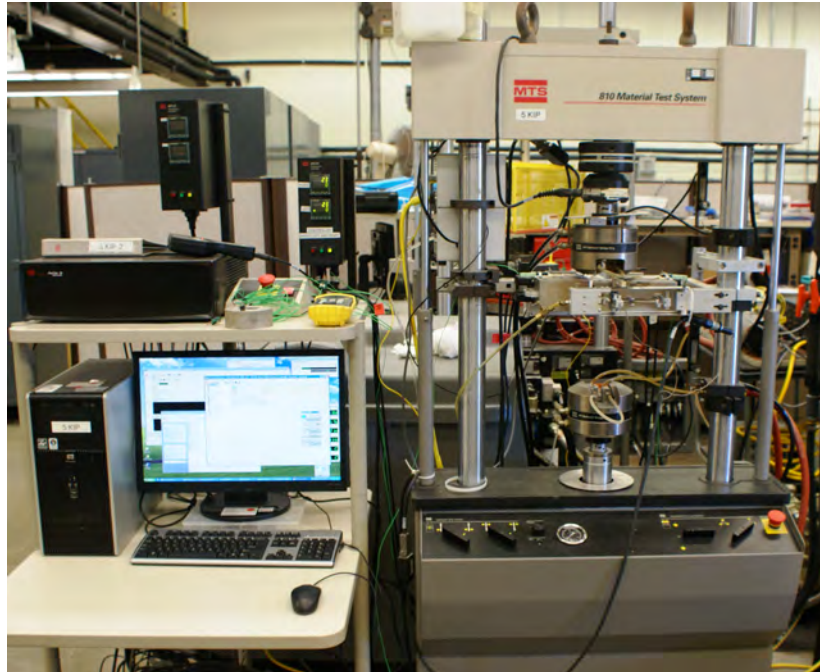
Figure 4.8: MTS 5 kip high-temperature loadframe

Temperature calibration was performed prior to experimentation in the 1100°C testing environment. A temperature calibration specimen of the same Nextel™ 720/AS material and geometry to be tested was mounted using a similar procedure as above. The

Figure 4.9: MTS 409.83 Temperature Controller

temperature calibration was run in load control with zero load. The specimen was straddled by two R-type thermocouples connected to an Omega CL3515A digital, hand thermometer as seen in Figure 4.10. The furnace temperature was gradually raised until the temperature calibration specimen reached the target testing temperature of 1100°C. Once steady state 1100°C temperature was observed for two hours, the corresponding temperature setpoints were recorded. The same procedure was repeated in both steam and air. Set points for corresponding tests were then used for subsequent testing. Temperature calibrations were reaccomplished whenever alumina insulation or furnace igniters were replaced.

Two safety-of-test mechanisms were in place for compressive load tests. A failure detector developed and described by Laffey comprised the first safety mechanism[24]. This failure detector preserved test specimen fracture surfaces. The second safety mechanism provided furnace crush protection from the lower hydraulic actuator or upper grip. Furnace crush protection was accomplished by raising the furnace rail support to a height outside of the damaging range of the hydraulic actuator. A sufficient amount of range remained
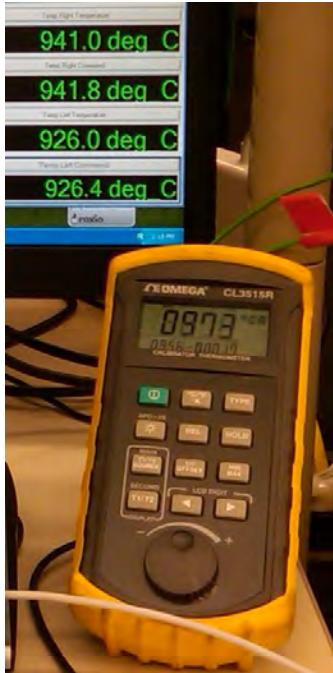
Figure 4.10: Omega CL3515A digital, hand thermometer during temperature calibration

for compressive loads to be applied without enough throw to reach the furnace bottom. Similarly, the upper crosshead was raised to allow downward travel of the upper grip during specimen release without reaching the furnace top.

The loadframe's hydraulic system was warmed up prior to testing by running a displacement-controlled sine wave of 0.5 inch for a minimum of 30 minutes. Fiberglass tabs were attached to the grip section of each specimen using M-Bond 200 (Vishay Micro-Measurements, Wendell, NC) adhesive and catalyst as discussed above. Tabbed grip sections were inserted into the hydraulic wedge grips following warm up. An alumina susceptor, seen in Figure 4.11, was used to separate the saturated steam environment (for steam tests) from the laboratory air within the furnace. The susceptor was an alumina cylinder with holes for both extensometer rods as well as a steam port located on the opposite side of the cylinder. The grips were cooled with 15°C water from a Naslab model HX-75 chiller. Grip pressures were set to 8 MPa. An AMTECO Steam Generator was

used to generate steam when required for steam tests and is displayed in Figure 4.12. Each furnace half was closed around the susceptor after specimen mounting inside the susceptor and grips. After the furnaces were closed, an MTS Model 632.53 E-14 high temperature extensometer was mounted to measure strain during testing. It should be noted that the strain measurement by the extensometer was not the actual interlaminar shear strain, but change in gage section length per unit original gage section.
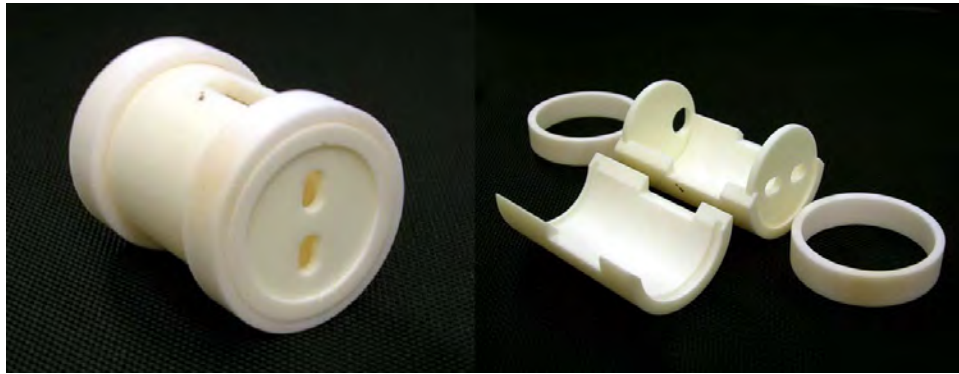
Figure 4.11: Alumina susceptor used for high temperature (1100°C) steam testing assembled (L) and disassembled (R)

Loads were applied after elevated temperatures were reached and held for 30 minutes. Zero-load hold conditions were maintained during temperature ramp-up. Monotonic compression tests were carried out at elevated temperatures in laboratory air. Interlaminar shear creep tests were accomplished both in air and steam. Procedures for interlaminar shear creep tests in steam differed only by the addition of steam generator warmup and operation prior to DNS specimen loading. Both the monotonic compression and interlaminar shear creep procedures can be seen in Appendix A, Figure 6.2 and Figure 6.3, respectively.

Figure 4.12: AMTECO HRFS-STMGEN Steam Generation System

4.5   Biaxial Tests

Biaxial (tension-torsion) tests were performed at room temperature (nominal value of 23°C) in laboratory air environment. A servo-controlled MTS 809 Axial-Torsional Testing System pictured in Figure 4.13 mated with an MTS TestStar IIm digital controller was used with TestStar IIm Station Manager software (version 5.3B 3243) for computerized testing and data acquisition.

Thin-walled PMC tubes were studied first for procedure development and vetting in addition to risk reduction. These surplus PMC specimens from previous experimentation were used for test setup and procedure maturation. Alumina tubes were then instrumented and tested. Alumina was used to verify test instrumentation and procedures were appropriately setup for testing with a brittle material. Finally, Nextel[TM] 720/AS CMC involute tubes were tested.

Figure 4.13: MTS 809 Axial-Torsional Testing System

Alumina and CMC tube specimen specifications can be seen in Figure 4.14. All thin-walled tube specimens were instrumented with Vishay Precision Group Micro-Measurements series L2A-03-250LW-350 linear and C2A-03-250LR-350 rectangular rosette strain gages. Eleven channels of strain gages were used to capture involute tube strain responses in areas of interest, to vet the Aramis DIC system, and provide risk mitigation from strain gage application errors or premature delamination. Five (5) total linear gages were used, with three gages comprising a "homemade" 45° rectangular rosette located in the center of the involute tube, 180° circumferentially opposed from the Aramis DIC pattern. The remaining six (6) channels were used for two preprinted 45° rectangular rosettes, located 90° circumferentially from the center homemade rosette. The strain gages were connected to strain gage conditioners and connected to the MTS Test Star IIm controller for recording per Figure 4.15.
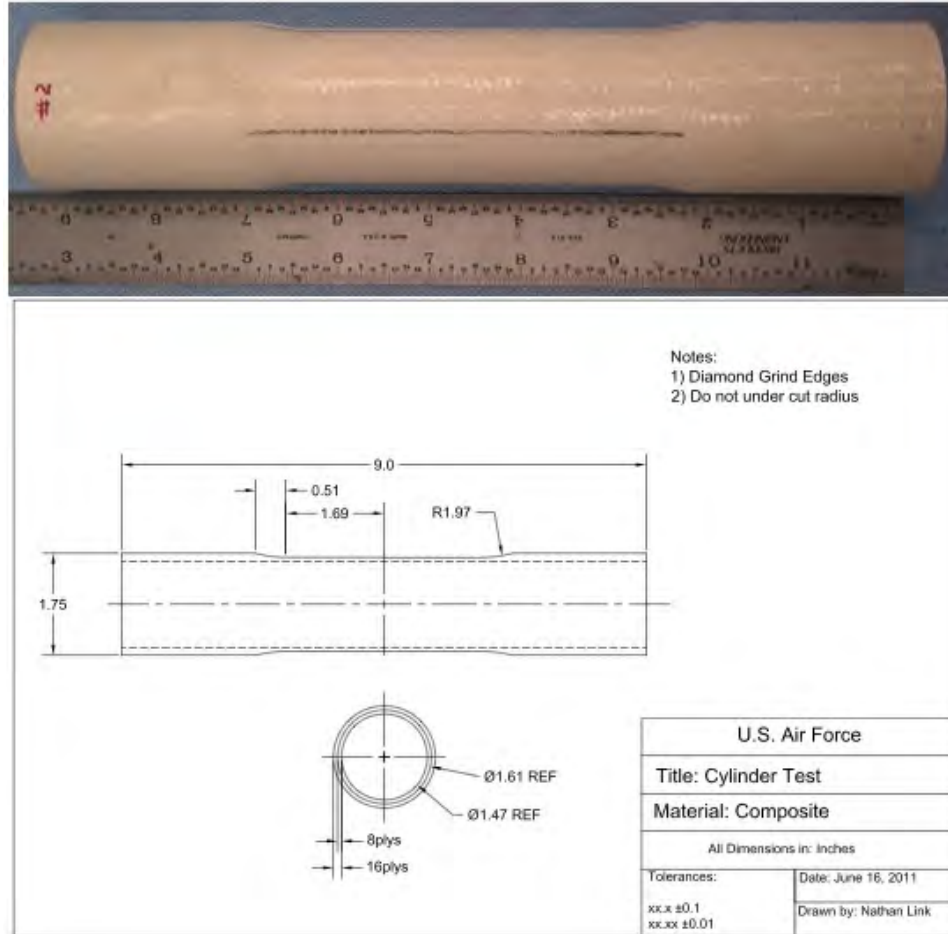
Figure 4.14: Nextel^{TM} 720/AS thin-wall involute tube specimen with strain gage alignment mark (above) and specifications (below)

Gages were selected based on performance specifications and availability from Micro-Measurements–350Ω resistance strain gages were selected. An excitation voltage of 0.5V was used. High resistance and low excitation voltage were selected to reduce thermal effects on gages. As seen in Figure 4.16, five linear and two rectangular rosette strain gages were used to measure axial, torsion, and shear strains. Two linear gages were placed circumferentially to measure torsion at opposite ends of the tube and three linear strain gages were used to create a "homemade" rectangular strain gage rosette with one gage aligned axially, one gage circumferentially, and one gage at a 45° angle to both the axial
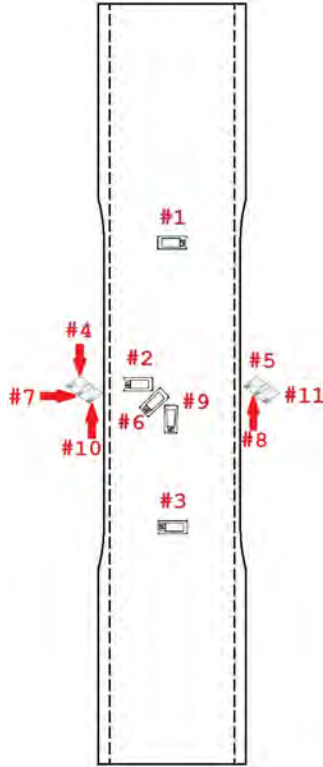
Figure 4.15: Oxide-oxide CMC involute tube strain gage locations

and torsional gages. The homemade rectangular strain gage rosette was installed 180° (circumferentially) from the DIC random speckle pattern. This orientation was used for verification and validation of DIC test data. The homemade rectangular strain gage rosette was used in lieu of a manufactured rectangular strain gage rosette for risk reduction of strain gage debonding.

Strain gages were installed using a modified installation procedure provided by Micro-Measurements. High amounts of degreasing, sanding, and cleaning dictated by Micro-Measurements for common metals such as steel and aluminum alloys were difficult to accomplish without introducing significant surface defects or leaving cleaning products residuals such as strands of textiles or paper byproducts from cleaning and drying products on the surface of the CMC. The following procedure was adopted and subsequently
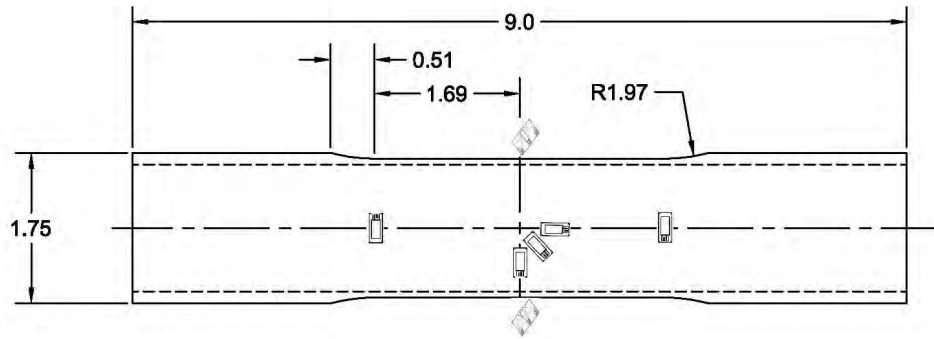
Figure 4.16: Strain gage locations (dimensions in inches)

modified from Daniel J. Knapke via Phil Blosser both of University of Dayton Research Institute (UDRI) for use with CMCs:

1. Lightly sand (one to three passes maximum) surface to remove high points on surface using 320 or 400 grit SiC paper. Do not try to sand flat.

2. If possible, clean the surface with isopropyl alcohol.

3. Draw pencil lines for orientation of gage through center (x and/or y as necessary).

4. Remove the strain gage from package and place face up on a smooth, flat, clean glass surface.

5. Apply Vishay PCT-2M tape over the top of the gage with at least 1 additional length of tape on both sides of the gage.

6. Remove the tape with the gage from the surface and apply the gage to the marked specimen, aligning the arrows to the alignment marks.

7. Adjust the position of the gage by moving the tape as needed for proper alignment.

8. Peel back the tape until all the gage is off the surface.

9. Apply a very light application of M-Bond 200 catalyst to the back of the gage and wait one minute to drying.

10. Apply M-Bond 200 adhesive to the specimen surface under the gage and apply the tape and strain gage while keeping proper alignment.

11. Hold application pressure for two minutes with a finger in place over the tape and strain gage

A bank of 11 rack-mounted Vishay Precision Group Model 2300 Signal Conditioning Amplifiers (SCAs), seen in Figure 4.17 were used to provide 0.5V excitation voltage to 350Ω strain gages and condition the signal before input to the MTS system for recording. The SCAs were setup in accordance with provided documentation to balance the system prior to calibration followed by calibration and finally balance of the strain gages immediately prior to testing. Calibration was done with a Vishay Wheatstone-Bridge Simulator model 1550A Strain Indicator Calibrator[4]. SCAs were calibrated from ±10V at $0.0005\frac{\epsilon}{V}$ which provided a range of ±0.5%ϵ. The 11 SCAs were then wired to the Test Star II controller analog to digital converter cards. Two cards were installed and available and each card would accommodate up to six input channels.

Figure 4.17: Bank of Vishay 2310 rack-mounted strain gage signal conditioning amplifiers

Input from strain gages to SCAs was done via a three-wire connection using a true quarter Wheatstone Bridge (internal dummy) setup, pictured in Figure 4.18. The internal dummy setup was used due to the automatic leadwire resistance correction from the three-wire circuit [1]. Strain gage lead wires were connected to the SCAs via wire jumpers seen in Figure 4.19. The SCAs were connected to the jumpers via three-wires terminated with a Bendix PT06A-14-15(SR) connector designed to a MIL-C-26482 connector. All 11 MIL-C-26482 connectors were modified from from 120Ω to 350Ω setups. The MIL-C-26482 connector pin arrangement can be seen in Figure 4.20 and the associated wiring diagram can be seen in Figure 4.21. This required desoldering wire from pin B in Figure 4.20 and resoldering to pin C.
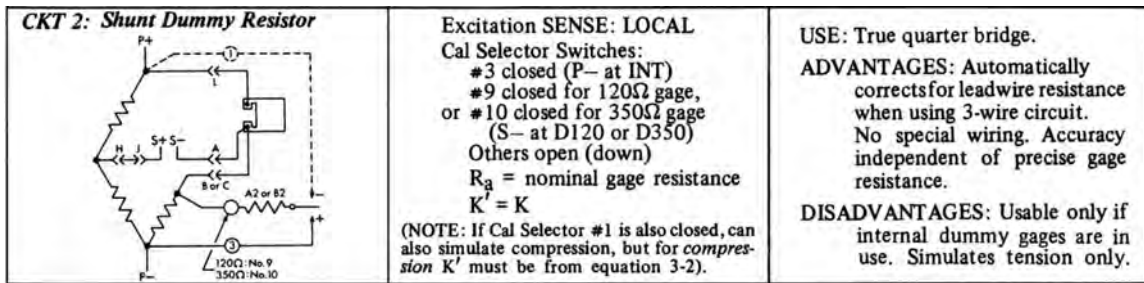
Figure 4.18: Quarter-bridge strain gage setup[1]

Strain gage application was accomplished first on the PMC tubes. Strain gage setup and instrumentation procedures were vetted with the successful SCA setup and strain gage installation followed by test data collection with the PMC tubes. Strain gage application and use procedures were then applied to alumina test specimens. One alumina specimen test was accomplished with strain gage instrumentation alone. The subsequent alumina specimen test used the same strain gage instrumentation and the addition of a DIC stochastic, or random, speckle pattern and Aramis software suite as an additional
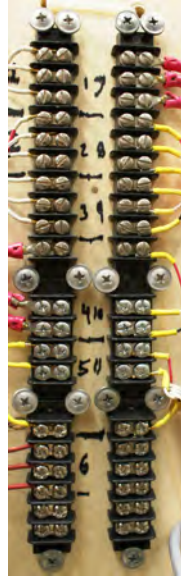
Figure 4.19: Wire jumpers to signal conditioning amplifiers
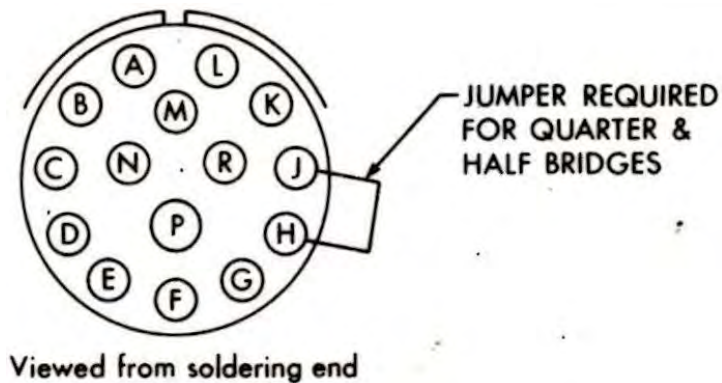
Figure 4.20: MIL-C-26482 standard connector pin arrangement to signal conditioning amplifiers[1]

full field measurement technique. DIC was used in a similar fashion as the uniaxial test procedures. Two different trial procedures for creating the DIC random speckle pattern using standard black laser printer toner ink powder and airbrush techniques were carried out. Alumina tube specimens were painted with a sufficient layer of flat-white standard
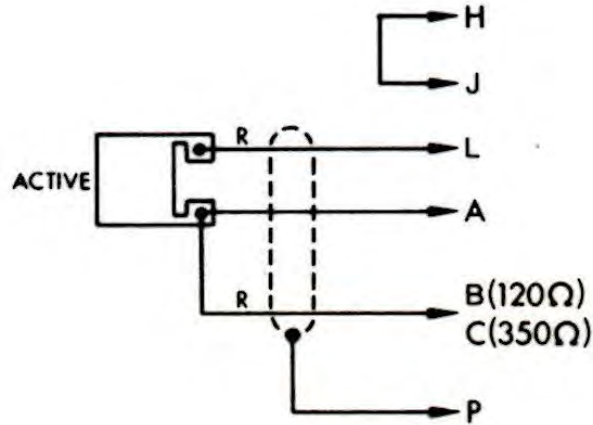
A1. INTERNAL DUMMY

Figure 4.21: Wiring diagram from strain gage to MIL-C-26482 standard connector pin[1]

household spray paint to achieve a uniform white background. Once the white paint was dry, laser printer toner ink powder was filtered through a 74 μm and 149 μm sieve stacked together as pictured in Figure 4.22. A 1/2" wide artist's brush was lightly dipped into a jar of toner powder. Speckling was accomplished by gently brushing the powder through the sieve stack consisting of 74 μm and 149 μm sieves while moving the stack evenly over the area of interest. As the rate of speckles falling through the sieve decreased, the sieve stack was lightly tapped repeatedly and moved over the speckling area. This process was repeated until a sufficiently speckled surface was achieved. The process in progress can be seen in Figure 4.23 while the end result can be seen in Figure 4.24. It must be noted that sufficient care was required to ensure that bumping of any sort was kept to a minimum to prevent toner from being discharged from the surface area of interest. Laser toner provided higher contrast and smaller speckles than the spray painted speckle patterns, both traits that were highly desirable for this test setup.

Figure 4.22: Standard sieves used for brushing black laser printer toner powder through for uniform stochastic speckle patterns

Figure 4.23: Laser printer toner speckling procedure on involute oxide-oxide CMC tube
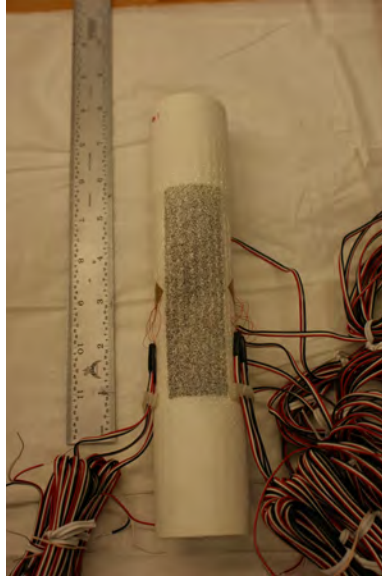
Figure 4.24: Laser printer toner speckling on involute oxide-oxide CMC tube NOTE: this pattern was not used

It was initially thought that the CMC specimens would provide a naturally sufficient white background, eliminating the need for a white paint layer for laser toner speckling. However, unlike the alumina specimens, the laser printer toner did not adhere to the CMC tube surface as the toner did to the painted alumina specimens. As a result, the random speckle pattern was spray painted on the involute oxide-oxide tubes in the same manner as the uniaxial aluminum alloy and Nextel$^{\text{TM}}$ 720/AS dogbone and straightsided specimens with a flat black speckle pattern painted over a flat white background.

After specimen preparation, biaxial (tension-torsion) testing was completed as follows:

1. Set and enable applicable MTS axial and torsional load/displacement limits

2. Connect strain gage(s) to signal conditioning amplifier(s), turn on for warm-up

3. Calibrate DIC (Aramis)

4. Install test specimen in upper grip with speckle pattern aligned to DIC (Aramis)

5. Align DIC (Aramis) field of view (FOV) with test specimen

6. Verify DIC (Aramis) correlation with speckle pattern using two images

7. Establish strain noise floor for Aramis (can use correlation verification images)

8. Balance (zero) strain gage(s) signal conditioning amplifier(s)

9. Perform the following steps as quickly as possible in order:

    a. Switch to manual command - axial load = 0 kip, torsion torque = 0 in-kip

    b. Grip lower grip

    c. Turn off manual command

10. Balance (zero) strain gage(s) signal conditioning amplifier(s)

11. Turn off applicable MTS axial and torsional load/displacement limits

12. Execute test (Run MPT program)

4.6 Biaxial (Tension-Torsion) Test Method

4.6.1 Build Up Approach

Uniaxial tests at room temperature were conducted on Nextel$^{\text{TM}}$ 720/AS dogbone and straightsided specimens to determine involute layup properties. UTS in the axial direction for the involute tubes was estimated with uniaxial dogbone involute coupon tests. USS in the circumferential direction for the involute tubes was estimated with uniaxial straightsided involute coupon tests. Dogbone and straightsided involute coupons were prepared for characterization using DIC. The DIC system was vetted by this process and was used as a full field measurement system. This was accomplished in a build up approach to compare DIC against extensometer strain measurements. With reasonable

strain agreement between DIC and extensometer data, the DIC system could then be used for full field strain measurement on the biaxial (tension-torsion) test specimens. Uniaxial tensile testing was also conducted at 1100°C on dogbone, straightsided, and DNS specimens. Results were used to predict high-temperature performance of involute CMC tubes[28].

4.6.2 *Digital Image Correlation (DIC)*

Aramis DIC system is a non-contact optical technique used to measure surface displacements and strain fields of a test specimen subjected to an external stimulus, which in the present research was a mechanically applied tensile load. DIC was developed in the 1980s as numerical computing was becoming available by M.A. Sutton and others at the University of South Carolina (USC)[29]. In a typical DIC tests, a high-contrast speckle pattern is created on the surface of the test specimen. Displacements are obtained by capturing images of the speckles during a load application and comparing displacement of speckles at each image to the original, unloaded, position. Strains are obtained by differentiating displacement fields with strain resolutions of 10^{-4} or less. DIC is an excellent full field strain measuring technique due its full field strain resolution. CMCs undergo non-uniform deformation during loading due to their heterogeneous architecture. Non-uniform deformation among fiber tows can be seen in uniaxial testing with CMCs. DIC's full field strain measurement and high strain resolution gives a higher probability of capturing damage initiation and failure progression during loading. Resolution of DIC is influenced by speckle, facet, and subset size and is determined by the individual user and calibration. Data collected from DIC can then be used to formulate high-fidelity computational models of oxide-oxide CMCs. Strain gages and extensometers have a lower probability of capturing discrete damage events and measure average strain over a discrete, localized areas. DIC has a higher probability than strain gages or extensometers

of capturing discrete damage events and measuring localized strains anywhere within its field of regard[33].

4.6.3 Challenges and Objectives

Through collaboration with project sponsors at AFRL, Daniel and Ishai's biaxial (tension-torsion) list of requirements listed in *Previous Biaxial (Tension-Torsion) Research on Oxide-Oxide Thin-Wall Tubes* was carefully considered and risk reduction carried out. Previous researchers found that buckling was a challenge for similar types of experiments[7]. Anti-buckling devices in the previous tests were used to overcome the buckling challenges. Due to the high modulus of the oxide-oxide CMC tube in this study, the risk of gage section buckling was determined to be low and no external anti-buckling devices or mechanisms were used during testing. Due to the elimination of any anti-buckling or other external support mechanisms that would contact the external surface of the tube, chance of extraneous or nonhomogeneous stresses on the outside of the tubes was reduced. Additionally, specimen geometry and MTS collet grip design provided loading exclusively through grip sections. Several other tests experimented with load introduction tab geometries often with sophisticated reinforcements or gripping procedures[26]. Load introduction for this effort was accomplished through the use of aluminum alloy plug inserts custom machined and epoxied in to take up the machining tolerances between the CMC tube and aluminum alloy plug. Care was taken to have enough epoxy to fill the gap in a uniform fashion. Additional measures were taken to prevent test result influence due to excess epoxy as seen by Liao et al[26]. Careful consideration was taken to not use an excess quantity of epoxy that would span across the tube diameter allowing crack propagation and thus premature tube failure outside the gage section.

Three test setup parameters posed the biggest challenges to biaxial (tension-torsion) testing. Specimen development and manufacture, gripping the test specimens, and specimen failure outside of the gage section. Specimen development and manufacture in
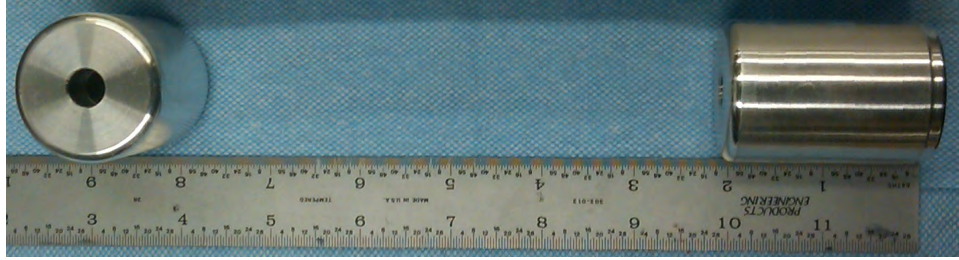
Figure 4.25: Aluminum alloy grip support plug inserts custom machined to each tube end to prevent grip section crushing during alumina and oxide-oxide CMC tension-torsion testing

the present study required approximately one year to complete (including six months of fiber architecture development and six months of fabrication) and was carried out by the project sponsors at AFRL and COI Ceramics, an ATK Aerospace Affiliate, in San Diego, California. Small specimen diameters would be desirable to minimize material costs and enable the use of smaller test stands. Minimum tube diameters are required due to the brittle nature of the ceramic fibers when they are wrapped to form the tube circumference. Diameter limits increase test resource requirements including the machinery required for the biaxial (tension-torsion) tests, raw materials, and machining required including tooling and layup machinery. This manufacturing process presents a non-trivial task for wound-type tubes. An innovative layup similar to a fanning of a deck of cards was proposed and used by COI Ceramics. This layup allows for a machining option to obtain smaller radii per a specified design. This also allows for a more conventional biaxial (tension-torsion) tube design with a reduced gage section and thicker gripping sections on the specimen top and bottom with a transition zone of a set machined radius between the grip and gage section as seen in Figure 4.14. Time and fiscal resource requirements for tube manufacture are significantly higher than flat uniaxial tensile coupons.

Gripping the test specimens required special attention. MTS collet grip estimation algorithms were provided. Collet grip estimation algorithms were intended for use with

aluminum and steel alloys where, due to ductility, crushing of the specimens is of less concern. Care was taken to avoid crushing of CMC grip sections during gripping procedures while ensuring grip pressures were high enough to prevent slipping during loading. Ensuring the appropriate gripping pressure required careful analysis of forces derived from preliminary uniaxial tests and a build-up risk reduction approach. Uniaxial tests were conducted to estimate required loads during biaxial (tension-torsion) testing. The load numbers were then input into the grip pressure estimation algorithms. Once the grip pressure estimates were obtained, specimens were gripped at 67% of estimated gripping pressure. Upon successful gripping at 67% of estimated gripping pressure, the specimen was gripped at 83% of estimated grip pressure. The 83% grip estimation pressure was used for specimen loading. No slipping was observed during modulus checks at 83% grip estimation pressure and the 83% grip estimation pressure was used for the remainder of testing.

Gripping pressure was determined through the use of MTS-provided grip pressure estimation calculations given in grip model 646.25 documentation[5]. This spreadsheet is shown in Figure 4.26 and was first used for grip estimation on alumina tube specimens. It was concluded by the resultant grip pressure estimates that each estimate was generated based on reaching the UTS for axial loads, USS for torsion loads, and reaching both maximum axial and torsion loads for biaxial (tension-torsion) loading. As a result, it was concluded that the estimated grip supply pressure was an overestimate, however, within reason. An attempt to build up grip pressure starting from 2 MPa was unable to be completed due to the fidelity of the grip supply pressure gage. The scale of the installed gage was 0 to 80 MPa. The lowest possible setting due to fidelity was 4 MPa. Alumina specimens were gripped successfully without grip section failures at 4 MPa. A higher setting of 5 MPa was then successfully testedand used for the remainder of testing.

MTS Series 646 Hydraulic Collet Grips Product Information				
Model 646.25				
Grip Pressure Constants				
A	B	Cr = Cn	µc-s	µg-c
174.8 cm2	52.4 kN/MPa	0.146 MPa/kN	0.13	0.06
27.1 in2	81.3 psi/lb	0.0946 psi/lb		

Axial Load to be Applied to the Specimen During Test		
Published Alumina UTS (MPa)	248	
Alumina Tube Specimen 1 Minimum Area (m2)	0.000119769	
Alumina Tube Specimen 1 Force (kN)	29.70258987	
Alumina Tube Specimen 1 Force (lbf)	6677.407835	
Estimated Grip Supply Pressure		
P = sqrt(L2+(2T/D)2)Cn		
Alumina - Specimen 1 - Axial	P = 4.336578121	MPa
Alumina - Specimen 1 - Torsion	P = 4.517692995	MPa
Alumina - Specimen 1 - Biaxial	P = 6.262224828	MPa
Clamping Force Applied to Specimen		
Alumina - Specimen 1 - Axial	Fc = 227.237 kN	Quick Estimate
Alumina - Specimen 1 - Torsion	Fc = 236.727 kN	Quick Estimate
Alumina - Specimen 1 - Biaxial	Fc = 328.141 kN	Quick Estimate
	Fc = 328.416 kN	More Accurate Estimate

Pressure on Grip Section		
Coorstek AD-998 Alumina Compressive Strength - 2500 MPa		
A = 2πrh		
A = 0.005807548 m2		
Alumina - Specimen 1 - Axial	σ = 39.12781892 MPa	
Alumina - Specimen 1 - Torsion	σ = 40.76197143 MPa	
Alumina - Specimen 1 - Biaxial	σ = 56.5024294 MPa	

Estimated Alumina Tube Shear Moment		
USS (MPa) 293.9		
Shear Moment Estimate (in-lb) 6110.029356	Upper	
Shear Moment Estimate (N-m) 690.3406214	Upper	

Figure 4.26: Biaxial (tension-torsion) grip pressure estimation spreadsheet developed from MTS provided grip estimation algorithms and constants

The last, but most important, challenge was obtaining test article failure within the specimen gage section. The most common technique used to drive failure in a known gage section is through a reduction in the cross-sectional area from the grip to the gage section. The section of the test article where the reduction in cross sectional area occurs is the transition zone. In ductile materials, such as metals and polymers, plastic yielding prevents stress concentrations from exceeding failure strength in this transition zone[15]. Due to the brittle nature of monolithic ceramics and CMCs, this plastic yielding mechanism

is not present thereby making it difficult to obtain test article failure within a gage section. Failure inside the gage section is required for accurate measurements and analysis of the failure loads and mechanisms. Oftentimes failures in brittle thin-walled tubes occur outside the gage section in either the transition zone or the gripping section.

A load spreadsheet was developed to determine biaxial (tension-torsion) test specimen loads, independently, which was required for calculating stress based off of specimen gage section geometry. This spreadsheet is shown in Figure 4.27.

| Specimen ID | Torsion | | | | | | Axial | | |
	Desired Stress, τ (MPa)	Outer Diameter, D_o (mm)	Inner Diameter, D_i (mm)	Radius, r (mm)	2d Moment of Inertia, J (m^4)	Torque, T (in-kip)	Desired Stress, σ (MPa)	Area, A (m^2)	Force, P (kip)
Thin-Wall Tube - Specimen X	2	41.08	39.18	20.54	4.82463E-08	0.042	2	0.00012	0.054
	3.5	41.08	39.18	20.54	4.82463E-08	0.073	3.5	0.00012	0.094
	5	41.08	39.18	20.54	4.82463E-08	0.104	5	0.00012	0.135
	10	41.08	39.18	20.54	4.82463E-08	0.208	10	0.00012	0.269
	20	41.08	39.18	20.54	4.82463E-08	0.416	20	0.00012	0.539
	25	41.08	39.18	20.54	4.82463E-08	0.520	25	0.00012	0.673
	80	41.08	39.18	20.54	4.82463E-08	1.663	80	0.00012	2.154
	50	41.08	39.18	20.54	4.82463E-08	1.039	50	0.00012	1.346
	100	41.08	39.18	20.54	4.82463E-08	2.079	100	0.00012	2.693
	150	41.08	39.18	20.54	4.82463E-08	3.118	150	0.00012	4.039
	200	41.08	39.18	20.54	4.82463E-08	4.158	200	0.00012	5.385
	250	41.08	39.18	20.54	4.82463E-08	5.197	250	0.00012	6.731
	300	41.08	39.18	20.54	4.82463E-08	6.237	300	0.00012	8.078
	350	41.08	39.18	20.54	4.82463E-08	7.276	350	0.00012	9.424
	400	41.08	39.18	20.54	4.82463E-08	8.316	400	0.00012	10.770

Figure 4.27: Biaxial (tension-torsion) load spreadsheet with independent axial load and torsion torque calculations.

Axial loads recorded during testing were used to calculate axial engineering stress. Calculation of axial stress from axial load was done using standard methods as shown in Equation (4.3).

$$\sigma = \frac{P}{A} \tag{4.3}$$

where

$\sigma = $ *Axial Stress* (Pa)

$P = $ *Axial Force (N)*

$A = $ *Cross-Sectional Area* (m^2)

For simplicity, for the remainder of the document, the term "axial stress" will be used to indicate "axial engineering stress." Axial displacement recorded during testing was used to calculate strain. Calculation of axial strain from axial displacement was done using standard methods as shown in Equation (4.4).

$$\epsilon = \frac{\Delta L}{L_0} \tag{4.4}$$

where

$\epsilon = $ *Axial Engineering Strain* $(\frac{\text{mm}}{\text{mm}})$

$\Delta L = $ *Axial Change in Length* (mm)

$L_0 = $ *Original Length* (mm)

Torsional loads (torque) recorded during testing were used to calculate shear stress. Calculation of shear stress from torque was done using standard methods as shown in Equation (4.5).

$$\tau = \frac{T\rho}{J} \tag{4.5}$$

where

$\tau = $ *Engineering Shear Stress* (Pa)

$T = $ *Torque* (N-m)

$\rho = $ *Outer Radius* (m)

$J = $ *Second Polar Moment of Inertia* (m^4)

The second polar moment of inertia is calculated as:

$$J = \frac{\pi}{32}(D_O^4 - D_I^4) \tag{4.6}$$

where

$D_O^4 = $ *Outer Tube Diameter* (m)

$D_I^4 = $ *Inner Tube Diameter* (m)

Time synchronization was required between the MTS loadframe and Aramis DIC system for Nextel$^{\text{TM}}$ 720/AS involute tube tests incorporating DIC, as in uniaxial tests. Time synchronization was required for Aramis to accurately record applied load data from the MTS loadframe for use with displacement and strains data collected by Aramis. Since the Aramis system only had two analog-to-digital recording channels, the MTS loadframe digital-to-analog outputs were programmed to output axial load and torsion torque to the MTS loadframe and Aramis system triggerbox for recording. Coaxial cables were used for this connection. Synchronization was achieved via a 5V TTL signal connected via coaxial cable from MTS loadframe to the Aramis trigger box. The 5V TTL trigger signal then was started at the test start via the MTS Station Manager software and triggered every second

for the test duration. The Aramis system subsequently was set to receive the 5V TTL signal and record an image set.

The torsion-to-failure test was carried out in torque control with loading rates of 1 MPa/sec to initiate fast fracture and ensure an adequate number of DIC image sets, or stages, while not overloading the processing power of the DIC system. The 1 MPa/sec loading with a target of 50 MPa yielded a 46.01 second test. From uniaxial testing, it was expected that 1 MPa/sec loading would yield 20-30 Aramis stages due to the system lag from the Aramis systems maximum of one (1) stage per second stage capturing ability. Data was acquired at 102.40 Hz. Axial force, torsion torque, time, and all 11 strain gage data was recorded. Strain gage data was recorded in Volts and transformed live into mm/mm. Additionally, axial force command, axial force absolute error, torsion torque command, torsion torque absolute error, and torsion angle were recorded for possible post-test error analysis. This procedure can be seen in Appendix A, Figure 6.7.

The biaxial (tension-torsion) proportional load procedure was performed after the torsion-to-failure test and was designed to initiate axial failure prior to torsion failure. The predicted axial UTS was 228 MPa based on uniaxial dogbone specimen testing and the predicted USS load of 32.6 MPa was observed from the pure torsion-to-failure test. Due to the desire to observe axial failure prior to torsion failure, a target of 228 MPa axial stress and 16.3 MPa shear stress was set. Axial load rates of 1 MPa/sec, which were desirable to give a higher probability of the Aramis system capturing crack initiation and/or crack propagation, yielded a test time of 455.83 seconds. Due to Aramis system limitations, an axial loading of 4 MPa/sec was required to obtain a reasonable test time of 85.5 seconds. Due to proportional loading, this related to a torsional loading of 0.143 MPa/sec. Data was acquired at 102.40 Hz. Axial force, torsion torque, time, and all 11 strain gage data was recorded. Strain gage data was recorded in Volts and transformed live into mm/mm. Additionally, axial force command, axial force absolute error, torsion torque command,

torsion torque absolute error, and torsion angle were recorded for possible post-test error analysis. This procedure can be seen in Appendix A, Figure 6.7.

V.   Results and Discussion

In order to design components that meet life, cost, and performance goals, aerospace structural designers must have a robust understanding of the materials options available to them and must be able to estimate when and how candidate materials will fail under load. Complex loading, such as the biaxial (tension-torsion) of the present study, make such an estimate all the more challenging. Overestimation of failure onset can result in unexpected component or system failure and could potentially lead to loss of life. Underestimation of failure onset results in excessive factors of safety, unnecessarily heavy components, and possibly a failure to achieve mission-specific goals. Failure criteria have been developed to guide engineers in the design process and to ensure safety and performance.

For typical aerospace materials such as aluminum, steel, and titanium, the design guidelines, failure criteria, and appropriate safety factors needed to meet program and system life cycle costs are relatively well understood. The knowledge base for aerospace alloys has been developed over many decades through an extensive use of metals in diverse aerospace applications. Metals are typically characterized with an initial elastic response followed by yield and a gradual transition toward plastic behavior. Designers typically assume isotropic behavior and these assumptions generally hold true.

Several failure criterion were developed in large part for metals undergoing multiaxial loading. Arguably the two most commonly-used criteria are the Tresca failure criterion and the von Mises failure criterion. The Tresca failure criterion, also known as the maximum shear stress criterion, assumes that failure of a material in multiaxial loading occurs when the maximum shear stress that develops exceeds a limit value. This limit value is the same as the shear stress that is developed under purely uniaxial tensile loading at the point of tensile failure. The von Mises failure criterion takes a similar approach, but evaluates maximum strain energy, rather than max shear stress. von Mises predicts

67

failure when the maximum multiaxial strain energy exceeds the maximum strain energy at onset of uniaxial failure. Tresca is generally considered to be more conservative than von Mises. Both these criteria provide useful estimates of the failure of typical isotropic, ductile, monolithic aerospace alloys, but are less useful in evaluating anisotropic, laminate composites, especially brittle CMCs.

Other failure criteria have been developed that better match the behavior of laminate composites such as those in the present study. Since in most ceramics and CMCs, failure occurs before yield stress is reached, Tresca and von Mises do not really apply. Tsai-Hill and Tsai-Wu criteria, while not specifically designed for oxide-oxide CMCs, are more applicable to laminate composite materials, and can be used to predict the onset of laminate failure in a composite material that is undergoing a complex loading state. In order to better predict the behavior of the CMC material and layup used in the present study, it was considered useful to evaluate the test data in the context of these more applicable failure criteria[15].

While the materials and test conditions in the present study were not an ideal match for the Tsai-Hill or Tsai-Wu failure criteria, it was felt that Tsai-Hill and Tsai-Wu were better suited than were Tresca and von Mises. Both, Tsai-Hill and Tsai-Wu were used to estimate the failure envelope for the oxide-oxide CMC involute tubes. The equations for Tsai-Hill theory are listed in Equation (5.1) below.

$$A\sigma_1^2 + B\sigma_2^2 + C\sigma_1\sigma_2 + D\tau_6^2 = 1 \tag{5.1}$$

In a biaxial state with axial tension and in-plane shear stress, $\sigma_2 = 0$ and thus the Tsai-Hill criterion reduces to $A\sigma_1^2 + D\tau_6^2 = 1$. With $A = \frac{1}{F_1^2}$ and $D = \frac{1}{F_6^2}$, Equation (5.1) reduces to Equation (5.2).

$$\frac{\sigma_1^2}{F_1^2} + \frac{\tau_6^2}{F_6^2} = 1 \tag{5.2}$$

In the case of these tests, F_1^2 represents F_{1t} or UTS because $\sigma_1 > 0$ and F_6^2 represents USS.

To obtain the values for UTS, dogbone specimens having a 0° fiber orientation were tested. To obtain the values for USS, straightsided specimens with a 90° fiber orientation were tested. A plot of the von Mises and Tresca along with the Tsai-Hill failure criterion is shown in Figure 5.1.
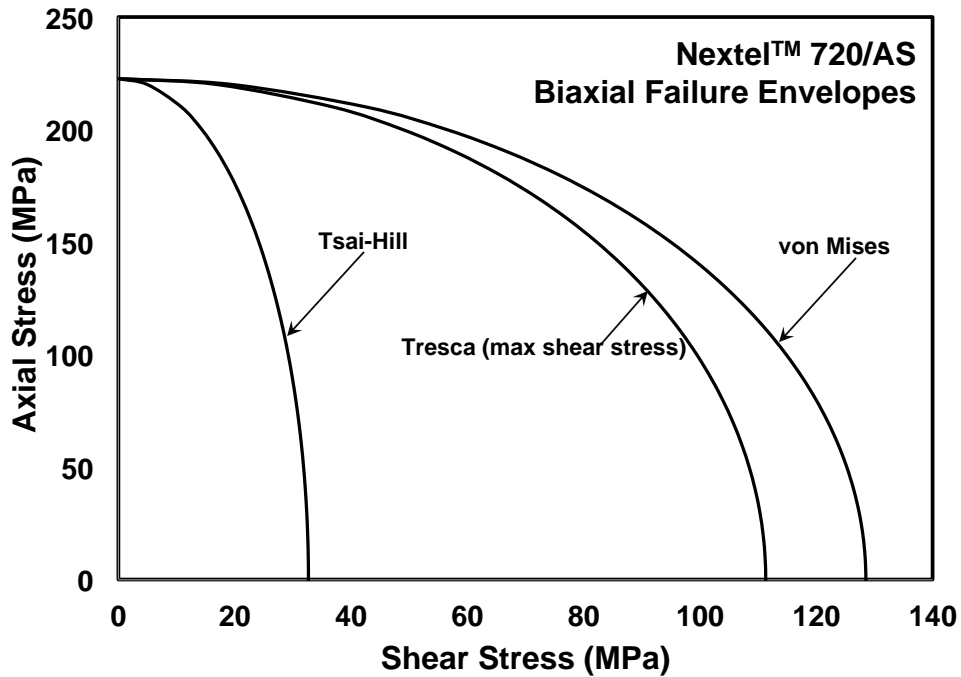

Figure 5.1: Biaxial (tension-torsion) failure envelope comparison

The results of tests conducted on the dogbone-shaped specimens are summarized in Table 5.1. Due to the limited number of tests, the results represent a qualitative assessment more than an explicit determination of properties. These tests, ultimately, were utilized to assist with prediction of biaxial (tension-torsion) failure loads.

Specimen #	Test Type	Environment	UTS (MPa)	Strain (%)	Notes
12-110	Monotonic Tension	Air - Room Temperature	211.95	0.422	
12-112	Tension-Tension	Air - Room Temperature	230.88	0.311	DIC Test
12-109	Tension-Tension	Air - 1100°C	238.56	0.268	
12-111	Tension-Tension	Air - 1100°C	224.58	0.321	
12-113	Monotonic Tension	Air - 1100°C	222.62	0.348	

Table 5.1: Summary of dogbone (0°) specimen tests

5.1 Dogbone Specimens

5.1.1 Monotonic Loading Tests

A monotonic loading test was run in tension both at room temperature and 1100°C in laboratory air. The results from these single tests are presented in Figure 5.2. While these represent single data points, it should be noted that the test run at elevated temperature displayed a higher UTS and lower strain to failure than the test at room temperature. Figure 5.3 shows a "fiber-pullout-like" behavior with definite fiber breakage, and a tortuous fracture surface. These indicators, especially the non-planar fracture surface, indicate the presence of satisfactory crack deflection mechanisms. As discussed previously in the background, the tortuous surface indicates that the path length of each crack has been lengthened which indicates that more work, or load, is required for the cracks to propagate through the specimen. Additional fracture surface images of specimen 12-113 can be seen in Figure 6.19 located in Appendix A. Of significant note is the similarities between both specimen 12-113 and the failure of the oxide-oxide CMC involute tube specimen 12-064 seen in Figure 5.34 which was biaxially loaded to failure in combined tension-torsion and discussed later.
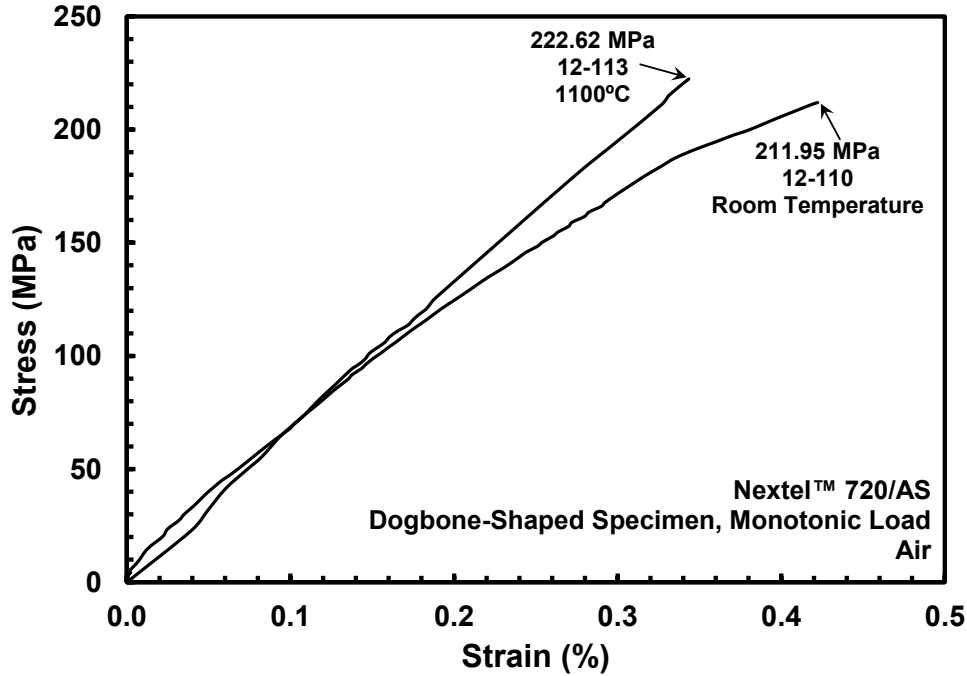
Figure 5.2: Stress vs. Strain curves obtained in monotonic tension tests of Nextel™ 720/AS dogbone-shaped specimens

The UTS of the dogbone monotonic tension test provided the first estimation point on the failure curve in Figure 5.4.

5.1.2 *Sequentially Loaded Tension Tests*

Sequentially Loaded Tension tests were repeated in an effort to obtain data for computational modeling with DIC. Results are presented in Figure 5.5. It should be noted that the UTS average of the two elevated temperature tests exceed the UTS of the room temperature test as was also observed in the monotonic tension tests. Additionally, failure strains at higher UTSs yielded lower failure strains.

In addition to failure stresses used for biaxial (tension-torsion) failure predictions, Figure 5.6 and Figure 5.7 present an interesting view of the build up to biaxial (tension-torsion) testing. The uniaxial studies served to verify that useful displacement and strain

Figure 5.3: Fracture surface of Nextel^{TM} 720/AS dogbone specimen 12-113 tested in monotonic tension to failure at 1100°C in laboratory air, top, right side

data could be obtained with the use of DIC. Figure 5.6 presents the displacements of Nextel^{TM} 720/AS dogbone-shaped specimen 12-112. The displacement measured in the specimen resulted from the corresponding bottom-to-top movement of the hydraulic actuator during specimen loading. The specimen is being held stationary at the top. The images presented to the left of the full-field displacements (moving from far right to left), are the individual Aramis DIC cameras' field of regard. In these two images, the location of the extensometer rods can be seen. This illustrates the limitation that extensometers only provide strain data at one finite point. Unlike extensometers, DIC's full field displacement and strain measurement capability provides a higher probability of capturing failure displacements and strains. Additionally, it can be seen that the displacement is not symmetric in Figure 5.6. This asymmetry could be due to specimen misalignment. Seeing

72

Figure 5.3: Fracture surface of Nextel™ 720/AS dogbone specimen 12-113 tested in monotonic tension to failure at 1100°C in laboratory air, top, right side

data could be obtained with the use of DIC. Figure 5.6 presents the displacements of Nextel™ 720/AS dogbone-shaped specimen 12-112. The displacement measured in the specimen resulted from the corresponding bottom-to-top movement of the hydraulic actuator during specimen loading. The specimen is being held stationary at the top. The images presented to the left of the full-field displacements (moving from far right to left), are the individual Aramis DIC cameras' field of regard. In these two images, the location of the extensometer rods can be seen. This illustrates the limitation that extensometers only provide strain data at one finite point. Unlike extensometers, DIC's full field displacement and strain measurement capability provides a higher probability of capturing failure displacements and strains. Additionally, it can be seen that the displacement is not symmetric in Figure 5.6. This asymmetry could be due to specimen misalignment. Seeing

72

Figure 5.4: Biaxial (tension-torsion) failure envelope with dogbone UTS point

this alignment issue is another advantage of DIC over a single point strain measurement such as an extensometer or strain gage.

Figure 5.7 displays the specimen just after failure. When compared with failure displacements seen in Figure 5.6, it appears that the DIC system correlates reasonably well to failure initiation sites. The agreement between DIC stage points used as a virtual extensometer and the actual extensometer mounted seen in Figure 5.5 provided the necessary confidence to move forward with DIC use as a measurement technique during biaxial (tension-torsion) testing.

Micrographs of the remaining dogbone specimens can be seen in Figure 6.17 through Figure 6.21 in Appendix A.
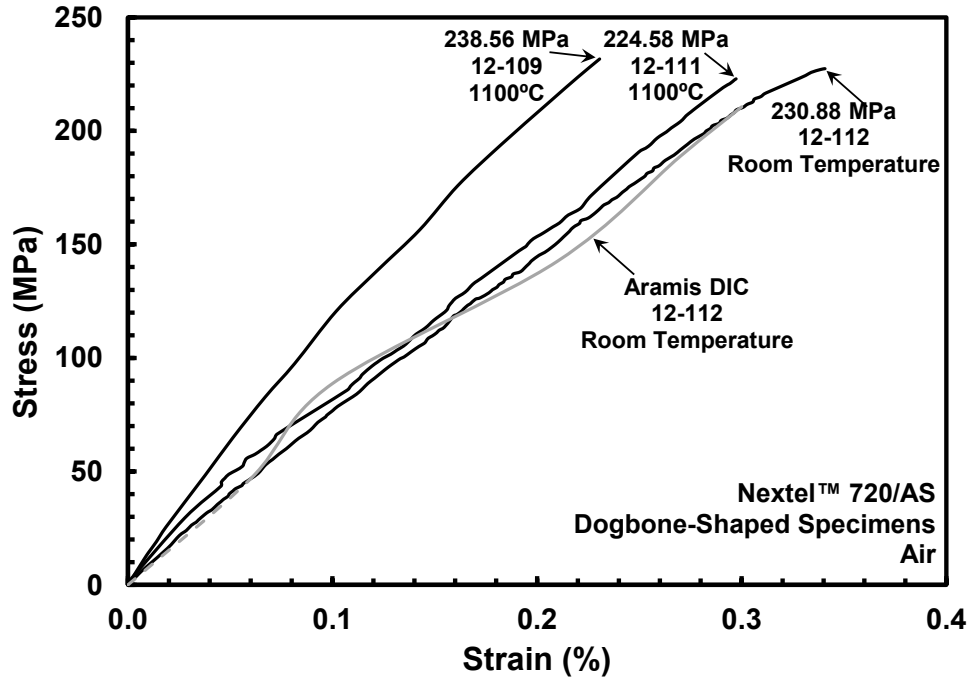
Figure 5.5: Stress vs. Strain curves without hysteresis removed obtained in sequentially loaded tension tests of Nextel™ 720/AS dogbone-shaped specimens
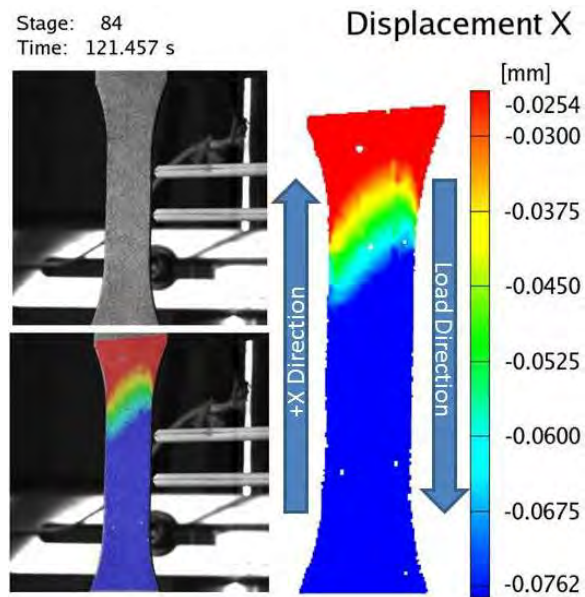
Figure 5.6: Nextel™ 720/AS dogbone specimen just before failure
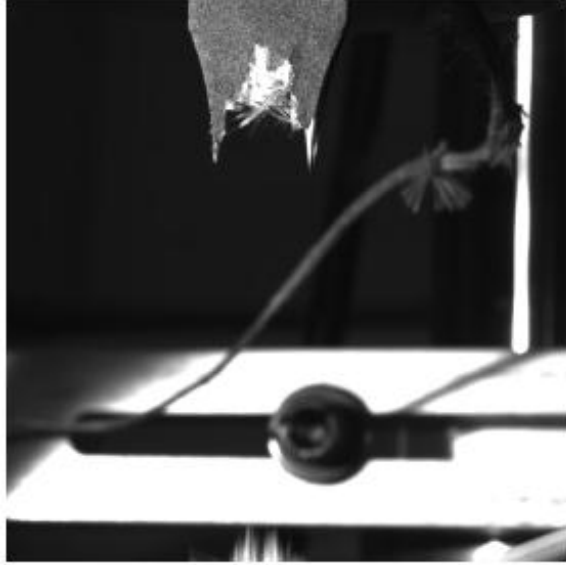
Figure 5.7: Nextel^{TM} 720/AS dogbone specimen just after failure

5.2 Straightsided Specimens

Similar to the dogbone-shaped specimens, the straightsided specimens cut in the 90°, orientation tests are summarized in Table 5.2. Due to the limited number of tests, the results represent a qualitative assessment more than an explicit determination of properties. These tests, ultimately, were utilized to assist with prediction of biaxial (tension-torsion) failure loads.

Specimen #	Test Type	Environment	UTS (MPa)	Strain (%)	Notes
12-099	Monotonic Tension	Air - 1100°C	46.36	0.051	
12-100	Monotonic Tension	Air - 1100°C	45.88	N/A*	*Extensometer Slip
12-098	Monotonic Tension	Air	49.11	0.081	DIC Test
12-106	Monotonic Tension	Air	39.44	0.066	

Table 5.2: Summary of straightsided (90°) specimen tests

The results of the straightsided specimens were complimentary to the results seen with fiber-dominated properties in that higher temperatures yielded, on average, higher UTS and lower failure strains than at room temperature. UTS was lower, as expected, than dogbone-shaped specimens due to the matrix-dominated properties. Micrographs of the straightsided specimens can be seen in Figure 6.22 through Figure 6.25 in Appendix A. These tests yielded estimates to the shear stress values seen in Figure 5.25.

The higher values of USS are the values obtained in the monotonic straightsided tests. A comparison to the DNS specimens was desired. DNS specimens measure a pure ILSS matrix-dominated value. While the straightsided specimens did measure a matrix-dominated shear strength, this was not a pure shear strength value. As a result a stress
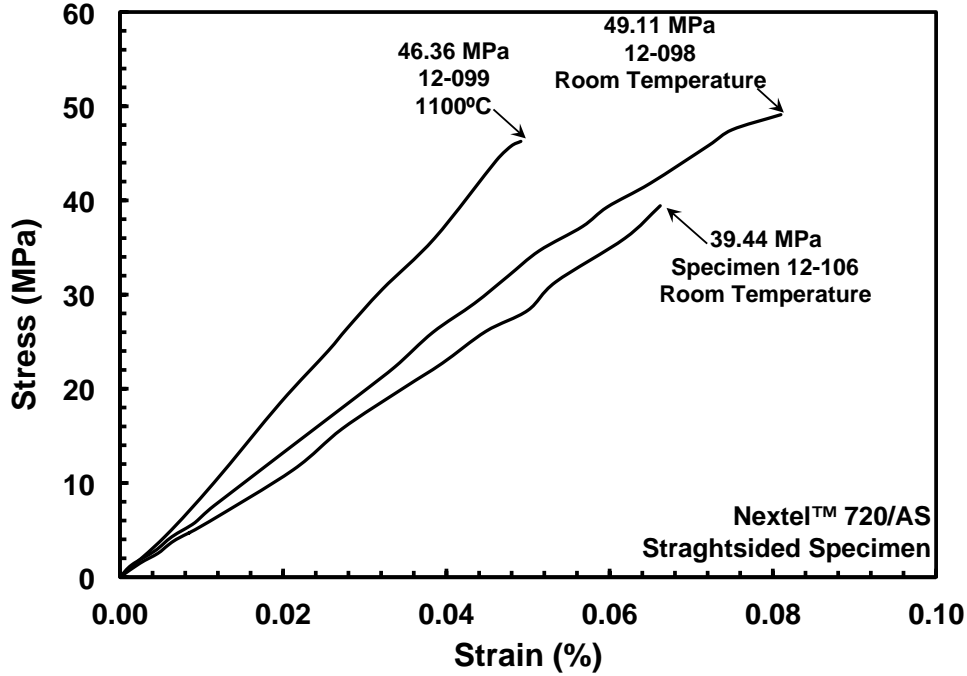
Figure 5.8: Stress vs. Strain curves obtained in tension test of Nextel$^{\text{TM}}$ 720/AS straightsided specimens 12-098, 12-099, and 12-106

transformation had to be made. With the assumption that the angle between involute plies was 7°, the stress tensor rotations are as follows:

$$\sigma'_x = \sigma_x cos^2\theta + \sigma_y sin^2\theta - 2\tau_{xy} sin\theta\ cos\theta \qquad (5.3)$$

$$\tau'_{xy} = (\sigma_x - \sigma_y)sin\theta\ cos\theta + \tau_{xy}(cos^2\theta - sin^2\theta) \qquad (5.4)$$

Equation (5.4) reduces to Equation (5.5) with the x-direction being the uniaxial load direction and the y being the through thickness direction as follows:

$$\tau'_{xy} = \sigma_x sin\theta\ cos\theta \qquad (5.5)$$

With the angle here being from the horizontal, 90° - 7° or nominally 83°, Equation (5.5) equates to:
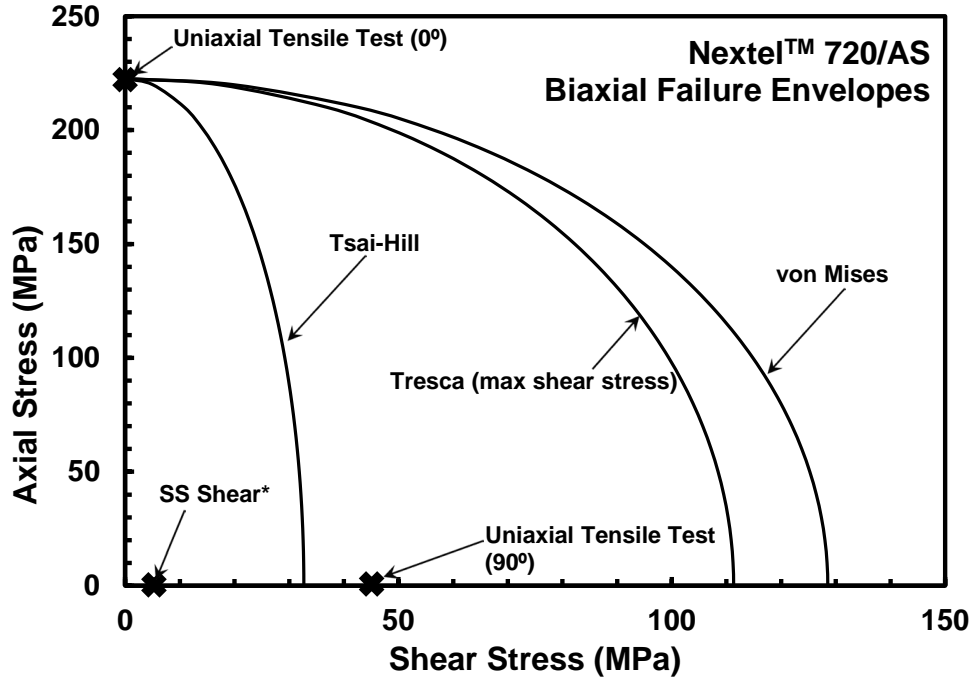
Figure 5.9: Biaxial (tension-torsion) failure envelope with monotonic UTS and USS

$$\tau'_{xy} = 0.12\sigma_x \tag{5.6}$$

Thus, the comparative value of 5.31 MPa of shear stress can be compared to ILSS values in the DNS specimens. The pure shear and monotonic ultimate strength values of the straightsided specimens can be seen in Figure 5.25.

5.3   Double-Notch Shear (DNS) Specimens

The DNS specimen tests are summarized in Table 5.3. Due to the limited number of tests, the results represent a qualitative assessment.

A total of three interlaminar shear monotonic compression tests were carried out at 1100°C in laboratory air. The results from these tests are presented in Table 5.3. ILSS results at 1100°C represent values previously unpublished by COI Ceramics [3]. These

Specimen #	Test Type	Environment	ILSS (MPa)	Failure Strain (%)	Creep Stress (MPa)
1	Monotonic Compression	Air - 1100°C	7.43	0.102	-
2	Monotonic Compression	Air - 1100°C	7.60	0.238	-
3	Monotonic Compression	Air - 1100°C	7.60	0.078	-
5	Compressive Creep	Air - 1100°C	-	0.317	6
6	Compressive Creep	Air - 1100°C	-	0.384	5
7	Compressive Creep	Air - 1100°C	-	0.471	4
8	Compressive Creep	Air - 1100°C	-	0.072	2
9	Compressive Creep	Steam - 1100°C	-	0.345	6

Table 5.3: Summary of DNS Specimen Tests

tests served to determine the appropriate 80% ILSS levels at which interlaminar shear creep test could be performed. The selection of 6 MPa for initial high temperature interlaminar shear creep tests represented a stress level of 79.5% observed ILSS values. The absolute stress versus absolute strain of these three tests are plotted in Figure 5.10.

The results of the monotonic compression yielded the final estimate for potential failure strengths of the biaxial oxide-oxide involute tube specimens. This estimate is plotted on the biaxial failure envelope estimation. Of note is the relative closeness of value to that of the shear stress transformed values of the straightsided specimens. DNS specimens were tested at elevated temperature and the straightsided transformed shear strength value was obtained at room temperature, thus, these values should not be used for quantitative comparison. These points can all be seen in Figure 5.11.

Following the ILSS testing, interlaminar shear creep tests were performed at 1100°C in laboratory air. The results of these tests are seen in Figure 5.13. Runout was set at 100
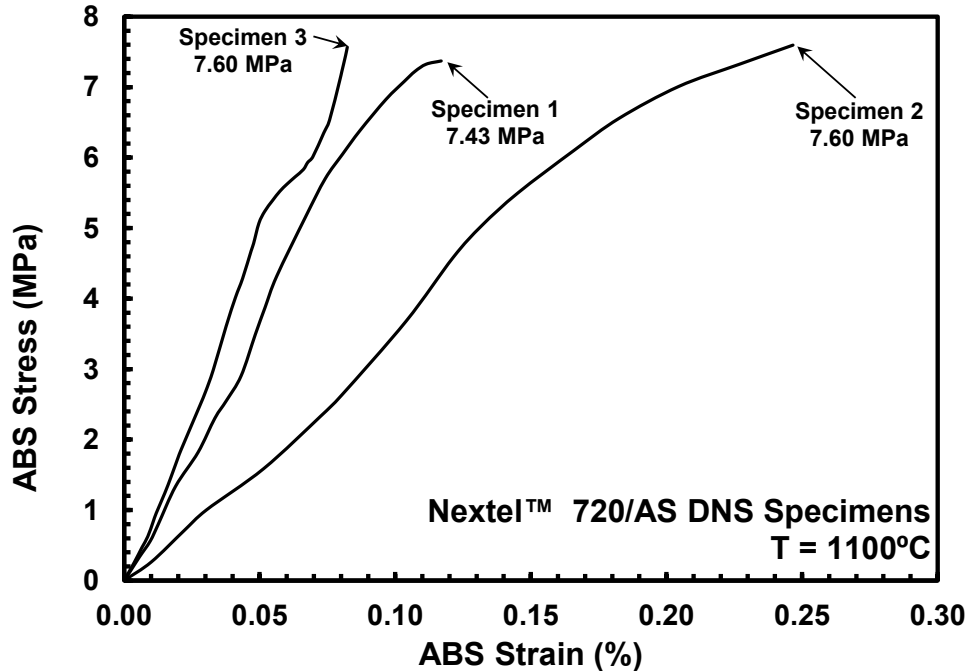
Figure 5.10: ABS Shear Stress vs. ABS Strain curves obtained in compression test of Nextel^{TM} 720/AS DNS specimens 1, 2, and 3 at 1100°C

hours, but was never obtained. After failing to achieve runout at 4 MPa, an estimation spreadsheet was created and a best fit curve was placed on the first three data points of 6, 5, and 4 MPa. A runout time of 360,000 seconds, or 100 hours, was placed into the equation, displayed in Figure 5.12, and solved for stress in MPa. A stress of 2.15 MPa was determined and a 2 MPa test was accomplished. Unfortunately, while creep levels were extremely low, the material still failed to achieve runout. Elevated temperatures in steam for comparison to test results in air were then carried out. The first test of 6 MPa in steam at 1100°C was carried out after a steam temperature calibration was carried out. The results of the 6 MPa test in both air and steam are shown in Figure 5.14.

After specimen failure, micrographs of the fracture surfaces were taken. Micrographs of specimen 1 are shown in Figure 5.15. Figure 5.14 shows the comparison of 6 MPa tests
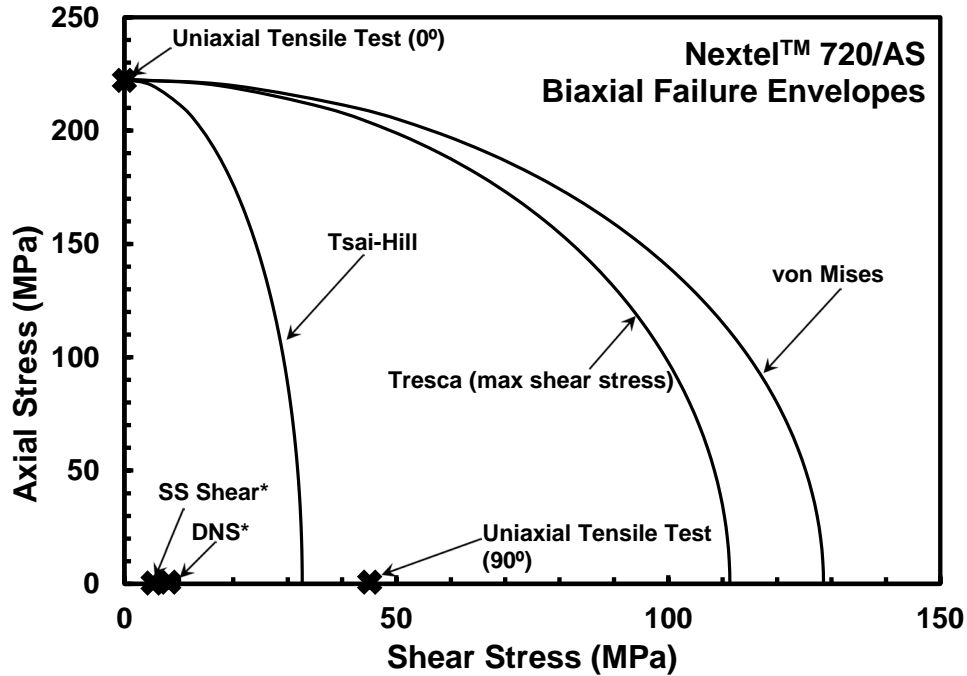
Figure 5.11: Biaxial (tension-torsion) failure envelope with monotonic UTS, USS, and ILSS values

in both air and steam. Specimen 1, tested for ILSS exhibited fast fracture with a very clean fracture surface and very little fiber breakage. Specimen 6, which was run in an interlaminar creep test at 6 MPa, exhibited similar fracture surface properties as Specimen 1. However, in steam, specimen 9, tested in interlaminar creep at 6 MPa in steam demonstrated rougher fracture surfaces with even less fiber breakage. Additionally, despite no modification of the failure detector which previously had worked flawlessly, fracture surfaces began to exhibit breakage at the machined notches orthogonal to the shear surfaces. The remainder of the fracture surfaces can be seen in Figure 6.26 through Figure 6.35 in Appendix A.

Specimens 10, 11, and 12 could have failed due to buckling from DNS specimen notches failing to meet the -0 ASTM specified t/2 cut depth per Figure 3.11 and Table 3.1. Images of this shortfall in Specimen 12 are pictured in Figure 5.17 and Figure 5.18 where
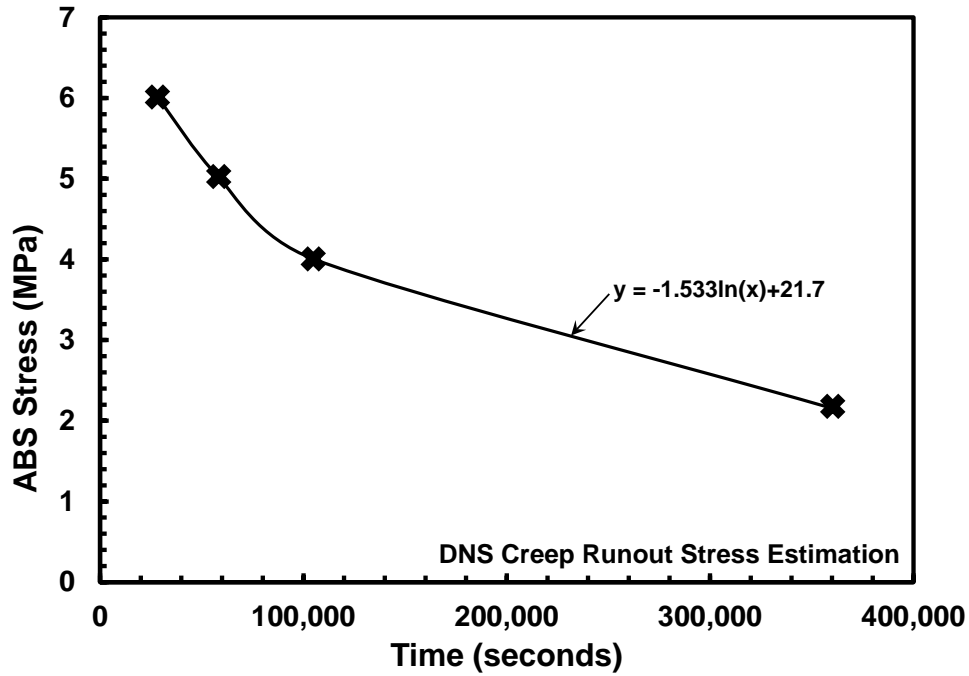
Figure 5.12: DNS creep runout stress estimation spreadsheet with curve fit to 6, 5, and 5 MPa to estimate runout at 360,000 seconds (100 hours) used for Nextel[TM] 720/AS in air at 1100°C

one side fails to meet specification and one side appears to touch centerline. Failing to meet the -0 t/2 specification would prevent ILSS failure as was intended and desired. It should be noted that failing to achieve ILSS modes of failure only occurred in steam rather than in both air and steam. Failing to achieve ILSS could be the result of many issues including specimen geometry or changes to materials due to the environment.
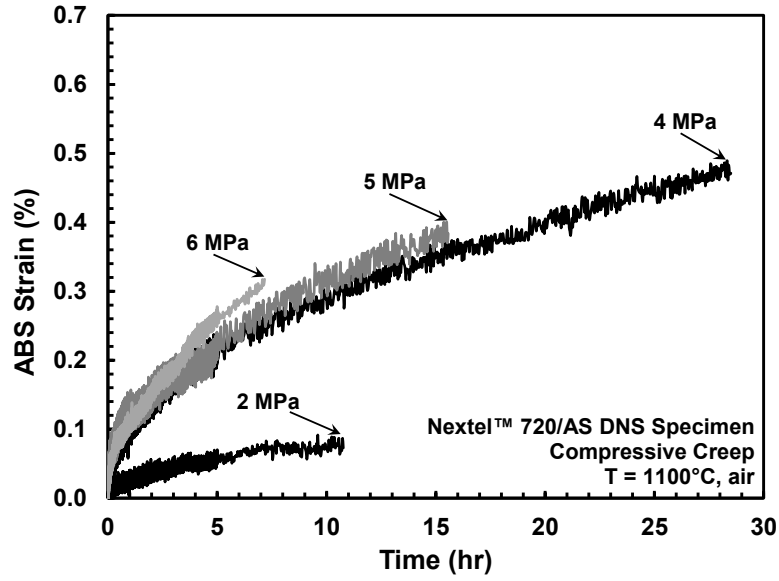
Figure 5.13: ABS Strain vs. Time curve for interlaminar shear creep tests on Nextel[TM] 720/AS in air at 1100°C
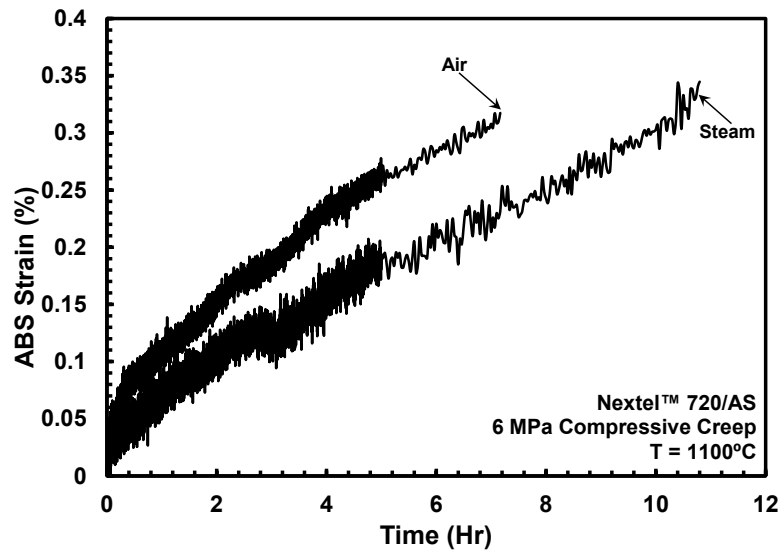
Figure 5.14: 6 MPa ABS Strain vs. Time curve comparison of interlaminar shear creep tests on Nextel[TM] 720/AS in air and steam at 1100°C
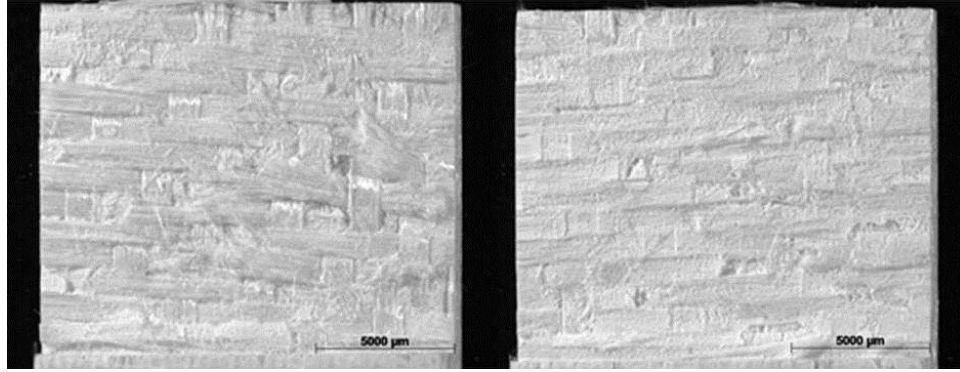
Figure 5.15: DNS Specimen 1 ILSS of Nextel^{TM} 720/AS in air at 1100°C
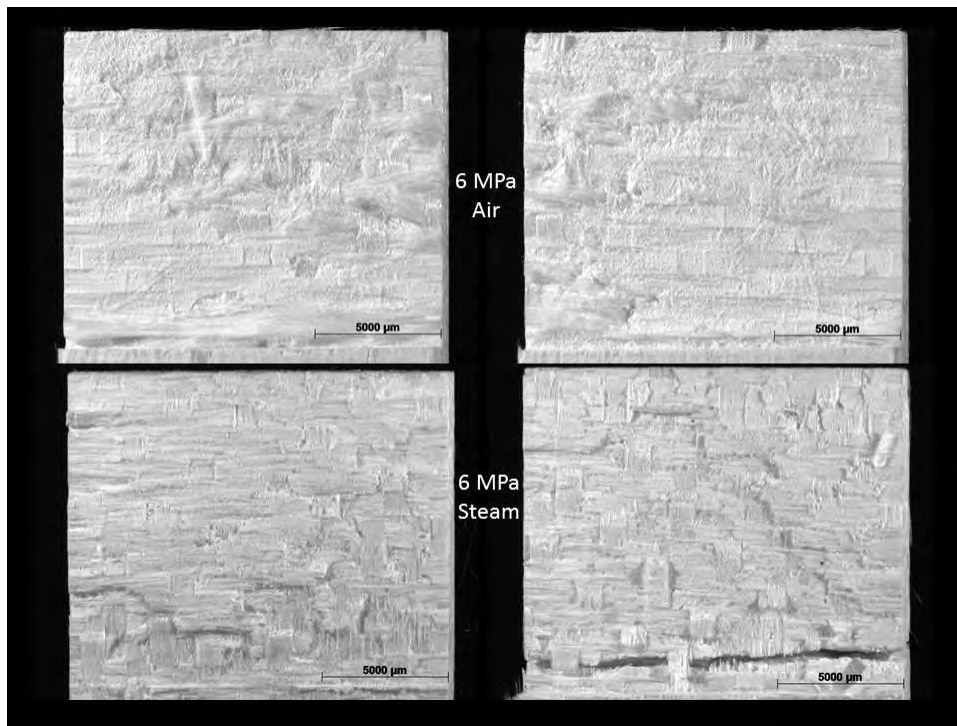
Figure 5.16: DNS Specimen 9 interlaminar creep of Nextel^{TM} 720/AS in air (top) and steam (bottom) at 1100°C
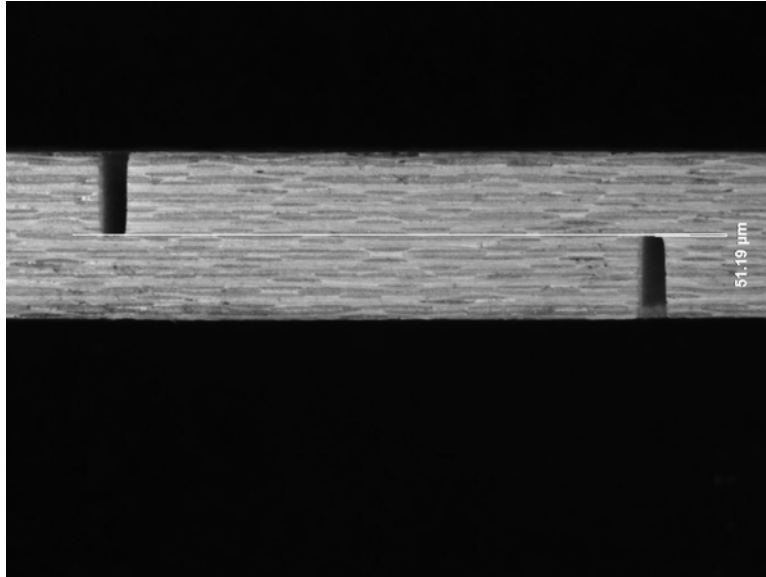
Figure 5.17: DNS specimen 12 left side notch undercut by 51.19μm - specimen failed unsatisfactorily under 4 MPa creep load at 1100°C in steam
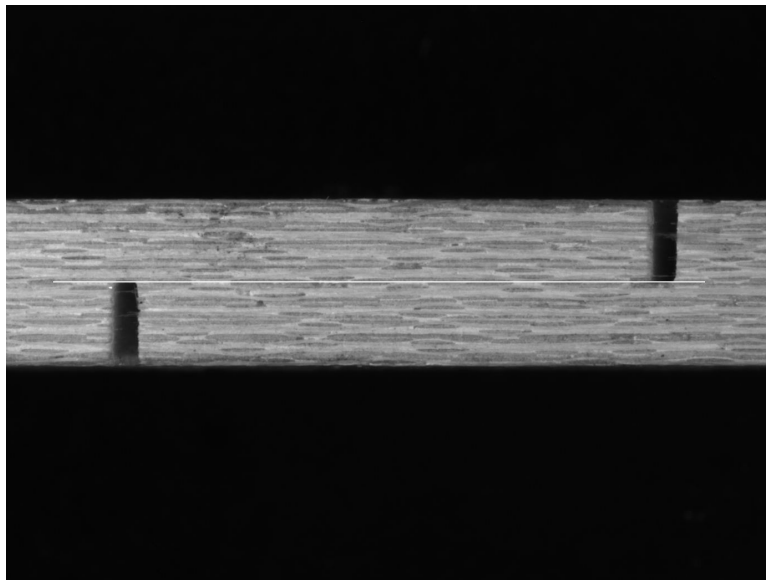
Figure 5.18: DNS specimen 12 right side cut to specification - specimen failed unsatisfactorily under 4 MPa creep load at 1100°C in steam

5.4   Thin-Wall Tube Specimens

All tests were accomplished at room temperature in laboratory air.

Specimen #	Test Type	UTS	USS	γ_{xy} Average	γ_{xy} Left	γ_{xy} Center	γ_{xy} Right	Failure Mode
		(MPa)	(MPa)	(%)	(%)	(%)	(%)	
12-063	Torsion to Failure	~0	32.68	0.31	0.24	0.41	0.29	Torsion
12-064	Biaxial to Failure	171.74	11.83	0.32	0.28	0.37	0.31	Torsion

Table 5.4: Summary of oxide-oxide CMC involute tube specimen tests

Data reduction was accomplished on MTS and DIC acquired data. Shear strain data was reduced from the three rectangular strain rosettes. The three rosettes each individually measured ϵ_A, ϵ_B, and ϵ_C. The circumferential gage, ϵ_A was the 0° reading, ϵ_B was the 45° gage reading, and ϵ_C is the axial or lengthwise gage reading at 90°. All three gages had units of $\mu\epsilon$. These direct readings could be transformed into shear strain, γ_{xy} via the following equations[14]:

$$\epsilon_A = \epsilon_{xx} \qquad \epsilon_B = \frac{1}{2}(\epsilon_{xx} + \epsilon_{yy} + \gamma_{xy}) \qquad \epsilon_C = \epsilon_{yy} \qquad \text{where} \qquad \gamma_{xy} = 2\epsilon_B - \epsilon_A - \epsilon_C \quad (5.7)$$

Once calculated, shear strain, could be plotted against the stress of interest. Figure 5.19 is a plot of the applied shear stress during the pure torsion test of CMC tube Specimen 12-063. Several factors influence the output of the stress/strain curves when using strain gages. Due to human error, strain gages bond quality can vary from installation to installation. The more iterations of installation and data collection that are carried out, the more an individual's techniques and processes for successful installation can be refined and increase the probability of successful installation. In other words, strain

gage installation is a variable uncontrollable by machine and thus will have some variability installation to installation. Differences in strain gage locations will also result in different strains measured. In the case of specimen 12-063, the center rosette was the closest gage to the failure sites as seen in the center image of Figure 5.20. This explained the higher shear strains seen in Figure 5.19. Further, the left and right rectangular strain gage rosettes (far left and far right, respectively of Figure 5.20) appeared to qualitatively show the next highest and lowest, respectively, strains based on the distance from the specimen failure site. Figure 5.19 shows, just like the dogbone specimen in Figure 5.3, "fiber-pullout-like" behavior with definite fiber breakage, and a tortuous fracture surface can be seen indicating satisfactory crack deflection mechanisms are present.
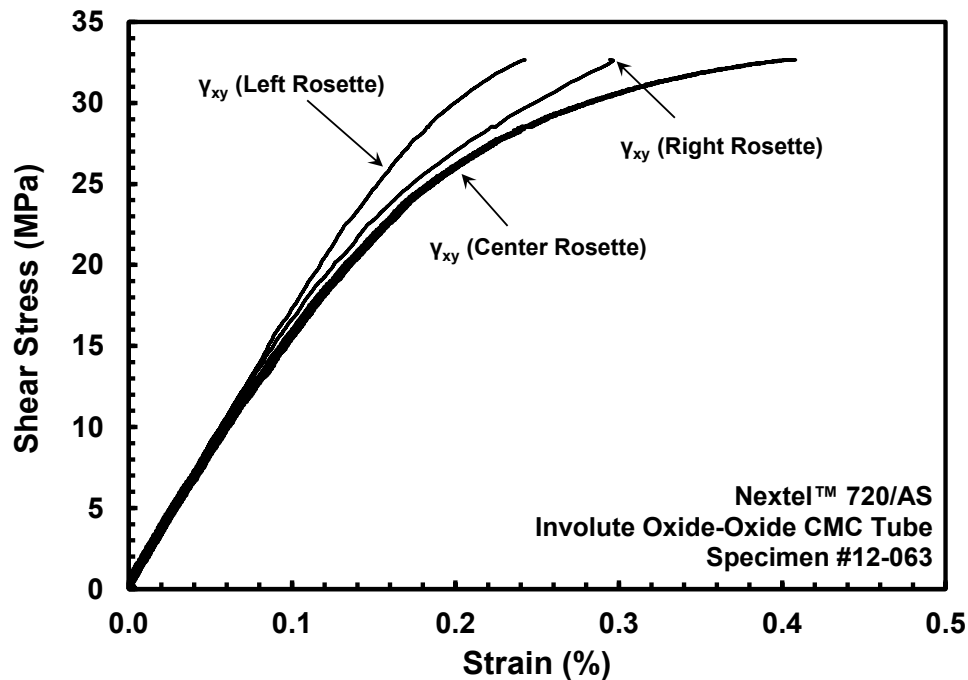
Figure 5.19: Shear stress vs. shear strain for Nextel^{TM} 720/AS oxide-oxide involute tube specimen 12-063 in pure torsion
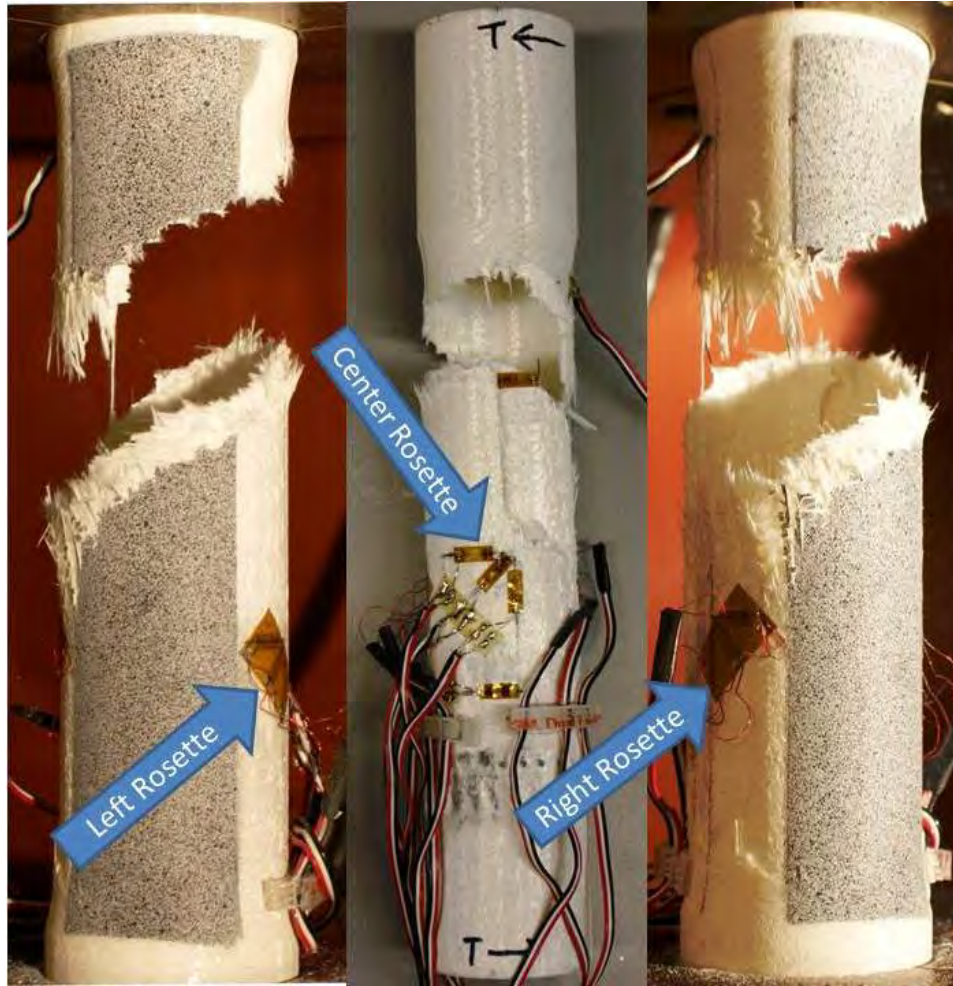
Figure 5.20: Qualitative crack distance to left, center, and right rosettes (from left to right) explaining differences in measured shear strains in Nextel^{TM} 720/AS oxide-oxide involute tube specimen 12-063 in pure torsion

The Aramis DIC data can be presented in an infinite number of ways dependent on items under study. Ultimately, DIC measures localized displacements or strains of the article under test. The primary objective of this research was detection of crack initiation and crack propagation within the involute tube to understand failure mechanisms beyond UTS, USS, and failure strains.

Figure 5.21 shows the crack initiation and crack propagation of specimen 12-063. Of significant interest is the location of this damage initiation site. Figure 5.22 shows where the specimen damage propagated through the involute tube wall thickness. While the top two images in Figure 5.21 show the failure location site near the bottom grip, Figure 5.22 shows the separation of the two parts, closer to the top grip. Upon inspection of the specimen, it appeared that the damage initiated near the bottom grip and propagated up through the thickness of the tube before the crack propagated through the thickness of the tube. This crack and crack propagation direction can be seen in the bottom of Figure 5.21.

Post failure analysis showed the possible path of the damage lengthwise through the specimen could have been through the delamination between plies of the involute layup. Figure 5.23 shows the separation of involute plies as a result of pure torsion loading. This damage along the involute layup exhibits the fiber architecture shown previously in Figure 3.12. Further "fiber-pullout-like" behavior and definite fiber breakage along the failure sites can be seen in Figure 5.24.

With the uniaxial tension test providing an estimate for the UTS and the pure torsion-to-failure test providing the expected value of USS of the involute tube, estimates of the failure loads could be made and a proportional load profile in load control could be planned and executed on the final involute tube specimen.

Following the successful test in pure torsion to failure, a biaxial (tension-torsion) test to failure was accomplished. The results of the uniaxial dogbone, straightsided, and DNS specimens in addition to the procedures developed during the single PMC tube test, alumina pure torsion test, alumina biaxial test, and oxide-oxide CMC involute tube in pure torsion test all culminated with the final biaxial (tension-torsion) test of an oxide-oxide CMC involute tube loaded proportionally in tension and torsion.
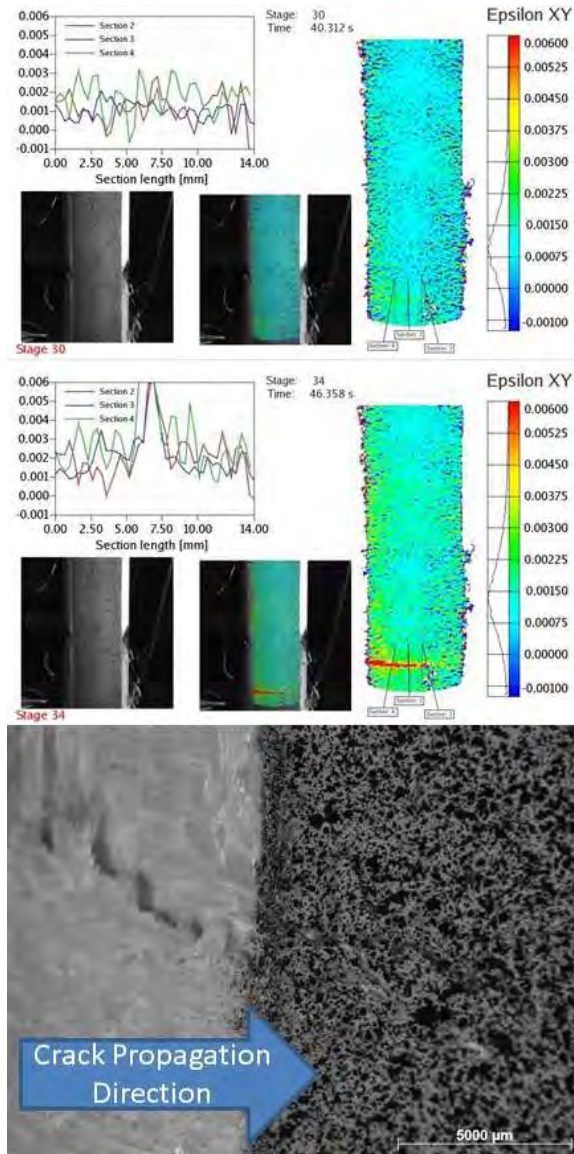
Figure 5.21: Aramis DIC showing crack propagation in Nextel^{TM} 720/AS oxide-oxide involute tube specimen 12-063 in pure torsion

Specimen 12-064 was tested biaxially in tension and torsion to investigate the influence of small torsional loads on an axially loaded specimen. Based on the desire of an axial failure mode and the estimates of UTS of 228 MPa and USS of 32.6 MPa, a 50% reduction of USS was targeted with 100% UTS. Target loading, thus, was $\tau = 7.15\%\sigma$
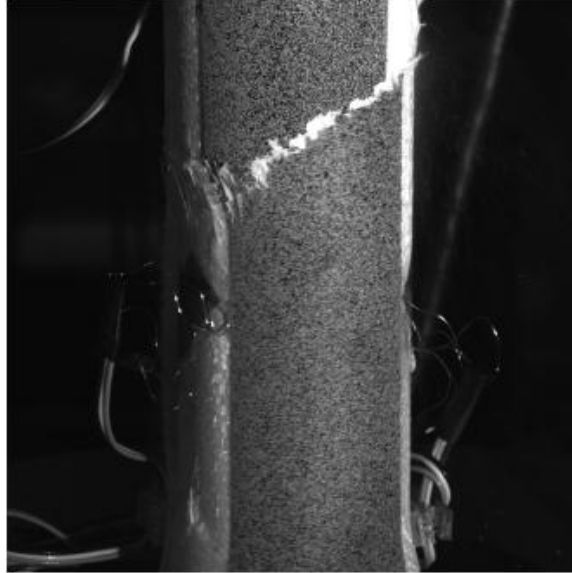
Figure 5.22: Nextel^{TM} 720/AS oxide-oxide involute tube specimen 12-063 in pure torsion
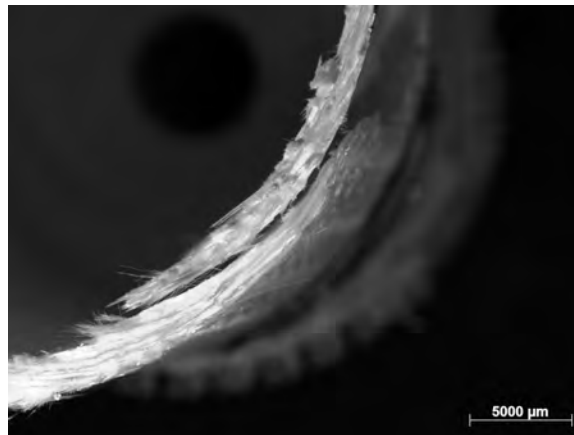
Figure 5.23: Involute Ply Failure - Nextel^{TM} 720/AS oxide-oxide involute tube specimen 12-063 in pure torsion

where τ = shear stress and σ = axial stress. Actual failure loads equated to τ = 6.89%σ and the specimen failed torsionally, not axially as intended.
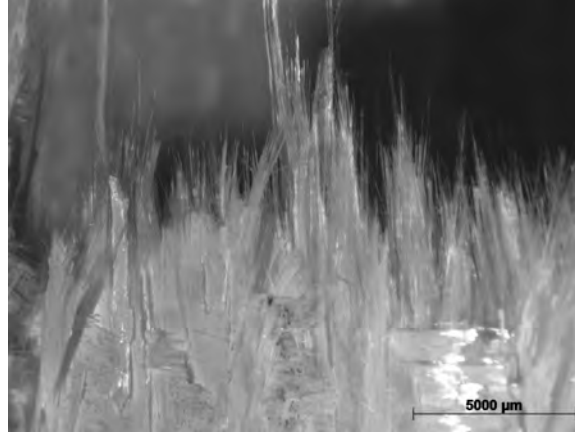
Figure 5.24: Closeup of Nextel$^{\text{TM}}$ 720/AS oxide-oxide involute tube specimen 12-063 fracture damage from pure torsion

The difference in axial versus shear stresses is illustrated in Figure 5.26 where the axial and shear stresses versus the shear strains are presented together. For uniaxial results, generally, stress versus strain curves terminate with a drop in load of the specimen indicating the ultimate load failure of the test specimen. In the case of specimen 12-064, the oxide-oxide CMC involute tube failed torsionally, but still supported an axial load before separating into two parts. Figure 5.27 plots shear stress versus shear strain independently and illustrate this drop in stress in the last data points. A lower yield point is defined when there is a maximum load point referred to as an upper yield point. Additionally, a lower value at which continued deformation, in this case specimen separation, must be defined and present. This later point is referred to as the lower yield point [23, 706-7].

While crack initiation and crack propagation were detectable in specimen 12-063 using DIC with ϵ_{xy} (γ_{xy}) processing, loading rates of specimen 12-064 precluded these events from being detected. In this case, however, displacements were displayed in the X (specimen length) and Y (specimen circumference) directions. Figure 5.28 and Figure 5.29 show the displacement gradients in the X and Y directions, respectively. Despite the
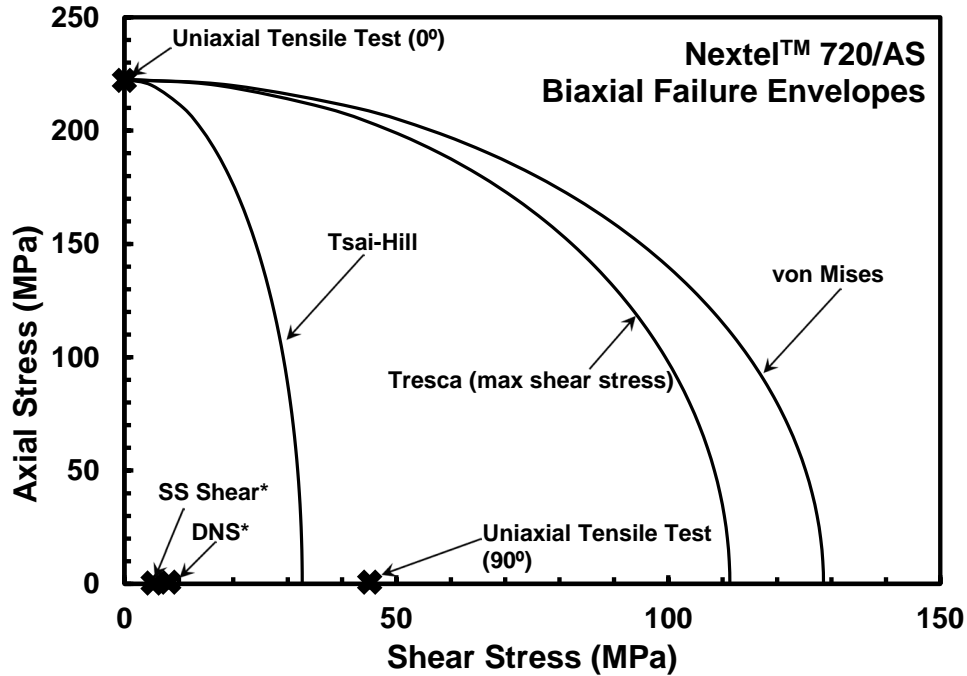
Figure 5.25: Biaxial (tension-torsion) failure envelope with monotonic UTS and USS, ILSS, and actual value of in-plane shear stress as seen in the pure torsion to failure oxide-oxide CMC involute tube test

loading rate precluding crack detection, specimen failure sites can still be narrowed down with the use of section lines to plot strain rates across a cross-section of the area of the specimen being imaged. Figure 5.30 shows specimen 12-064 after failure.

While crack initiation or propagation was not detected, one of the major reasons for the use of DIC on CMCs was exhibited. Figure 5.31 shows the strains on individual fiber tows being detected. The fiber tows unpainted can be seen on the left image while the major strains just before specimen failure can be seen in the right image. This resolution of strain or displacement data is unrivaled by any other strain or displacement measuring system available today. Further processing in Figure 5.32 is shown with the addition of a section
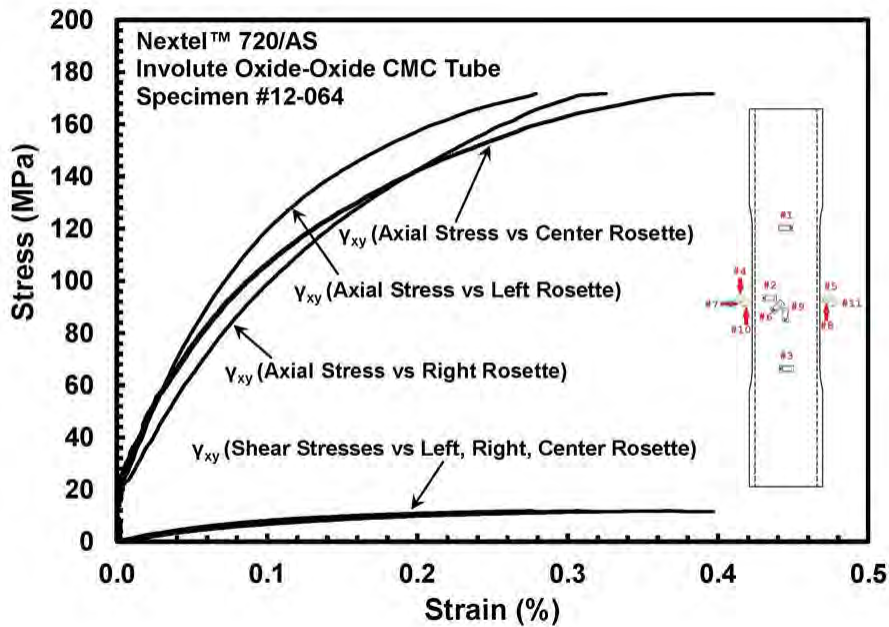
Figure 5.26: Axial and shear stresses vs. shear strain for Nextel^{TM} 720/AS oxide-oxide involute tube specimen 12-064 - biaxial loads to failure - failed in torsion

line to indicate the rise and fall of strains across the fiber tows. The rise and fall of strains displayed in the graph of the section line strain values correlates Figure 5.33 shows the approximate distances between warps in the satin weave. This distance of approximately 6.1mm can be correlated to the spikes of major strain in the section line. A spike of approximately 1.3% strain at 14mm on the section length can be seen. Additional spikes can be seen approximately every 6-7mm indicating that this section line is along a warp fiber tow. Also of interest is that the strain of these individual fiber tows is much higher (1.2-1.5+%) than the macroscopic specimen failure strains.

Micrographs of fracture surfaces can be seen in Figure 5.34 and Figure 5.35. Figure 5.34 is of interest due to the similarities in failure damage displayed between the

94
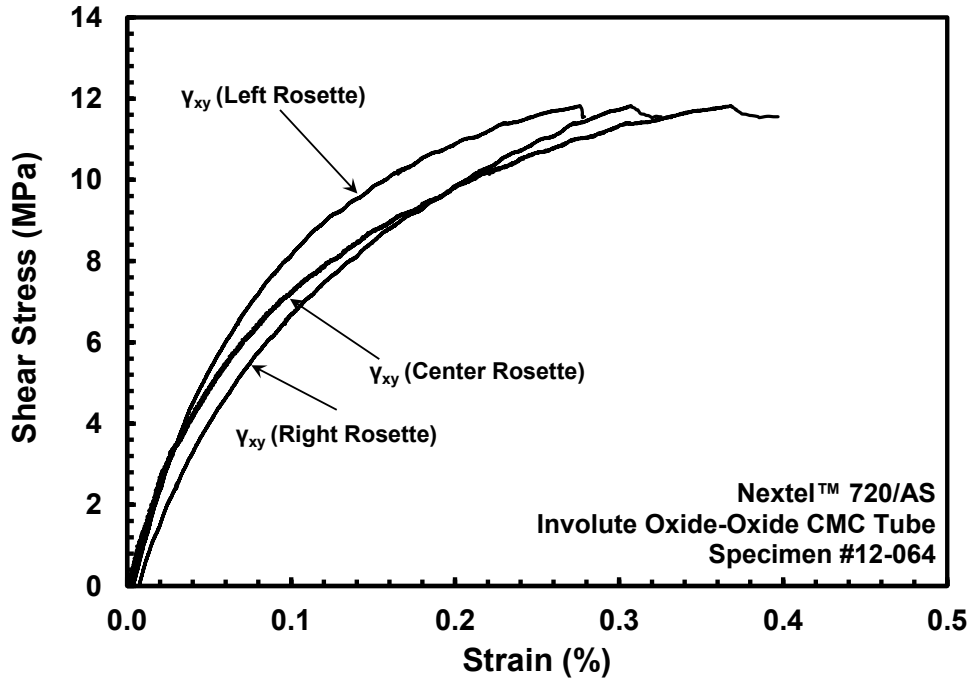
Figure 5.27: Shear stresses vs. shear strain (expanded) for Nextel[TM] 720/AS oxide-oxide involute tube specimen 12-064 - biaxial loads to failure - failed in torsion

involute tube and dogbone specimens as seen in Figure 5.3. Again, "fiber-pullout-like" behavior with definite fiber breakage, and a tortuous fracture surface can be seen indicating satisfactory crack deflection mechanisms are present.

The Tsai-Wu, or interactive tensor polynomial theory, is a failure criterion that accounts for the difference between tensile and compressive strengths in an anisotropic material, similar to the CMC in this study. Tensile strength lies in the axial or length-wise direction and compressive strength lies in the circumferential direction during biaxial (tension-torsion) testing. In the case of the involute tubes, the axial strength was shown to be much higher than the torsional strength. As such, it was appropriate to see what this failure criterion would predict. The results of the proportionally loaded biaxial (tension-torsion) test can be seen in Figure 5.36 along with the Tsai-Wu failure criterion fit curve.

Figure 5.28: Nextel^{TM} 720/AS oxide-oxide involute tube specimen 12-064 - biaxial loads to failure - failed in torsion

The Tsai-Wu curve in Figure 5.36 incorporates only one biaxial (tension-torsion) data point. More data points would be required before deriving more information to the suitability of the Tsai-Wu failure criteria to the Nextel^{TM} 720/AS oxide-oxide CMC. The Tsai-Hill and Tsai-Wu appear to provide a better failure strength estimation than von Mises or Tresca.

The Tsai-Wu failure criteria is seen in Equation (5.8).

$$f_1\sigma_1 + f_2\sigma_2 + f_{11}\sigma_1^2 + f_{22}\sigma_2^2 + f_{66}\tau_6^2 + 2f_{12}\sigma_1\sigma_2 = 1 \qquad (5.8)$$

Equation (5.8), for the biaxial (tension-torsion) loading condition, is reduced to Equation (5.9) where $f_1 = \frac{1}{F_{1t}} - \frac{1}{F_{1c}}$ and $f_{11} = \frac{1}{F_{1t}F_{1c}}$ and $f_{66} = \frac{1}{F_6^2}$

Figure 5.29: Nextel^{TM} 720/AS oxide-oxide involute tube specimen 12-064 - biaxial loads to failure - failed in torsion

$$f_1\sigma_1 + f_{11}\sigma_1^2 + f_{66}\tau_6^2 = 1 \tag{5.9}$$

From the uniaxial tests, F_{1t} was determined to be 222.62 MPa and from the pure torsion test, F_{66} was determined to be $\frac{1}{32.68^2 MPa}$ or $9.36 \times 10^{-4} \frac{1}{MPa}$. These values along with σ_1 and τ_6 of 171.74 MPa and 11.83 MPa, respectively, were placed into Equation (5.9) and a value for F_{1c} was determined to be -402.535 MPa. Because brittle structures tend to have higher compressive failure strengths, the value for F_{1c} seemed appropriate. Further, when plotted, the data fit on the curve in an reasonable manner.

Figure 5.30: Nextel^{TM} 720/AS oxide-oxide involute tube specimen 12-064 just after failure - biaxial loads to failure - failed in torsion
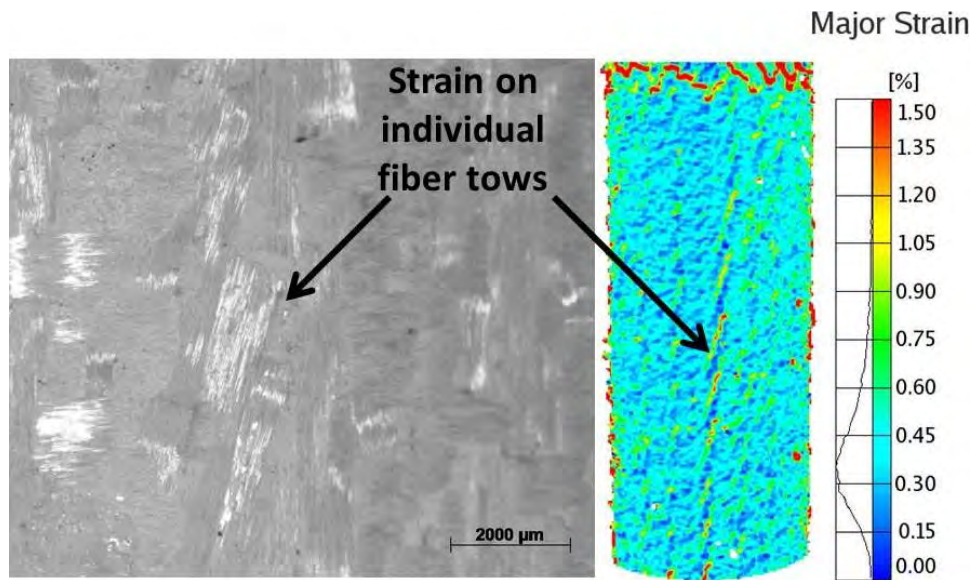
Figure 5.31: DIC measured strains of individual fiber tows on Nextel^{TM} 720/AS oxide-oxide involute tube specimen 12-064 - biaxial loads to failure - failed in torsion

Figure 5.32: DIC measured strains of individual fiber tows on Nextel™ 720/AS oxide-oxide involute tube specimen 12-064 - biaxial loads to failure - failed in torsion
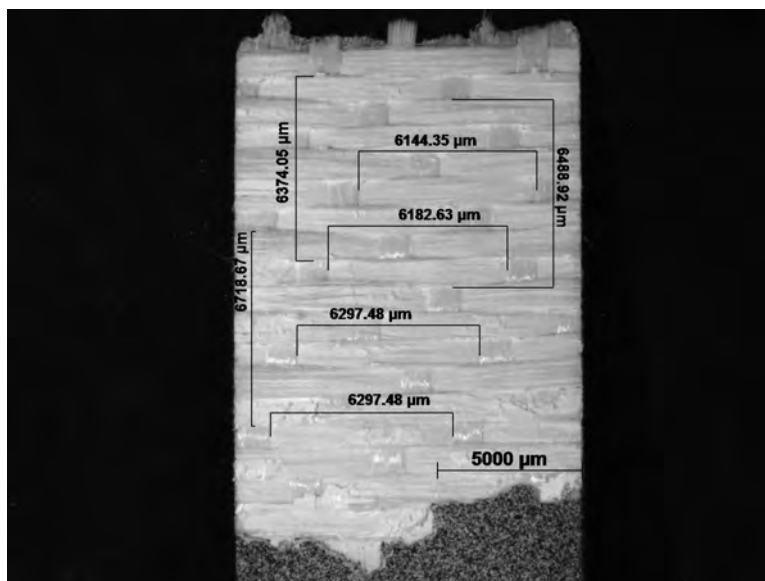
Figure 5.33: Distance between warps in 8H Nextel™ 720 satin weave used in Nextel™ 720/AS involute layup
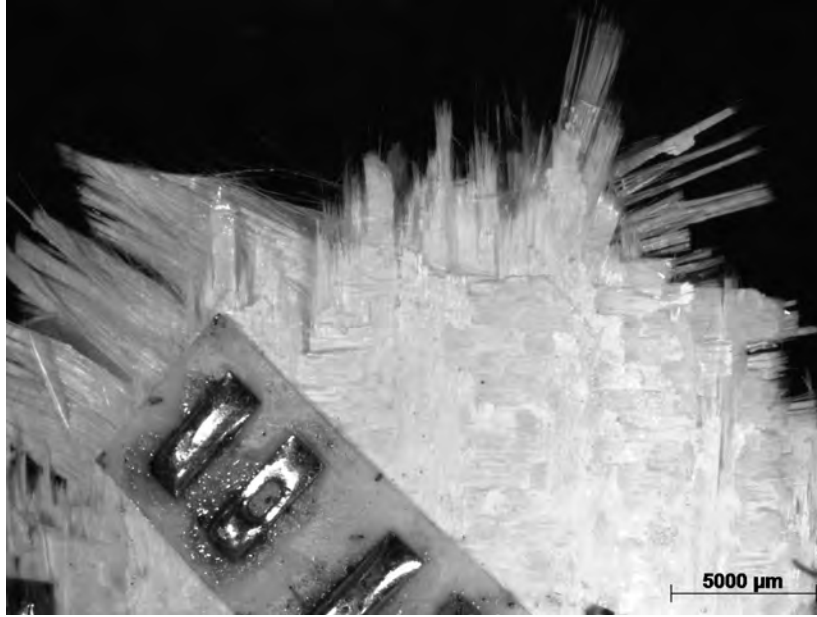
Figure 5.34: Damage of Nextel[TM] 720/AS oxide-oxide involute tube specimen 12-064 similar to that of dogbone specimen in Figure 5.3 - biaxial loads to failure - failed in torsion
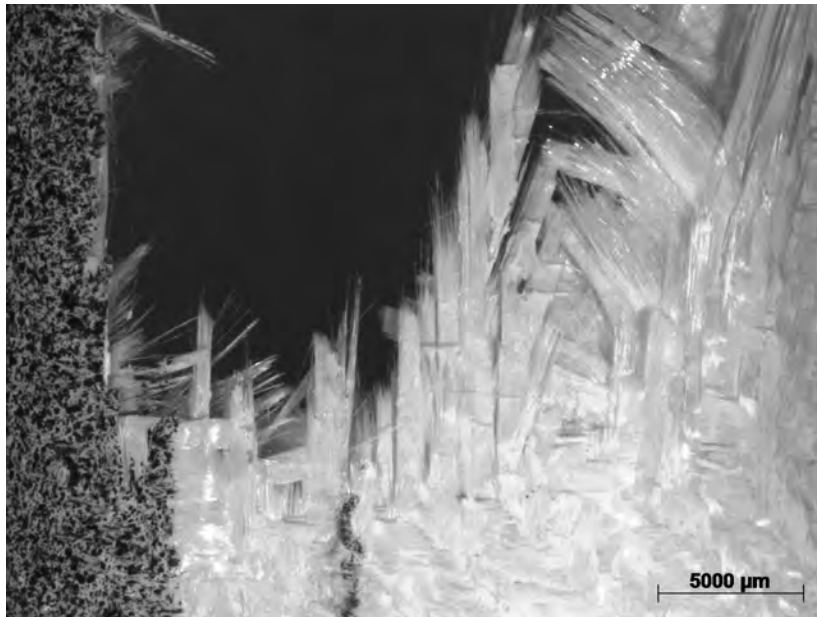
Figure 5.35: Failure site damage in Nextel[TM] 720/AS oxide-oxide involute tube specimen 12-064 - biaxial loads to failure - failed in torsion
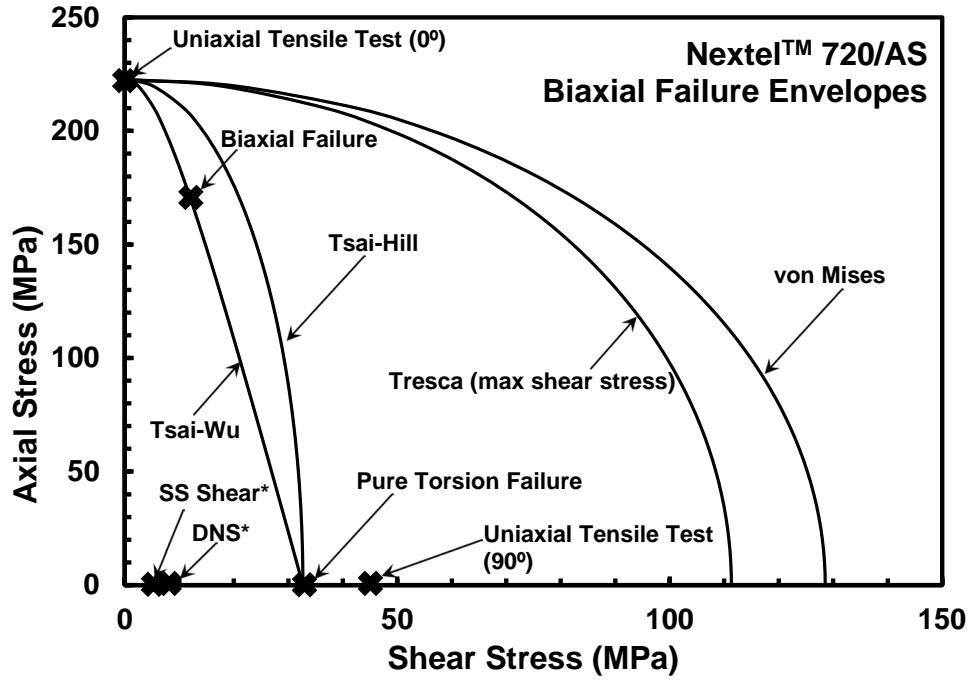
Figure 5.36: Failure envelope of an oxide-oxide CMC thin-wall involute tube

VI. Conclusions and Recommendations

A biaxial (tension-torsion) testing and computational model verification and validation procedure for oxide-oxide CMC involute tubes at room temperature was developed. Uniaxial stress-strain responses were found to be useful in determining expected loads and gripping pressures necessary for biaxial (tension-torsion) loading[28]. Both pure torsion and combined tension-torsion of an oxide-oxide CMC involute tube at room temperature was investigated. The oxide-oxide CMC involute tube exhibited USS of 32.68 MPa in pure torsion and UTS of 171.74 MPa and USS of 11.83 MPa under tension-torsion. Failure strains of 0.31% and 0.32% in pure torsion and tension-torsion, respectively, were observed.

Computational model verification and validation data was obtained through the use of DIC. This method of displacement and strain measurements offered the fidelity required heterogeneous CMC materials. Crack initiation and crack propagation was detected in addition to providing displacement and strain information down to the fiber tow level. The spatial resolution of DIC systems is higher when implemented with a speckle pattern of appropriate size.

As temperature increased, very little change in UTS or failure strain was seen. Relief in residual stresses at elevated temperatures in combination with test specimen scatter could explain test results[45].

The biaxial (tension-torsion) procedures developed can be used to generate a more statistically significant series of test results for UTS and USS with incorporation of Weibull analysis[22]. Additionally, composite microstructure and likely damage and failure mechanisms can be studied.

Recommendations include biaxial (tension-torsion) loadframe tuning utilizing a brittle material due to observed load outputs and careful consideration of DIC image acquisition.

Loadframe tuning can be accomplished with additional time and specimen quantities. Both of these resources were scarce in the testing documented in this manuscript, but future endeavors should consider this a priority before testing.

To gain more DIC resolution, starting DIC data acquisition once a desired load of 20-50% of expected failure loads have been achieved, could be implemented with the same DIC system and no additional costs. Along with careful speckling procedures, this brief delay in image capture would allow for loading rates to remain at lower rates, like 1-2 MPa/second, and not require the acquisition of a large number of unneeded DIC stage points. Had this been implemented in the biaxial (tension-torsion) test on specimen 12-064, it is reasonable to assume that higher fidelity would have been achieved in the Aramis DIC results.

Appendix A

Figure 6.1: MTS Station Manager straightsided specimen room temperature displacement to failure procedure

Type	Name	Start	Interrupt
	Data Acquisition	<Procedure>.Start	
	Specimen Zero Force Command	<Procedure>.Start	
	Specimen Zero Force Hold	Specimen Zero Force Command.Done	Right Furnace to 1063ºC.Done Left Furnace to 1092ºC.Done
	Right Furnace to 700ºC	Specimen Zero Force Command.Done	
	Left Furnace to 700ºC	Specimen Zero Force Command.Done	
	Right Furnace to 1063ºC	Right Furnace to 700ºC.Done Left Furnace to 700ºC.Done	
	Left Furnace to 1092ºC	Right Furnace to 700ºC.Done Left Furnace to 700ºC.Done	
	Load to Failure	Right Furnace to 1063ºC.Done Left Furnace to 1092ºC.Done	Compression Failure Detector.Done
	Compression Failure Detector	<Procedure>.Start	
	Left Oven Off	Compression Failure Detector.Done	
	Right Oven Off	Compression Failure Detector.Done	

Procedure is done when	Left Oven Off.Done Right Oven Off.Done

Figure 6.2: Nextel™ 720/AS DNS ILSS monotonic compression to failure test procedures

Figure 6.3: Nextel™ 720/AS DNS interlaminar shear creep test procedures

Type	Name	Start	Interrupt
	Start Aramis - 1 pic/sec	<Procedure>.Start	
	Timed Acquisition 1	<Procedure>.Start	
	Ramp to 50 MPa	<Procedure>.Start	
	Unload from 50 MPa to 0 MPa	Ramp to 50 MPa.Done	
	Ramp to 100 MPa	Unload from 50 MPa to 0 MPa.Done	
	Unload from 100 MPa to 0 MPa	Ramp to 100 MPa.Done	
	Ramp to 150 MPa	Unload from 100 MPa to 0 MPa.Done	
	Unload from 150 MPa to 0 MPa	Ramp to 150 MPa.Done	
	Ramp to 200 MPa	Unload from 150 MPa to 0 MPa.Done	
	Unload from 200 MPa to 0 MPa	Ramp to 200 MPa.Done	
	Ramp to 250 MPa	Unload from 200 MPa to 0 MPa.Done	
	Unload from 250 MPa to 0 MPa	Ramp to 250 MPa.Done	
	Ramp to 300 MPa	Unload from 250 MPa to 0 MPa.Done	
	Unload from 300 MPa to 0 MPa	Ramp to 300 MPa.Done	
	Ramp to 350 MPa	Unload from 300 MPa to 0 MPa.Done	
	Unload from 350 MPa to 0 MPa	Ramp to 350 MPa.Done	
	Ramp to 400 MPa	Unload from 350 MPa to 0 MPa.Done	
	Unload from 400 MPa to 0 MPa	Ramp to 400 MPa.Done	
	Limit Stop	<Procedure>.Start	

Procedure is done when	Unload from 400 MPa to 0 MPa.Done

Figure 6.4: Room temperature uniaxial test incorporating DIC

107

Figure 6.5: Elevated temperature (1100°C) uniaxial Nextel™ 720/AS dogbone specimen test procedure

Type	Name	Start	Interrupt
	Data Acquisition	<Procedure>.Start	
	Failure Detector	<Procedure>.Start	
	Zero Specimen Load	<Procedure>.Start	
	Hold Zero Specimen Load	Zero Specimen Load.Done	Right Furnace Ramp up to 1100ºC - 1086ºC Setpoint.Done Left Furnace Ramp up to 1100ºC - 1103ºC Setpoint.Done
	Right Furnace Ramp up to 1100ºC - 1086ºC Setpoint	<Procedure>.Start	
	Left Furnace Ramp up to 1100ºC - 1103ºC Setpoint	<Procedure>.Start	
	Ramp to 50 MPa	Hold Zero Specimen Load.Done	Failure Detector.Done
	Unload from 50 MPa to 0 MPa	Ramp to 50 MPa.Done	
	Ramp to 100 MPa	Unload from 50 MPa to 0 MPa.Done	Failure Detector.Done
	Unload from 100 MPa to 0 MPa	Ramp to 100 MPa.Done	
	Ramp to 150 MPa	Unload from 100 MPa to 0 MPa.Done	Failure Detector.Done
	Unload from 150 MPa to 0 MPa	Ramp to 150 MPa.Done	
	Ramp to 200 MPa	Unload from 150 MPa to 0 MPa.Done	Failure Detector.Done
	Unload from 200 MPa to 0 MPa	Ramp to 200 MPa.Done	
	Ramp to 250 MPa	Unload from 200 MPa to 0 MPa.Done	Failure Detector.Done
	Unload from 250 MPa to 0 MPa	Ramp to 250 MPa.Done	
	Ramp to 300 MPa	Unload from 250 MPa to 0 MPa.Done	Failure Detector.Done
	Unload from 300 MPa to 0 MPa	Ramp to 300 MPa.Done	
	Ramp to 350 MPa	Unload from 300 MPa to 0 MPa.Done	Failure Detector.Done
	Unload from 350 MPa to 0 MPa	Ramp to 350 MPa.Done	
	Ramp to 400 MPa	Unload from 350 MPa to 0 MPa.Done	Failure Detector.Done
	Unload from 400 MPa to 0 MPa	Ramp to 400 MPa.Done	
	Right Oven Off	Failure Detector.Done	
	Left Oven Off	Failure Detector.Done	

Procedure is done when: Left Furnace Ramp up to 1100ºC - 1103ºC Setpoint.Done
Right Furnace Ramp up to 1100ºC - 1086ºC Setpoint.Done

Type	Name	Start	Interrupt
	Data Acquisition	<Procedure>.Start	
	Zero Specimen Load	<Procedure>.Start	Right Furnace Ramp up to 1100ºC.Done Left Furnace Ramp up to 1100ºC.Done
	Hold Zero Specimen Load	Zero Specimen Load.Done	Right Furnace Ramp up to 1100ºC.Done Left Furnace Ramp up to 1100ºC.Done
	Right Furnace Ramp up to 1100ºC	<Procedure>.Start	
	Left Furnace Ramp up to 1100ºC	<Procedure>.Start	
	Displacement 0.05 mm/sec	Hold Zero Specimen Load.Done	

Procedure is done when | Displacement 0.05 mm/sec.Done

Figure 6.6: Elevated temperature (1100°C) uniaxial Nextel™ 720/AS straightsided specimen test procedure

Type	Name	Start	Interrupt
	Timed Acquisition	<Procedure>.Start	
	Aramis Trigger Start	<Procedure>.Start	
	Torsion Failure Load with Zero Axial Force Hold	<Procedure>.Start	Specimen Failure Load Protection.Done
	Specimen Failure Load Protection	Torsion Failure Load with Zero Axial Force Hold.Done	
	Unload from Failure Load Protection	Specimen Failure Load Protection.Done	

Procedure is done when	Unload from Failure Load Protection.Done

Figure 6.7: MTS Station Manager oxide-oxide CMC involute tube monotonic torsion to failure procedure with Aramis DIC 1/sec trigger

110

Type	Name	Start	Interrupt
	Timed Acquisition	<Procedure>.Start	
	Aramis Trigger Start	<Procedure>.Start	
	100%UTS Axial Load with 50%USS Torsion Torque	<Procedure>.Start	

Procedure is done when	100%UTS Axial Load with 50%USS Torsion Torque.Done

Figure 6.8: MTS Station Manager oxide-oxide CMC involute tube biaxial (tension-torsion) to failure procedure with Aramis DIC 1/sec trigger

Figure 6.9: DNS specimens before cleaning

Figure 6.10: DNS specimens during first cleaning
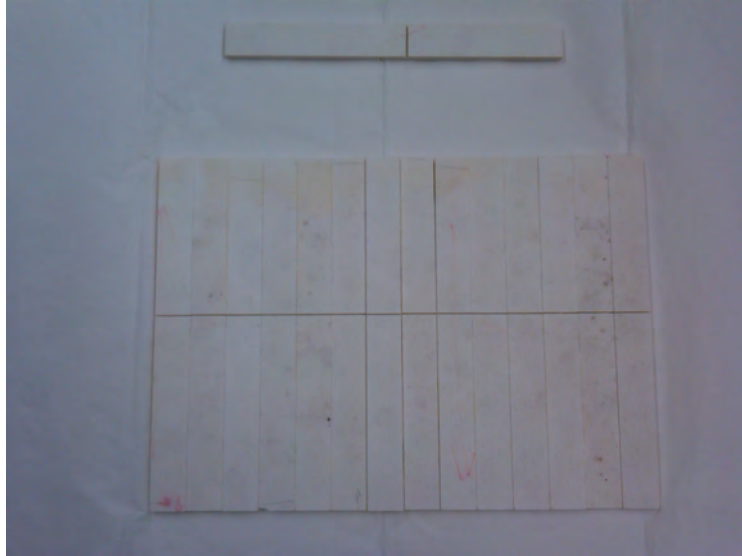
Figure 6.11: DNS specimens after first cleaning

Figure 6.12: DNS specimens during 25 minute ultrasonic acetone bath
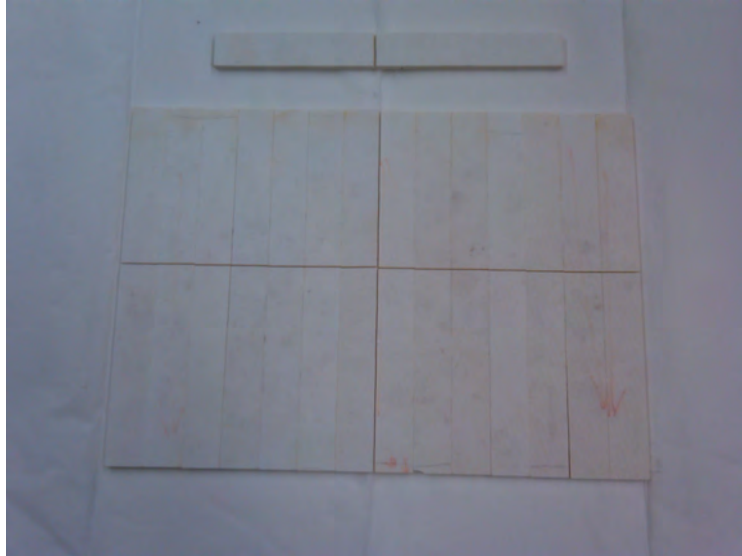
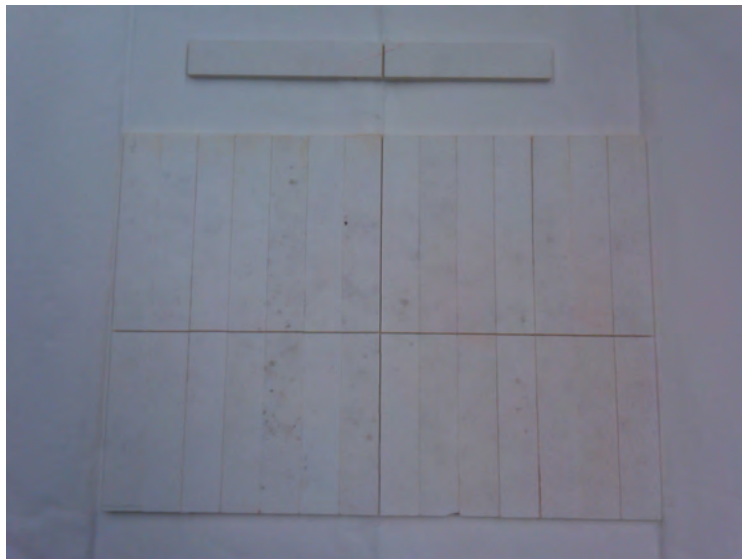Figure 6.13: Side 1 of DNS specimens before 100°C 16 hour bakeout

Figure 6.14: Side 2 of DNS specimens before 100°C 16 hour bakeout

Figure 6.15: DNS specimen bakeout furnace
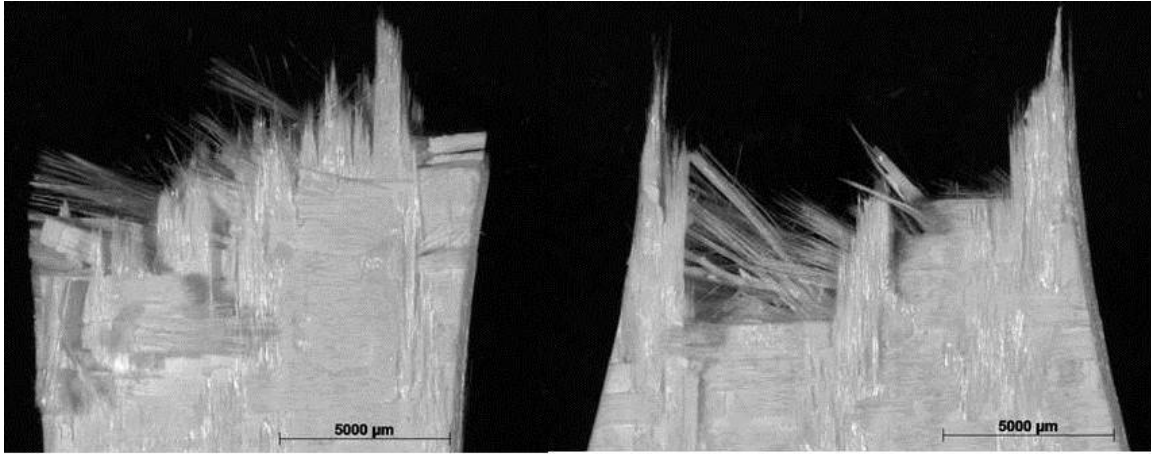

Figure 6.16: DNS specimens bakeout setup

Figure 6.17: Dogbone Specimen 12-109 - 0° involute layup - 1100°C in air - Nextel^{TM} 720/AS
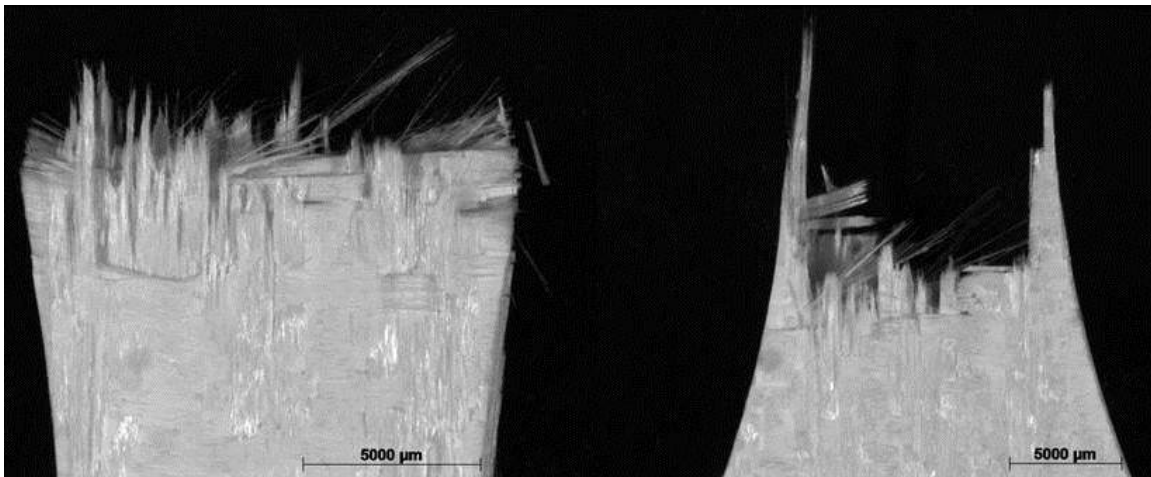

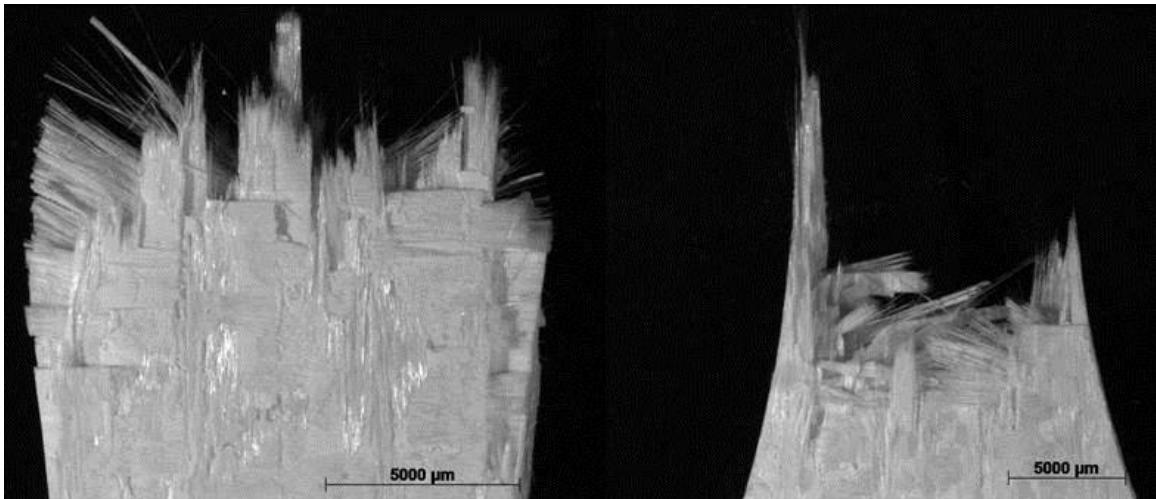Figure 6.18: Dogbone Specimen 12-111 - 0° involute layup - 1100°C in air - Nextel^{TM} 720/AS

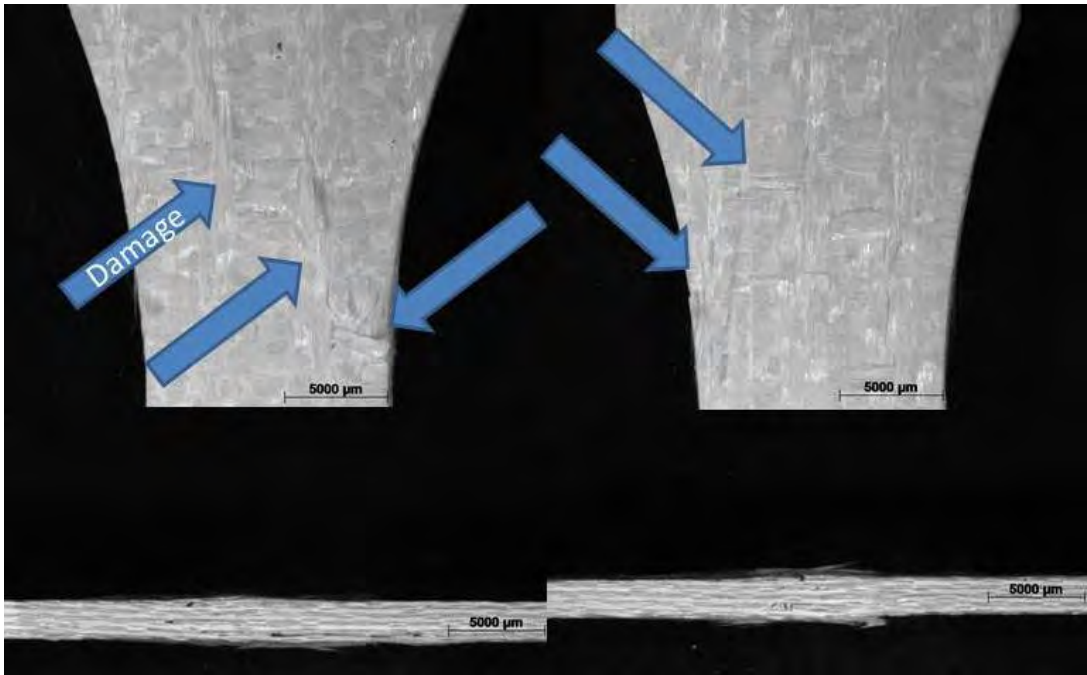Figure 6.19: Dogbone Specimen 12-113 - 0° involute layup - 1100°C in air - Nextel^{TM} 720/AS

Figure 6.20: Dogbone Specimen 12-110 - 0° involute layup - room temperature in air - Nextel^{TM} 720/AS
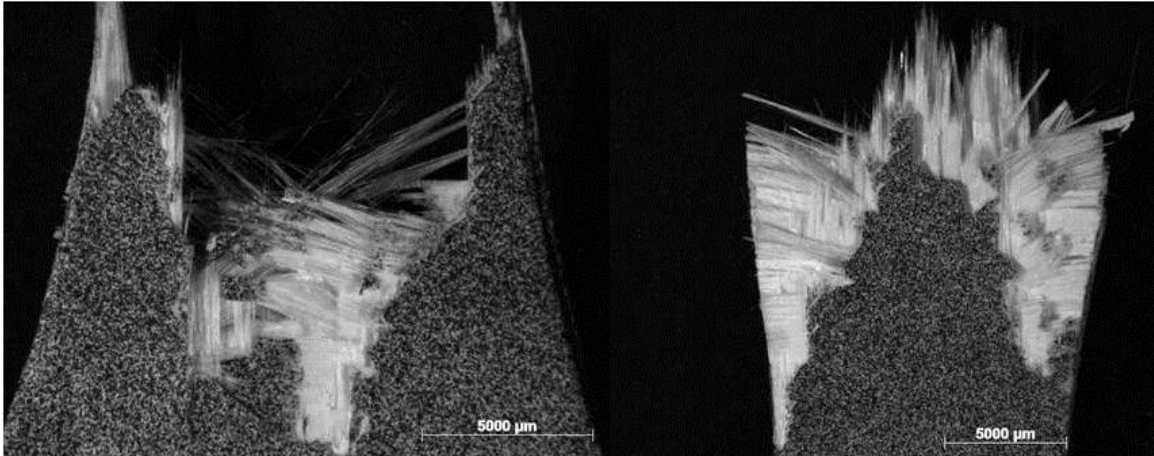
Figure 6.21: Dogbone Specimen 12-112 - 0° involute layup - DIC test at room temperature in air - Nextel^{TM} 720/AS
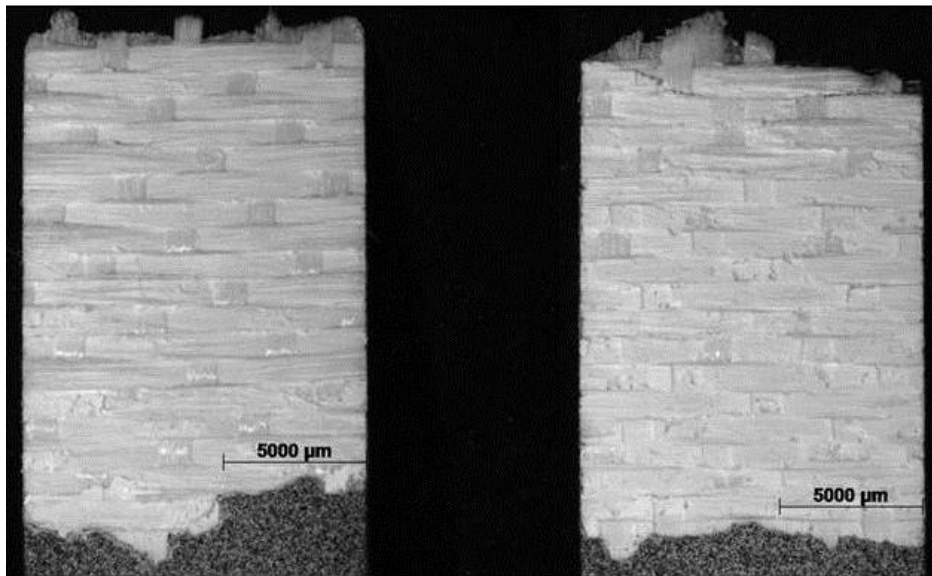

Figure 6.22: Straightsided Specimen 12-098 - 90° involute layup - DIC test at room temperature in air - Nextel^{TM} 720/AS
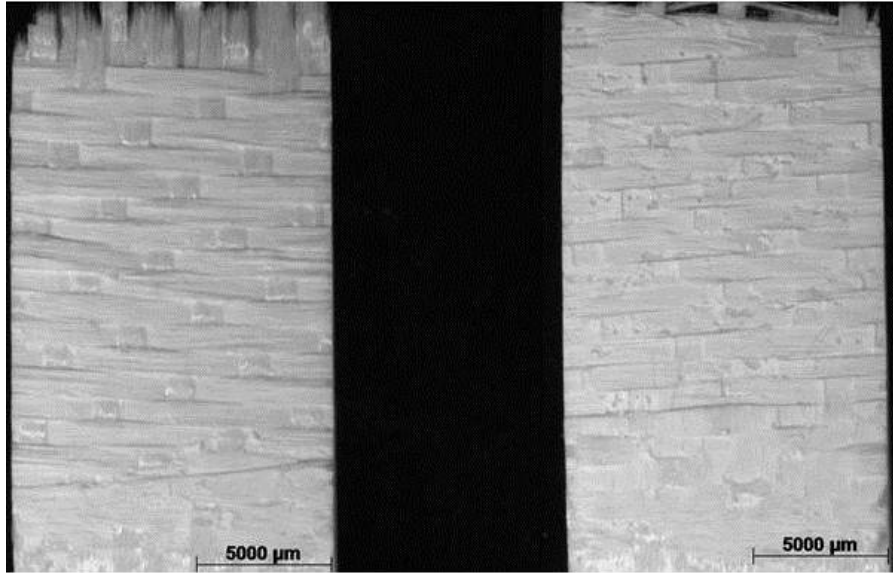
Figure 6.23: Straightsided Specimen 12-106 - 90° involute layup - room temperature in air - Nextel™ 720/AS
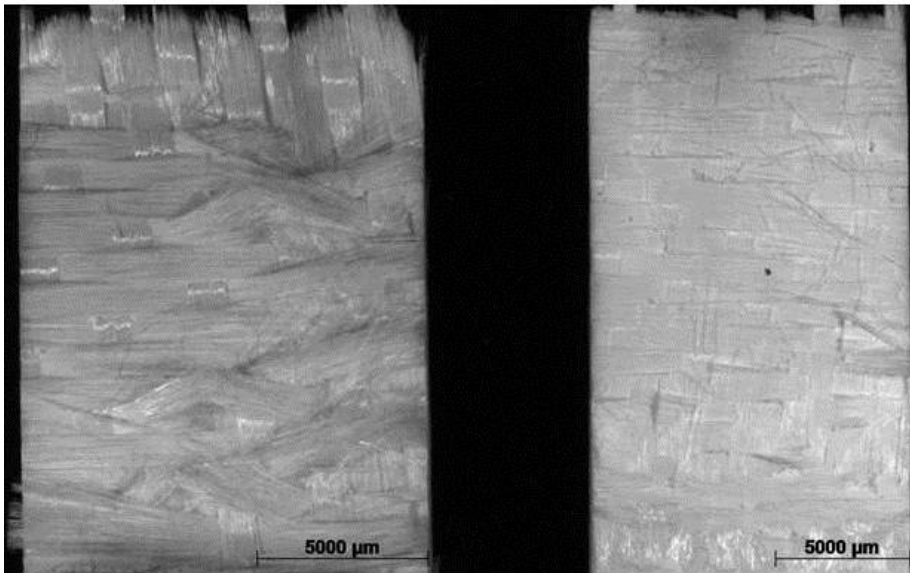

Figure 6.24: Straightsided Specimen 12-099 - 90° involute layup - 1100°C in air - Nextel™ 720/AS
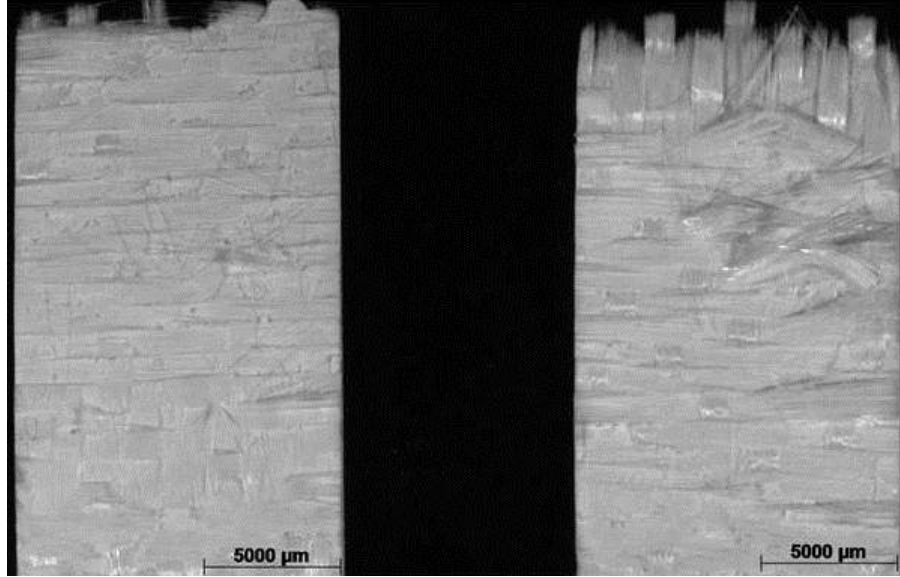
Figure 6.25: Straightsided Specimen 12-100 - 90° involute layup - 1100°C in air - Nextel^{TM} 720/AS
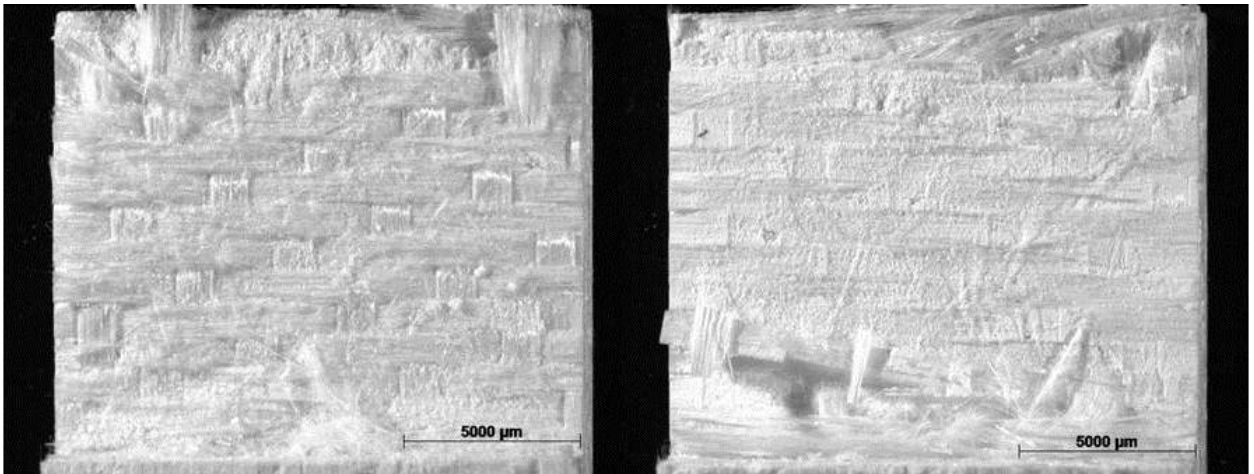
Figure 6.26: DNS Specimen 2 - ILSS test at 1100°C in air - Nextel^{TM} 720/AS
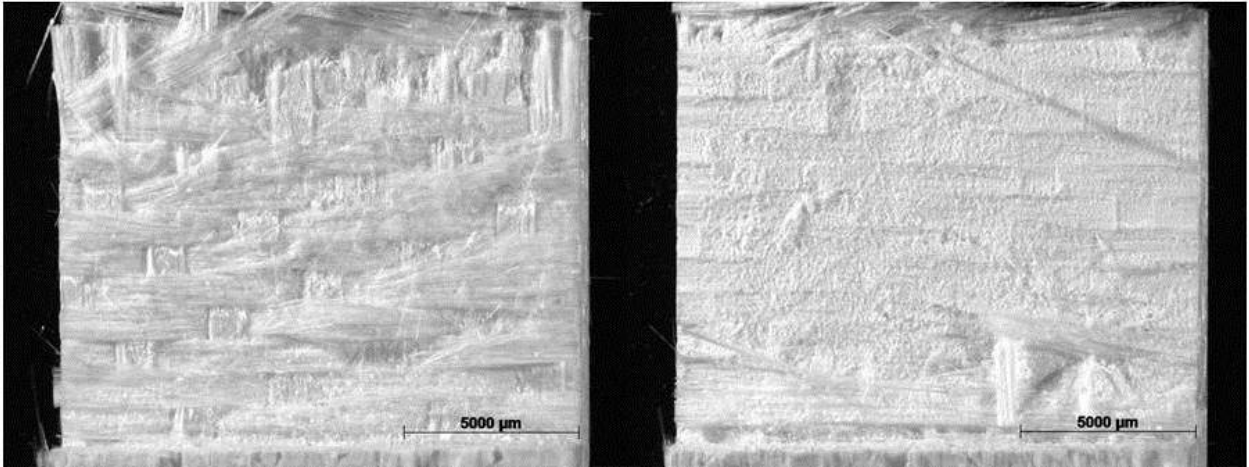
Figure 6.27: DNS Specimen 3 - ILSS test at 1100°C in air - Nextel^{TM} 720/AS

Figure 6.28: DNS Specimen 4 - interlaminar creep at 1100°C in air - 6 MPa - Nextel^{TM} 720/AS - failed

Figure 6.29: DNS Specimen 6 - interlaminar creep at 1100°C in air - 5 MPa - Nextel™ 720/AS

Figure 6.30: DNS Specimen 7 - interlaminar creep at 1100°C in air - 4 MPa - Nextel™ 720/AS

Figure 6.31: DNS Specimen 8 - interlaminar creep at 1100°C in air - 2 MPa - Nextel[TM] 720/AS
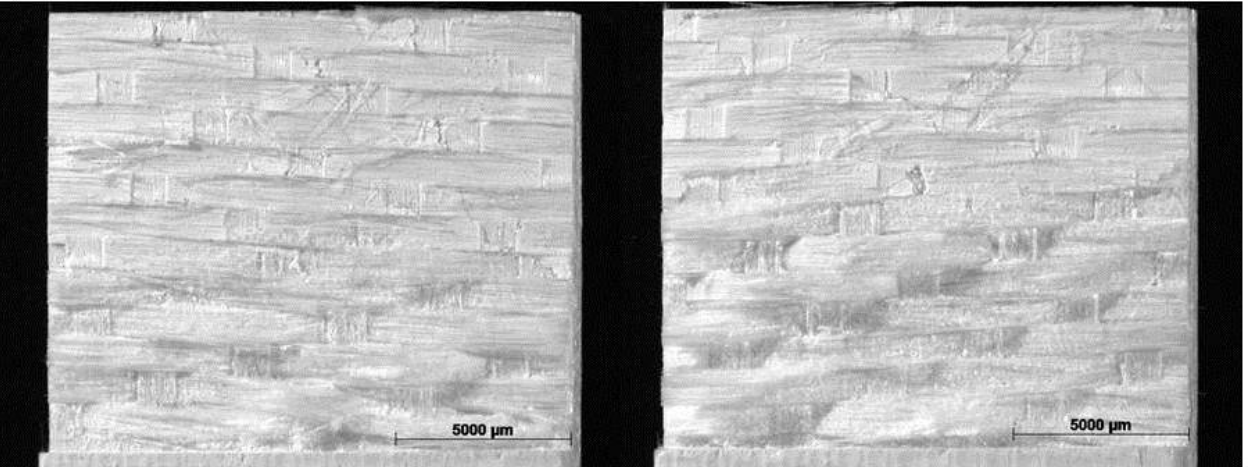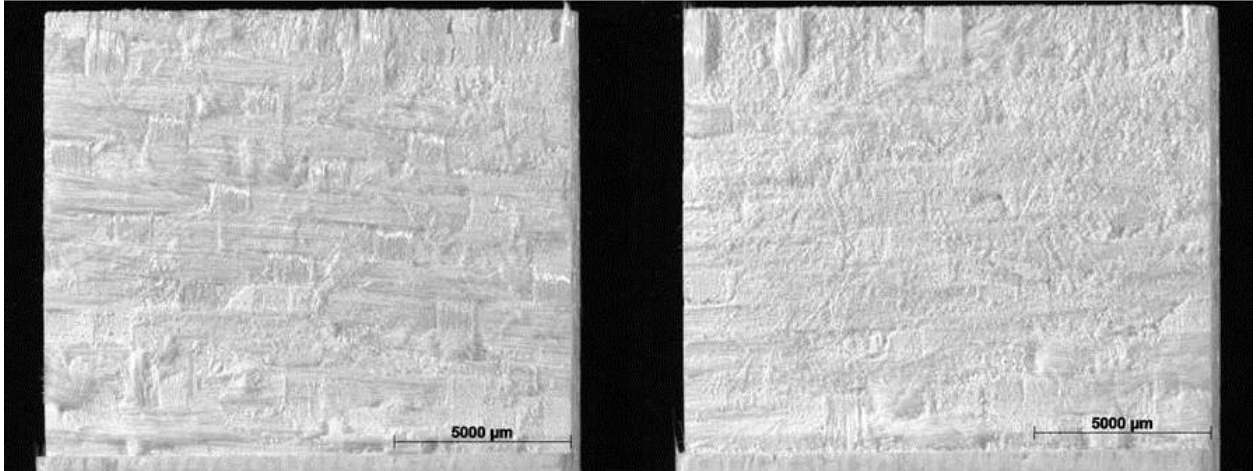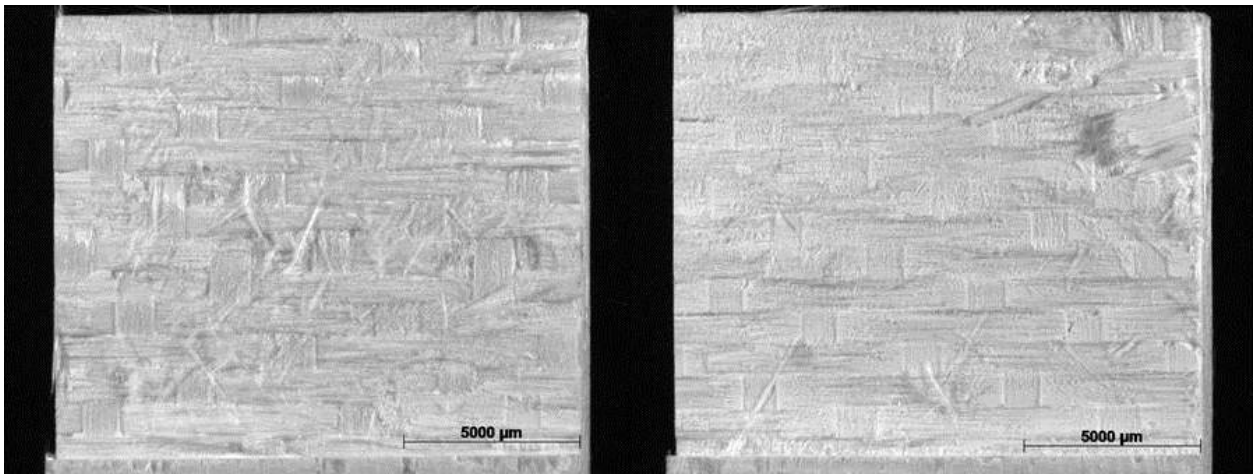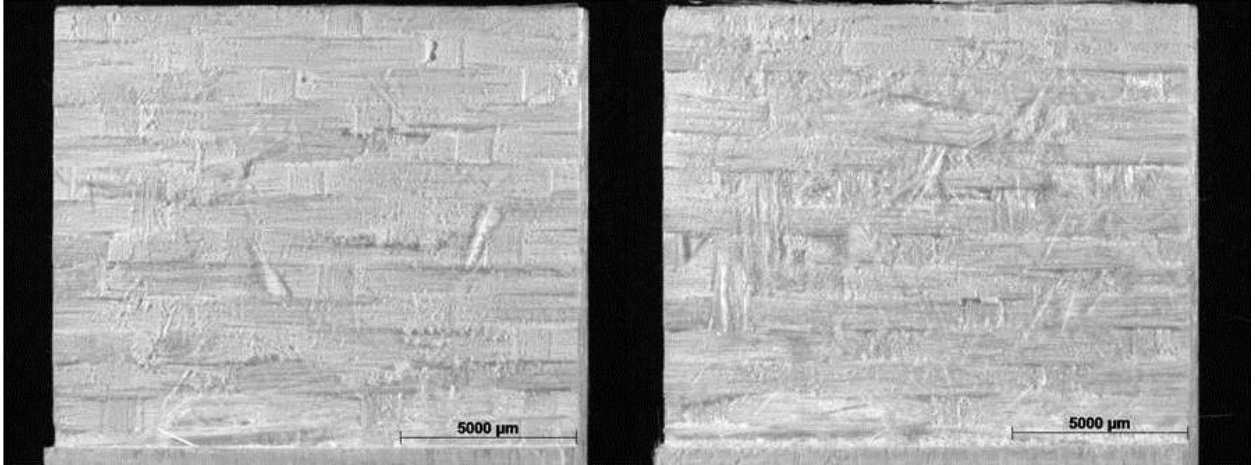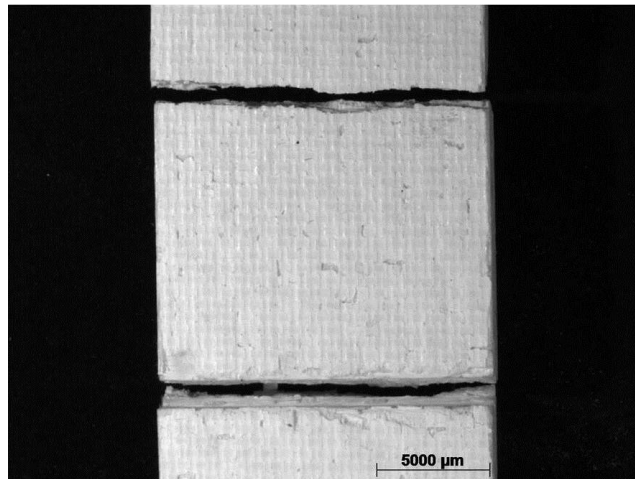

Figure 6.32: DNS Specimen 10 - interlaminar creep at 1100°C in steam - 6 MPa - Nextel[TM] 720/AS
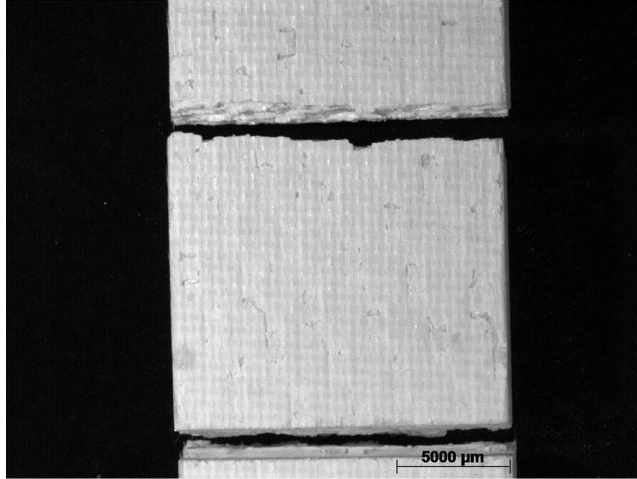
Figure 6.33: DNS Specimen 11 - interlaminar creep at 1100°C in steam - 6 MPa - Nextel^{TM} 720/AS
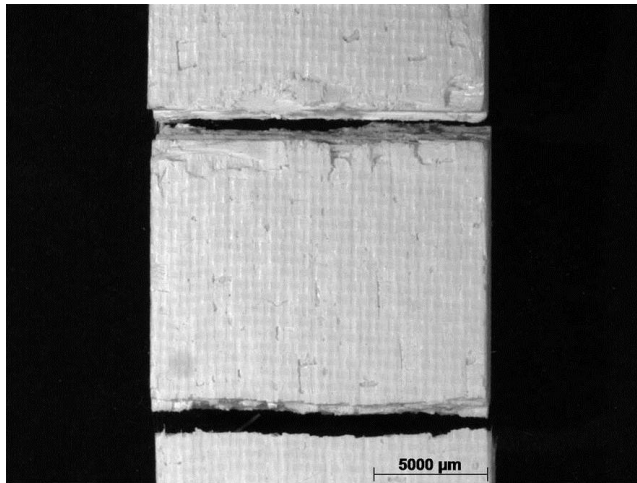

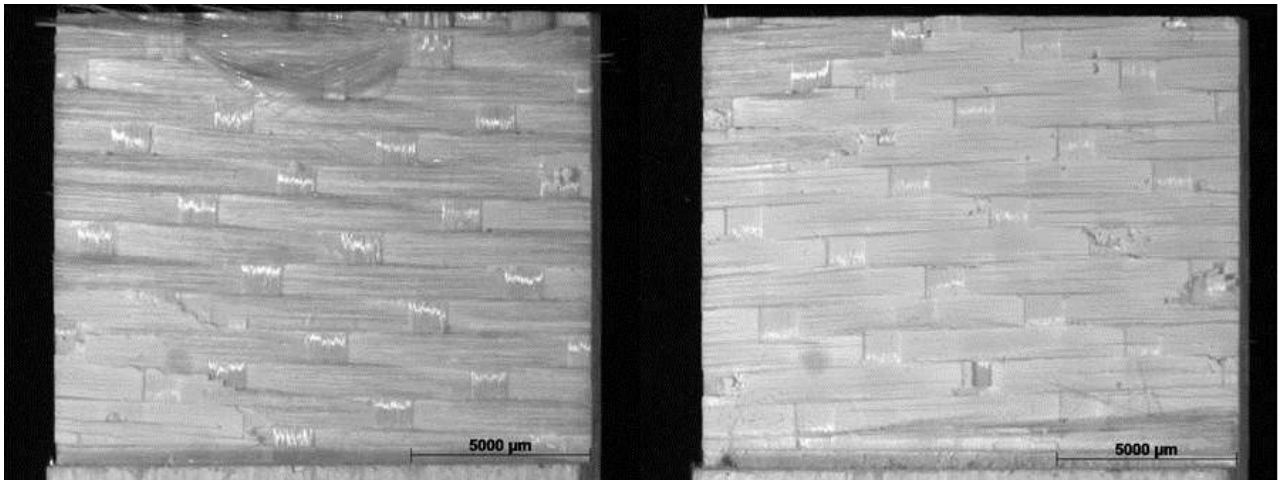Figure 6.34: DNS Specimen 12 - interlaminar creep at 1100°C in steam - 6 MPa - Nextel^{TM} 720/AS

Figure 6.35: DNS Specimen 13 - Nextel^{TM} 720/AS - failed prior to testing

Bibliography

[1] "2310 Instruction Manual". *2300 System Strain Gage Conditioning Amplifier*. Raleigh, NC: Vishay Measurements Group.

[2] "3M Nextel™ Ceramic Fiber Typical Properties". *3M Nextel™ Ceramic Textiles Technical Notebook*. St. Paul, MN: 3M Corporation.

[3] "Average Physical, Mechanical, and Thermal Properties". *COI Ceramics, Inc*. San Diego, CA: COI Ceramics. Printed 8 April 2010.

[4] "Instruction Manual". *Model 1550A Strain Indicator Calibrator*. Raleigh, NC: Vishay Measurements Group.

[5] "Series 646 Hydraulic Collet Grips Product Information: Model 646.10 and 646.25". *Manual Part Number 011-558-204 D*. Eden Prairie, MN: MTS Systems Corporation. June 2001.

[6] "DMBZ polyimides provide an alternative to PMR-15 for high-temperature applications". *NASA Technical Memorandum*, (107111):55 – 55, 1996.

[7] Amijima, S., T. Fujii, and M. Hamaguchi. "Static and fatigue tests of a woven glass fabric composite under biaxial tension-torsion loading". *Composites*, 22:281–289, July 1991.

[8] Ashby, M.F. *Materials Selection in Mechanical Design*. Burlington, MA: Butterworth-Heinemann, 2005.

[9] ASTM Standard C 1425-11, 2011. "Standard Test Method for Interlaminar Shear Strength of 1D and 2D Continuous Fiber-Reinforced Advanced Ceramics at Elevated Temperatures". ASTM International, West Conshohocken, PA, 1999, DOI: 10.1520/C1425-11, www.astm.org.

[10] ASTM Standard E 2207-08, 2008. "Standard Practice for Strain-Controlled Axial-Torsional Fatigue Testing with Thin-Walled Tubular Specimens". ASTM International, West Conshohocken, PA, 2002, DOI: 10.1520/E2207-08, www.astm.org.

[11] Boakye, E.E., R.S. Hay, P. Mogilevsky, and L.M. Douglas. "Monazite Coatings on Fibers: II, Coating without Strength Degradation". *Journal of the American Ceramic Society*, 84:2793–2801, December 2001.

[12] Bouchetou, M.L., M. Huger, D. Fargeot, and C. Gault. *Effect of the Environment on CMCs*. In A.G. Evans, R. Naslain (eds.) *High-Temperature Ceramic-Matrix Compsites I: Design, Durability, and Performance*. Westerville, OH: The American Ceramic Society, 1995.

[13] Chawla, K.K. *Ceramic Matrix Composites*. Boston: Kluwer Academic, 2nd edition, 2003.

[14] Dally, J.W. and W.F. Riley. *Experimental Stress Analysis*. New York: McGraw-Hill, 3rd edition, 1991.

[15] Daniel, I.M. and O. Ishai. *Engineering Mechanics of Composite Materials*. New York: Oxford University Press, 2006.

[16] Dowling, N.E. *Mechanical Behavior of Materials: Engineering Methods for Deformation, Fracture, and Fatigue*. Upper Saddle River, NJ: Pearson/Prentice Hall, 3rd edition, 2007.

[17] Duval, D.J., S. H. Risbud, and J. F. Shackelford. *Chapter 2: Mullite*. In J.F. Shackelford, R.H. Doremus (eds.) *Ceramic and Glass Materials: Structure, Properties and Processing*. New York: Springer, 2008.

[18] Gadow, R. "Ceramic layer composites in advanced automotive engineering and biomedical applications". *Key Engineering Materials*, 333:177–194, 2007.

[19] Gower, M.R.L. and R.M. Shaw. "Towards a Planar Cruciform Specimen for Biaxial Characterisation of Polymer Matrix Composites". *Applied Mechanics and Materials*, 24-25:115–120, June 2010.

[20] Green, D.J. *An Introduction to the Mechanical Properties of Ceramics*. Cambridge: Cambridge UP, 1998.

[21] Holmquist, M.G., T.C. Radsick, O.H. Sudre, and F.F. Lange. "Fabrication and testing of all-oxide CFCC tubes". *Composites*, 34:163–170, October 2002.

[22] Kawai, N., T. Kotani, Y.Kakimoto, and E. Sato. "Fracture behavior of silicon nitride ceramics under combined compression-torsion stresses analyzed by multiaxial fracture statistics". *European Ceramic Society*, 31:1827–1833, April 2011.

[23] Kingery, W. D., H. K. Bowen, and D. R Uhlmann. *Introduction to Ceramics*. New York: Wiley, 2nd edition, 1976.

[24] Laffey, P.D. *The Effects of Environment on the Interlaminar Shear Performance of an Oxide/Oxide Ceramic Matrix Composite at Elevated Temperature*. MS thesis, AFIT/GAE/ENY/07-J11. School of Engineering and Management, Air Force Institute of Technology (AU), Wright-Patterson Air Force Base, OH, June 2007.

[25] Levi, C.G., J.Y. Yang, B.J. Dalgleish, F.W. Zok, and A.G. Evans. "Processing and Performance of an All-Oxide Ceramic Composite". *Journal of the American Ceramic Society*, 81:2077–86, August 1998.

[26] Liao, Kin, Eric R. George, and Kenneth L. Reifsnider. "Characterization of Ceramic Matrix Composite Tubes Under Uniaxial/Biaxial Monotonic and Cyclic Loading". *ASTM*, 1280:224–240, 1997.

[27] Mattingly, J.D. *Elements of Propulsion: Gas Turbines and Rockets*. Reston, VA: American Institute of Aeronautics and Astronautics, 2005.

[28] Nohut, S., A. Usbeck, H. Özcoban, D. Krause, and G.A. Schneider. "Determination of the multiaxial failure criteria for alumina ceramics under tension-torsion test". *European Ceramic Society*, 30:3339–3349, August 2010.

[29] Pan, Bing, Kemao Qian, Huimin Xie, and Anand Asundi. "Two-dimensional digital image correlation for in-plane displacement and strain measurement: a review". *Measurement Science and Technology*, 20:1–17, April 2009.

[30] Parlier, M., M.-H. Ritti, and A. Jankowiak. "Potential and Perspectives for Oxide/Oxide Composites". *Aerospace Lab Journal*, 1–12, November 2011.

[31] Petrovic, J.J. and M.G. Stout. "Fracture of Al_2O_3 in Combined Tension/Torsion: I, Experiments". *Journal of the American Ceramic Society*, 64:656–660, May 1981.

[32] Pope, Matthew T. *Creep Behavior in Interlaminar Shear of a CVI SIC/SIC Composite at Elevated Temperature in Air and in Steam*. MS thesis, AFIT/GMS/ENY/12-M02. School of Engineering and Management, Air Force Institute of Technology (AU), Wright-Patterson Air Force Base, OH, March 2012.

[33] Rajan, V.P., M.N. Rossol, and F.W. Zok. "Optimization of Digital Image Correlation for High-Resolution Strain Mapping of Ceramic Composites". *Experimental Mechanics*, April 2012.

[34] Ray, Indrajit, George C. Parish, Julio F. Davalos, and An Chen. "Effect of Concrete Substrate Repair Methods for Beams Aged by Accelerated Corrosion and Strengthened with CFRP". *Journal of Aerospace Engineering*, 24(2):227–239, 2011.

[35] Ruggles-Wrenn, M. B. and T. Kutsal. "Effects of steam environment on creep behavior of Nextel[TM] 720/alumina-mullite ceramic composite at elevated temperature". *Composites Part A-Applied Science and Manufacturing*, 41(12):1807–1816, December 2010.

[36] Ruggles-Wrenn, M. B., A. T. Radzicki, S. S. Baek, and K. A. Keller. "Effect of loading rate on the monotonic tensile behavior and tensile strength of an oxide-oxide ceramic composite at 1200° C". *Materials Science and Engineering: A (Structural Materials: Properties, Microstructure and Processing)*, 492(1-2):88–94, September 2008.

[37] Ruggles-Wrenn, M. B. and B. A. Whiting. "Cyclic creep and recovery behavior of Nextel[TM] 720/alumina ceramic composite at 1200°C". *Materials Science and*

Engineering: A (Structural Materials: Properties, Microstructure and Processing), 528(3):1848–1856, January 2011.

[38] Ruggles-Wrenn, M.B. and J.C. Braun. "Effects of steam environment on creep behavior of Nextel[TM] 720/alumina ceramic composite at elevated temperature". *Materials Science and Engineering: A (Structural Materials: Properties, Microstructure and Processing)*, 497:101–10, December 2008.

[39] Ruggles-Wrenn, M.B., J. Delapasse, A.L. Chamberlain, J.E. Lane, and T.S. Cook. "Fatigue behavior of a Hi-Nicalon[TM]/SiC$-$B$_4$C composite at 1200°C in air and in steam". *Materials Science and Engineering: A (Structural Materials: Properties, Microstructure and Processing)*, 534(0):119 – 128, 2012.

[40] Ruggles-Wrenn, M.B., S. Mall, C.A. Eber, and L.B. Harlan. "Effects of steam environment on high-temperature mechanical behavior of Nextel[TM] 720/alumina (N720/A) continuous fiber ceramic composite". *Composites Part A (Applied Science and Manufacturing)*, 37:2029–40, November 2006.

[41] Ruggles-Wrenn, M.B. and M. Ozer. "Creep behavior of Nextel[TM] 720/alumina-mullite ceramic composite with ±45deg fiber orientation at 1200°C". *Materials Science and Engineering: A (Structural Materials: Properties, Microstructure and Processing)*, 527:5326–34, July 2010.

[42] Stout, M.G. and J.J. Petrovic. "Multiaxial Loading Fracture of Al$_2$O$_3$ Tubes: I, Experiments". *Journal of the American Ceramic Society*, 67:14–18, January 1984.

[43] Szweda, A., S. Butner, J. Ruffoni, C Bacalsk, J. Lane, J. Morrison, G Merrill, M. van Roode, A Fahme, N. Miriyala, and D. Leroux. "Development and Evaluation of Hybrid Oxide/Oxide Ceramic Matrix Composite Combustor Liners". *ASME*, 67:14–18, January 1984.

[44] Van Roode, M., J. Price, J. Kimmel, N. Miriyala, D. Leroux, A. Fahme, and K. Smith. "Ceramic Matrix Composite Combustor Liners: A Summary of Field Evaluations". *Journal of Engineering of Gas Turbine and Power*. **129**: 21-30 (January 2007).

[45] Venables, J.D. "High Temperature Structural Materials". *Encyclopedia of Life Support Systems*. February 2013. www.eolss.net/Sample-Chapters/C05/E6-36-02-03.pdf.

[46] Yeh, Hsien-Yang, Sean V. Nguyen, and Hsien-Liang Yeh. "Failure analyses of polymer matrix composite (PMC) honeycomb sandwich joint panels". *Journal of Reinforced Plastics and Composites*, 23(9):923 – 939, 2004. ISSN 07316844.

[47] Zawada, L.P. and S.S. Lee. "Evaluation of four CMCs for aerospace turbine engine divergent flaps and seals". *Ceramic Engineering and Science Proceedings*, 16:337–339, 1995.

[48] Zok, F.W. and C.G. Levi. "Mechanical Properties of Porous-Matrix Ceramic Composites". *Advanced Engineering Materials*, 3:15–23, 2001.

Vita

Captain Joseph M. DeRienzo is a 2002 graduate of West Florence High School (Florence, SC) and 2006 graduate of the United States Air Force Academy (Colorado Springs, CO). After earning his Bachelor of Science degree in General Engineering in May of 2006 he was commissioned as a 2d LT in the world's greatest air, space, and cyberspace force; the United States Air Force. Captain DeRienzo served at Edwards Air Force Base, CA planning and executing F-16 and T-38 avionics and engine flight test for four years. It was there he met his future wife and solidified his love of experimentation, especially flight test. After 10 months at the Compressor Research Facility within the Air Force Research Lab's Propulsion Directorate, Wright-Patterson, AFB, OH, he was assigned to the Air Force Institute of Technology. After graduation Captain DeRienzo will be assigned to the United States Air Force Space and Missile Command, Los Angeles AFB, CA.

REPORT DOCUMENTATION PAGE

Form Approved
OMB No. 0704–0188

1. REPORT DATE *(DD–MM–YYYY)*	2. REPORT TYPE	3. DATES COVERED *(From — To)*
21–03–2013	Master's Thesis	May 2010–Mar 2012

4. TITLE AND SUBTITLE

Biaxial (Tension-Torsion) Testing of an Oxide/Oxide Ceramic Matrix Composite

5a. CONTRACT NUMBER

5b. GRANT NUMBER

5c. PROGRAM ELEMENT NUMBER

6. AUTHOR(S)

DeRienzo, Joseph M., Captain, USAF

5d. PROJECT NUMBER

5e. TASK NUMBER

5f. WORK UNIT NUMBER

7. PERFORMING ORGANIZATION NAME(S) AND ADDRESS(ES)

Air Force Institute of Technology
Graduate School of Engineering and Management (AFIT/EN)
2950 Hobson Way
WPAFB, OH 45433-7765

8. PERFORMING ORGANIZATION REPORT NUMBER

AFIT-ENY-13-M-10

9. SPONSORING / MONITORING AGENCY NAME(S) AND ADDRESS(ES)

Air Force Research Laboratory
Attn: Larry Zawada
2230 10th Street
Wright-Patterson AFB, OH 45433

10. SPONSOR/MONITOR'S ACRONYM(S)

AFRL/RXCC

11. SPONSOR/MONITOR'S REPORT NUMBER(S)

12. DISTRIBUTION / AVAILABILITY STATEMENT

DISTRIBUTION STATEMENT A:
APPROVED FOR PUBLIC RELEASE; DISTRIBUTION UNLIMITED

13. SUPPLEMENTARY NOTES

This work is declared a work of the U.S. Government and is not subject to copyright protection in the United States.

14. ABSTRACT

High temperatures and structural loads in advanced aerospace structures often result in complex loading conditions. This study is focused on biaxial (tension-torsion) testing of an oxide-oxide porous matrix ceramic matrix composite (CMC) (Nextel[TM] 720/AS) thin wall tube with a novel involute layup. Tests included pure torsion and biaxial (tension- torsion) loading. Strain gages were used in addition to digital image correlation (DIC) to measure strains and to detect crack initiation and propagation. Room temperature and $1100°C$ uniaxial tests were performed in a build up approach prior to biaxial (tension-torsion) testing. Double-notch shear (DNS) specimens were tested at $1100°C$ in air to obtain interlaminar shear strength (ILSS).

15. SUBJECT TERMS

Ceramic Matrix Composites, Composite Materials, Ceramic Fibers, Ceramic Materials, Fiber Reinforced Composites, Alumina, Aluminosilicate, Mullite, Creep, Oxides, Nextel[TM] 720 Fiber, Tube, Biaxial, Involute, Tension-Torsion

16. SECURITY CLASSIFICATION OF:			17. LIMITATION OF ABSTRACT	18. NUMBER OF PAGES	19a. NAME OF RESPONSIBLE PERSON
a. REPORT	b. ABSTRACT	c. THIS PAGE			Dr. Marina B. Ruggles-Wrenn (ENY)
U	U	U	UU	153	19b. TELEPHONE NUMBER *(include area code)* (937)-255-3069 x 4641 marina.ruggles-wrenn@afit.edu

Standard Form 298 (Rev. 8–98)
Prescribed by ANSI Std. Z39.18